Universitat Politècnica de València
I.U.I. CMT - Clean Mobility & Thermofluids

Doctoral Thesis

Computational modelling of the primary atomization in aero engine airblast atomizers through a DNS approach

Presented by:
Mr. Carlos Moreno Montagud

Supervised by:
Dr. Marcos Carreres Talens

in fulfillment of the requirements for the degree of
Doctor of Philosofy

Valencia, July 2024

Ph.D. Thesis

Computational modelling of the primary atomization in aero engine airblast atomizers through a DNS approach

Written by: Mr. Carlos Moreno Montagud
Supervised by: Dr. Marcos Carreres Talens

Thesis committee:

Chairman: Dr. José María Desantes Fernández
Secretary: Dr. Jorge Martínez López
Member: Dr. Clara García Sánchez

Valencia, July 2024

Abstract

The aviation industry's expansion in recent decades has led to increased pollutant emissions, impacting global climate and air quality. Environmental regulations try to address these issues, encouraging innovation in combustion technologies for aero-engine designs. Lean combustion has emerged as a potential solution to reduce NOx and particulate matter emissions, but it requires precise control to avoid flame instability.

In this context, the project ESTiMatE (`https://estimate-project.eu/`) emerges aiming to enhance the reliability and precision of soot predictions specifically tailored to the aeronautical sector. The research carried out within this project holds significant promise for advancing our knowledge of soot formation mechanisms and improving combustion efficiency, ultimately leading to reduced emissions and improved environmental sustainability in aviation. To achieve this, it is crucial to thoroughly understand and characterize various phenomena that influence soot formation, including fuel atomization, mixing, combustion, and subsequent emissions formation. The present thesis, as part of the ESTiMatE project, focuses in the first step to characterize spray flames, i.e. the liquid atomization process.

There exist some empirical models to characterize atomization. Rosin-Rammler model assumes an exponential size distribution of droplets, while PAMELA model combines a Lagrangian representation of individual droplets with a Eulerian description of the continuous liquid phase, capturing the spatial distribution of droplets within the spray and providing detailed information on droplet size and position. The objective of this specific work package of the ESTiMatE project is to develop a new phenomenological model through high-fidelity simulations instead of empirical results. This model is proposed to be coupled to the Integrated Technology Demonstrator (ITD) leader code PRECISE-UNS and the Barcelona Supercomputing Center (BSC) code Alya to inject droplets in Lagrangian simulations, effectively reproducing the key features of the primary atomization process on the spray formation.

Prefilming airblast atomizers are particularly chosen as they gained significant popularity in modern aero engines. Conducting fundamental studies on the actual annular configuration of airblast atomizers is challenging, so researchers have directed their attention towards planar configurations as an alternative that can provide valuable insights. The Karlsruhe Institute of Technology (KIT) has made notable contributions in this regard by developing a dedicated planar test rig, enabling researchers to conduct comprehensive experiments and generating a substantial database of results encompass-

ing various working fluids and operating conditions, allowing two-phase flow modellers to validate their calculations concerning primary atomization.

This thesis presents a comprehensive investigation of primary atomization in these devices with a computational approach using embedded Direct Numerical Simulations (eDNS) within the PARIS Simulator code. This methodology makes use of the Volume of Fluid (VOF) method in VOF-DNS simulations of the atomizing edge to obtain useful data, and precursor one-phase Large-Eddy Simulations (LES) simulations in order to account for gas inflow turbulence at the DNS inlet. Nevertheless, two slightly different methodologies have been derived from eDNS, extending it with additional precursor two-phase LES simulations. The first one, imposes constant liquid film thickness and velocity at the DNS inlet, but unlike the usual eDNS, their mean values are obtained processing the new two-phase LES simulations. It has been validated for a reference operating condition, representative of altitude relight, as there is many experimental and computational data available in the literature. The second one, introduces variable liquid film thickness and velocity instead, constituting a more realistic boundary condition for the DNS.

Two different studies have been conducted in this regard. On the one hand, using the former methodology, a parametric study was performed to investigate the impact of mean gas velocity and fluid properties on the formation of liquid structures. By varying these parameters (therefore Reynolds, Weber and Ohnesorge dimensionless numbers), differences on the breakup mechanisms are observed based on the momentum flux ratio, as found in the literature. The results provide insights into the complex dynamics of primary atomization and the role of those different operational parameters. The basis for a phenomenological model has been established using these results, and it can be extended with more operating conditions following the described methodology. On the other hand, a comparison between both methodologies has been carried out in parallel, in order to account for the influence of film history on the primary atomization process. In this study, by improving the inlet boundary conditions, the phenomenology observed in the experimental results from the literature has been succesfully reproduced, unlike with the standard eDNS.

A novel post-processing technique for characterizing liquid structures has been proposed and used. Usual post-processing methods in two-phase flows detect droplets in a 3D domain but only detect ligaments in a top view 2D projection of it using algebraic functions optimization. However, this new method is able to find both droplets and ligaments as well as its 3D properties within the atomizer, using the Open Computer Vision Library (OpenCV)

instead. It has been also validated with the experimental and computational results in the literature.

Overall, the thesis has laid the foundations for the development of specific airblast atomization models through the use of high-fidelity simulations. Therefore, it contributes to a better prediction of the injection, atomization, evaporation, mixing and combustion phenomena in aero engines, enabling a more efficient design towards sustainable air mobility.

Resumen

La expansión de la industria aeronáutica en las últimas décadas ha llevado a un aumento de las emisiones contaminantes, repercutiendo en el clima global y la calidad del aire. Las regulaciones ambientales intentan abordar estos problemas, fomentando la innovación en tecnologías de combustión para los diseños de motores aeronáuticos. La combustión de mezclas pobres ha surgido como posible solución para reducir las emisiones de NO_x y partículas, pero requiere un control preciso para evitar la inestabilidad de la llama.

En este contexto, el proyecto ESTiMatE (`https://estimate-project.eu/`) nace con el objetivo de mejorar la fiabilidad y precisión de las predicciones de hollín enfocándose específicamente en el sector aeronáutico. La investigación llevada a cabo dentro de este proyecto tiene un gran potencial para avanzar en el conocimiento sobre los mecanismos de formación de hollín y mejorar la eficiencia de la combustión, lo que en última instancia conduce a la reducción de emisiones y una mayor sostenibilidad ambiental en la aviación. Para lograr esto, es crucial comprender a fondo y caracterizar varios fenómenos que influyen en la formación de hollín, incluyendo la atomización del combustible, la mezcla, la combustión y la consecuente formación de emisiones. La presente tesis, como parte del proyecto ESTiMatE, se centra en el primer paso para caracterizar las *spray flames* (llamas obtenidas al quemar un chorro líquido), es decir, el proceso de atomización del líquido.

Existen algunos modelos empíricos para caracterizar la atomización. El modelo de Rosin-Rammler asume una distribución exponencial del tamaño de gotas, mientras que el modelo PAMELA combina una representación Lagrangiana de las gotas individuales con una descripción Euleriana de la fase líquida contínua, capturando la distribución espacial de las gotas dentro del spray y proporcionando información detallada sobre el tamaño y la posición de las mismas. El objetivo de este paquete de trabajo específico del proyecto ESTiMatE es desarrollar un nuevo modelo fenomenológico a través de simulaciones de alta fidelidad en lugar de resultados empíricos. Se propone acoplar este modelo al código PRECISE-UNS del líder Integrated Technology Demonstrator (ITD) y al código Alya del Barcelona Supercomputing Center (BSC) para inyectar gotas en simulaciones Lagrangianas, reproduciendo de forma efectiva las características clave del proceso de atomización primaria en la formación del spray.

Los atomizadores de tipo *prefilming airblast* han sido elegidos particularmente ya que han ganado una popularidad significativa entre los aeromotores modernos. Realizar estudios fundamentales sobre la configuración anular de estos atomizadores es un gran desafío, por lo que los investigadores han enfo-

cado sus esfuerzos en la configuración plana como una alternativa que puede proporcionar información valiosa. El *Karlsruhe Institute of Technology* (KIT) ha hecho contribuciones notables en este sentido al desarrollar un banco de pruebas de configuración plana, proporcionando a los investigadores la posibilidad de llevar a cabo experimentos exhaustivos y generar una base de datos extensa con resultados que abarcan diversos fluidos de trabajo y condiciones de operación, y permitiendo además a los modeladores de flujo bifásico validar sus cálculos en relación con la atomización primaria.

Esta tesis presenta una investigación exhaustiva de la atomización primaria en estos dispositivos con un enfoque computacional a través de simulaciones *Direct Numerical Simulation* (DNS) de tipo embebido (eDNS) empleando el código PARIS Simulator. Esta metodología utiliza el método *Volume of Fluid* (VOF) en simulaciones VOF-DNS del borde del atomizador para obtener información útil, y simulaciones *Large-Eddy Simulations* (LES) monofásicas precursoras que permiten tener en cuenta la turbulencia del gas en la entrada de dichas simulaciones VOF-DNS. No obstante, se han propuesto dos nuevas metodologías ligeramente diferentes derivadas a partir de eDNS, extendiéndola con simulaciones LES bifásicas adicionales. La primera de ellas impone un espesor y velocidad constantes para la película líquida en la entrada de la DNS, pero a diferencia de la eDNS habitual, sus valores medios se obtienen procesando las nuevas simulaciones LES bifásicas. Esta metodología ha sido validada para una condición de operación de referencia, representativa del reencendido en altitud, ya que hay muchos datos experimentales y computacionales disponibles en la literatura. La segunda, introduce un espesor y velocidad variables de la película líquida, constituyendo una condición de contorno más realista para la DNS.

Se han realizado dos estudios diferentes al respecto. Por un lado, utilizando la primera metodología, se realizó un estudio paramétrico para investigar el impacto de la velocidad media del gas y las propiedades del fluido en la formación de estructuras líquidas. Al variar estos parámetros (por tanto, los números adimensionales de Reynolds, Weber y Ohnesorge), se observan diferencias en los mecanismos de ruptura basadas en el ratio de flujo de momento entre líquido y gas, como se afirma en la literatura. Los resultados proporcionan mayor perspectiva sobre la compleja dinámica de la atomización primaria y el papel que desempeñan esos parámetros operacionales. La base para un modelo fenomenológico se ha establecido utilizando estos resultados y puede extenderse con más condiciones de operación siguiendo la metodología descrita. Por otra parte, se ha realizado en paralelo una comparación entre ambas metodologías, para considerar la influencia de la historia de la película de combustible en el proceso de atomización primaria. En este estudio, al

mejorar las condiciones de contorno a la entrada, se ha logrado reproducir con éxito la fenomenología presente en los resultados experimentales de la literatura, al contrario que con la eDNS estándar.

Se ha propuesto y utilizado una novedosa técnica de postprocesado para caracterizar las estructuras líquidas. Los métodos de postprocesado habituales en flujos bifásicos detectan gotas en un dominio 3D, pero solamente detectan ligamentos en una proyección 2D del mismo desde una vista superior, utilizando optimización de funciones algebraicas. Sin embargo, este nuevo método es capaz de encontrar gotas y ligamentos, así como sus propiedades, totalmente en 3D utilizando la librería de visión por computador OpenCV. También ha sido validado con los resultados experimentales y computacionales disponibles en la literatura.

Con todo, la tesis ha sentado las bases para el desarrollo de modelos específicos de atomización *airblast* mediante el uso de simulaciones de alta fidelidad, siendo por tanto una contribución hacia una mejor predicción de los fenómenos de inyección, atomización, evaporación, mezcla y combustión de los aeromotores que permita realizar un diseño más eficiente de los mismos hacia una movilidad aérea sostenible.

Resum

L'expansió de la indústria aeronàutica en les últimes dècades ha portat a un augment de les emissions contaminants, repercutint en el clima global i la qualitat de l'aire. Les regulacions ambientals intenten abordar aquests problemes, fomentant la innovació en tecnologies de combustió per als dissenys de motors aeronàutics. La combustió de mescles pobres ha sorgit com a possible solució per reduir les emissions de NO_x i partícules, però requereix un control precís per evitar la inestabilitat de la flama.

En aquest context, el projecte ESTiMatE (`https://estimate-project.eu/`) naix amb l'objectiu de millorar la fiabilitat i precisió de les prediccions de sutge enfocant-se específicament en el sector aeronàutic. La investigació realitzada dins d'aquest projecte té un gran potencial per avançar en el coneixement sobre els mecanismes de formació de sutge i millorar l'eficiència de la combustió, cosa que en última instància condueix a la reducció d'emissions i a una major sostenibilitat ambiental en l'aviació. Per aconseguir això, és crucial comprendre a fons i caracteritzar diversos fenòmens que influeixen en la formació de sutge, incloent l'atomització del combustible, la mescla, la combustió i la consegüent formació d'emissions. La present tesi, com a part del projecte ESTiMatE, se centra en el primer pas per caracteritzar les *spray flames* (flames obtingudes en cremar un doll líquid), és a dir, el procés d'atomització del líquid.

Existeixen alguns models empírics per caracteritzar l'atomització. El model de Rosin-Rammler assumeix una distribució exponencial de la grandària de les gotes, mentre que el model PAMELA combina una representació Lagrangiana de les gotes individuals amb una descripció Euleriana de la fase líquida contínua, capturant la distribució espacial de les gotes dins de l'spray i proporcionant informació detallada sobre la grandària i la posició de les mateixes. L'objectiu d'aquest paquet de treball específic del projecte ESTiMatE és desenvolupar un nou model fenomenològic a través de simulacions d'alta fildelitat en lloc de resultats empírics. Es proposa acoblar aquest model al codi PRECISE-UNS del líder Integrated Technology Demonstrator (ITD) i al codi Alya del Barcelona Supercomputing Center (BSC) per injectar gotes en simulacions Lagrangianes, reproduint de manera efectiva les característiques clau del procés d'atomització primària en la formació de l'spray.

Els atomitzadors de tipus *prefilming airblast* han sigut triats particularment ja que han guanyat una popularitat significativa entre els aeromotors moderns. Realitzar estudis fonamentals sobre la configuració anul · lar d'estos atomitzadors és un gran desafiament, per la qual cosa els investigadors han enfocat els seus esforços en la configuració plana com una alternativa que pot

proporcionar informació valuosa. El *Karlsruhe Institute of Technology* (KIT) ha fet contribucions notables en aquest sentit en desenvolupar un banc de proves de configuració plana, proporcionant als investigadors la possibilitat de dur a terme experiments exhaustius i generar una base de dades extensa amb resultats que abasten diversos fluids de treball i condicions d'operació, i permetent a més als modeladors de flux bifàsic validar els seus càlculs en relació amb l'atomització primària.

Esta tesi presenta una investigació exhaustiva de l'atomització primària en aquests dispositius amb un enfocament computacional a través de simulacions *Direct Numerical Simulation* (DNS) de tipus embegut (eDNS) emprant el codi PARIS Simulator. Aquesta metodologia utilitza el métode *Volume of Fluid* (VOF) en simulacions VOF-DNS de la vora de l'atomitzador per a obtindre informació útil, i simulacions *Large-Eddy Simulations* (LES) monofàsiques precursores que permeten tindre en compte la turbulència del gas a l'entrada d'aquestes simulacions VOF-DNS. No obstant això, s'han proposat dos noves metodologies lleugerament diferents derivades a partir de eDNS, estenent-la amb simulacions LES bifàsiques addicionals. La primera d'elles imposa una grossària i velocitat constants per a la pel · lícula líquida en l'entrada de la DNS, però a diferència de la eDNS habitual, els seus valors mitjans s'obtenen processant les noves simulacions LES bifàsiques. Aquesta metodologia ha sigut validada per a una condició d'operació de referència, representativa de la reencesa en altitud, ja que hi ha moltes dades experimentals i computacionals disponibles en la literatura. La segona, introduïx una grossària i velocitat variables de la pel · lícula líquida, constituint una condició de contorn més realista per a la DNS.

S'han realitzat dos estudis diferents sobre aquest tema. D'una banda, utilitzant la primera metodologia, es va realitzar un estudi paramètric per a investigar l'impacte de la velocitat mitjana del gas i les propietats del fluid en la formació d'estructures líquides. En variar estos paràmetres (per tant, els números adimensionals de Reynolds, Weber i Ohnesorge), s'observen diferències en els mecanismes de ruptura basades en el ràtio de flux de moment entre líquid i gas, com s'afirma en la literatura. Els resultats proporcionen major perspectiva sobre la complexa dinàmica de l'atomització primària i el paper que exercixen eixos paràmetres operacionals. La base per a un model fenomenològic s'ha establit utilitzant aquests resultats i pot estendre's amb més condicions d'operació seguint la metodologia descrita. D'altra banda, s'ha realitzat en paral · lel una comparació entre totes dues metodologies, per a considerar la influència de la història de la pel · lícula de combustible en el procés d'atomització primària. En aquest estudi, en millorar les condicions de contorn a l'entrada, s'ha aconseguit reproduir amb èxit la fenomenologia

present en els resultats experimentals de la literatura, al contrari que amb la eDNS estàndard.

S'ha proposat i utilitzat una nova tècnica de postprocessament per a caracteritzar les estructures líquides. Els mètodes de postprocessament habituals en fluxos bifàsics detecten gotes en un domini 3D, però solament detecten lligaments en una projecció 2D del mateix des d'una vista superior, utilitzant optimització de funcions algebraiques. No obstant això, aquest nou mètode és capaç de trobar gotes i lligaments, així com les seues propietats, totalment en 3D utilitzant la llibrería de visió per computador OpenCV. També ha sigut validat amb els resultats experimentals i computacionals disponibles en la literatura.

Amb tot, la tesi ha establit les bases per al desenvolupament de models específics d'atomització *airblast* mitjançant l'ús de simulacions d'alta fidelitat, sent per tant una contribució cap a una millor predicció dels fenòmens d'injecció, atomització, evaporació, mescla i combustió dels aeromotors que permeta realitzar un disseny més eficient dels mateixos cap a una mobilitat aèria sostenible.

"Los hombres geniales empiezan grandes obras, los hombres trabajadores las terminan".
Leonardo da Vinci

A mi iaia

Hace más de una década que comenzó mi etapa universitaria aquí, en la Universitat Politècnica de València. En todo este tiempo he tenido el placer y la suerte de coincidir con muchas personas extraordinarias que, de un modo u otro, han dejado una huella imborrable en mí. De todos ellos he aprendido grandes lecciones, no solamente en el ámbito académico sino también en el personal, así que quiero aprovechar esta oportunidad para agradecérselo.

No puedo empezar de otra manera que no sea agradeciendo infinitamente a mi tutor y director de tesis, Marcos Carreres. Él es el principal culpable de que floreciera en mí la idea de realizar un doctorado, y me ha brindado su apoyo en todo momento para conseguir sacar adelante este ambicioso proyecto. Durante estos más de 5 años he sido testigo de su gran implicación, revisando minuciosamente documentos y presentaciones, organizando incontables reuniones en las que replantear nuevos caminos a explorar cuando todo fallaba, tratando de recuperar la motivación si no éramos capaces de ver esa luz al final del túnel, estando disponible incluso fuera del horario laboral para incluir resultados de última hora... y un sinfín de situaciones más. Se ha ganado mi profundo respeto y admiración, y siento que no podría haber encontrado un mejor acompañante en esta aventura.

De igual modo, debo agradecer a la universidad los recursos recibidos a través del Contrato Predoctoral para la Formación de Doctores (UPV - SUBP2) dentro del Programa de Apoyo para la Investigación y Desarrollo (PAID-01-19) de la Universitat Politècnica de València; y al I.U.I. CMT - Clean Mobility & Thermofluids por brindarme la oportunidad de realizar la tesis en un centro de investigación de prestigio mientras participaba en un Proyecto Europeo de gran calibre. Desde la directiva, que mantiene los engranajes en marcha para que todo el departamento siga funcionando tras tantos años; pasando por la secretaría, cuyo personal (en especial Amparo) ha sido capaz de convertir el infierno burocrático en un camino de rosas; hasta el personal de limpieza, iluminando con una amable sonrisa las tardes en las que era un estorbo por ser el último en marcharme del despacho.

Me siento enormemente agradecido además con los integrantes del departamento de inyección, que me han ofrecido un inmejorable ambiente de trabajo. A Raúl Payri liderando al equipo en las reuniones de los miércoles, pero también en los almuerzos de La Pascuala o las tardes de karting. A los profesores Javi, Jaime, Pedro, Joaquín y Gabriela siempre dispuestos a echar una mano al recurrir a ellos ante cualquier duda. A los técnicos José Enrique y Omar, llevando el peso de los ensayos en instalaciones experimentales con un humor y buen rollo perpetuos. A los doctorandos, con quienes me he sentido identificado tarde o temprano durante todo este proceso: Alberto, Armando,

Vincenzo, Santiago, María, Kike, Javi, Tomás, César, Borja... (lo siento si me dejo a alguno).

Y cómo no, a mis compañeros de despacho. Marco, para mí un ejemplo a seguir, trabajador incansable y con una capacidad de análisis y aprendizaje admirables. Mario, que me ha estado guiando incluso antes de empezar en esta locura (cuando todavía estaba realizando el TFM) y que con su facilidad para sacar conversación hasta de las piedras me hizo mucho más amenas las interminables tardes de trabajo. Lucas, con quien he aprendido a utilizar la mayoría de herramientas que he necesitado, que siempre ha estado dispuesto a ayudar con bugs repentinos e inexplicables, y con quien he compartido scripts, comandos, conversaciones frikis, memes y chistes malos. Y finalmente Alejandro y Alicia, a quienes mando mucho ánimo con sus respectivos proyectos, que han llegado aquí con la ilusión del principiante desoyendo todas nuestras advertencias (corred, insensatos).

Me gustaría mencionar también a algunas personas de otros departamentos que han contribuido enormemente al desarrollo de este trabajo. Desde el departamento informático está Figo, a quien he recurrido innumerables veces para pedir ayuda con conexiones, dominios, cableado, cambios de contraseña y especialmente almacenamiento en los NAS, aumentando mi cuota en decenas de terabytes (para que luego digan que el saber no ocupa lugar). En el departamento de combustión a Chemari y a José Manuel, implicados en otras partes del proyecto ESTiMatE pero igualmente reuniéndose con nosotros y aportando todo tipo de sugerencias para seguir avanzando.

Y por último en cuanto a personal del CMT, pero no menos importante, mi compañero y amigo Iván. Prácticamente me ha acompañado en todo mi recorrido universitario, desde el primer curso de la carrera hasta el final del doctorado, formando incluso parte del mismo proyecto en otro de los paquetes de trabajo. Guardaré para siempre en mi memoria los trayectos en tranvía (o si había suerte en coche), los interminables trabajos en equipo y memorias de prácticas, las tardes de estudio para los éxamenes y sus audios de 10 minutos resolviéndome dudas de manera impecable, los almuerzos a las 11h o los viernes de sushi (siempre con su correspondiente paseo para estirar las piernas), las conversaciones sobre videojuegos o literatura fantástica para desconectar, los inicios en el gimnasio que sirvieron para motivarnos mutuamente en eso de la vida sana, los intercambios de ideas cuando nos hemos ido atascando en nuestros respectivos proyectos... Ha sido un verdadero placer recorrer este camino a tu lado y no me cabe duda de que vas a conseguir grandes cosas, como ya has hecho al adelantarme por el interior y defender tu tesis de manera impecable.

Por otra parte, quiero agradecer del BSC a Dani, supervisando el proyecto ESTiMatE, programando reuniones extra para atajar y resolver los contratiempos de manera muy profesional; y Carlos, que ha cogido el relevo de cierta manera aportando ideas para el modelo fenomenológico, realizando las primeras implementaciones para probarlo y darnos feedback, y ayudando a redactar los últimos entregables del proyecto. También a Esther Pla, que desde la Escuela de Doctorado en la propia universidad me ayudó enormemente en la gestión de la Beca de Movilidad y el papeleo correspondiente para poder disfrutar de una estancia en un centro de investigación extranjero: el Institut d'Alembert de la Sorbonne Université. De allí, agradecer al Profesor Stéphane Zaleski por tutorizarme, a mis compañeros por su aportación en los "pulse meetings" semanales y al personal administrativo por la gestión de la exasperante burocracia francesa, identificaciones, llaves de acceso, etc. Y precisamente hablando de mi estancia en París, no puedo olvidarme de la gente maravillosa que conocí en la Cité y especialmente en la Fondation de Monaco donde me hospedé: Laura, Lacmé, César, Emma, Morgan, Diane, Andrés, Simón, Isaías, Johann, Tomás, Raquel, José, Diana... (de nuevo perdón si me dejo a alguien). Sois geniales, me lo pasé increíble junto a vosotros y espero que nuestros caminos se vuelvan a cruzar en el futuro.

Finalmente, fuera del entorno académico y de la investigación he recibido el apoyo de muchas personas que, incluso sin entender lo que me llevaba entre manos, me han ofrecido un consuelo constante, su compañía para desconectar y sus ánimos para seguir avanzando. A ellos también va dedicado este texto.

A mi familia, y en particular a mis padres y mi hermano, que han estado en el día a día achuchando para que pise el acelerador a fondo. A mis queridísimos Ajuaseite: Adri, Barri, Clau, Esther, Gabi, Javi C, Javi S, Juan, Nacho, Paloma, Paz, Tono y Xavi. Me siento muy privilegiado de formar parte de este grupo en el que compartimos cada triunfo (que no son pocos), y este es uno más. A mis Castores: Mir, Ana, José, Adolfo, Javi, Toni, Marta y Guille. Un grupo muy variopinto, pero que sabe mejor que nadie cómo desconectar organizando una buena escapada por la naturaleza o una fiesta en condiciones. Ya sabéis cuánto os aprecio y también que "yo nunca he conducido en Carpesa". A mi estimada orquesta, la JOSC, que me ha permitido desde hace más de 10 años conocer a gente maravillosa a través de la música, como a su apasionado director Javi Olmos o mi gran mejor amiga incondicional Lidia. A mis amados Otomanos: Aarón, Adrián, Alberto, Ana, José, Juanjo, Lucía, María, Migue, Paula M, Paula S, Pedro, Rafael, Nuria y Xavi. Me habéis hecho disfrutar de muchos pequeños momentos de la vida (esmorçarets, previas, comidas, fiestas, Santa Cecilias, actos de banda y de xaranga Quatre Gats...) que, sumados en conjunto, forman un gran pilar

de felicidad y dan sentido a mi vida. Y por último también a mis adorados gamers: Tami con su entusiasmo y su don para los motes, Rafa con su humor especial y su carisma en los vídeos y streamings, Alba con una inteligencia y una capacidad de análisis envidiables (dentro y fuera de los videojuegos) que además es mi "dúo bot favorita ever", Chema con su pensamiento lateral e inusitada forma de tomar decisiones que pueden resultar geniales o fatídicas, y Raúl (Detad), al que espero tener la oportunidad de ver en persona cuando me vuelva a dejar caer por Madrid.

A todos y cada uno de vosotros, mil gracias.

Contents

List of Figures

List of Tables

Nomenclature

Acronyms

ACARE	Advisory Council for Aeronautics Research in Europe.
AMR	Adaptive Mesh Refinement.
BSC	Barcelona Supercomputing Center.
CAEP	Committee on Aviation Environmental Protection.
CDF	Cumulative Distribution Function.
CFD	Computational Fluid Dynamics.
CFL	Courant-Friedrichs-Lewy number.
CIAM	Calcul d'Interface Affine par Morceaux.
CLSMOF	Coupled Level-Set Moment Of Fluid
CLSVOF	Coupled Level-Set Volume Of Fluid
CPU	Central Processing Unit.
CSF	Continuous Surface Force.
DMD	Dynamic Mode Decomposition.
DNS	Direct Numerical Simulation.
eDNS	embedded DNS.
ELSA	Eulerian-Lagrangian Spray Atomization.
ELVIRA	Efficient Least-squares Vof Interface Reconstruction Algorithm.
ENO	Essentially Non-Oscillatory.
ESTiMatE	Emissions SooT ModEl.
FCT	Flux-Corrected Transport.
FFT	Fast Fourier Transform.

FT	Front-Tracking.
FVM	Finite Volume Method.
GAMG	Geometric-Algebraic MultiGrid.
HF	Height Function.
ICAO	International Civil Aviation Organisation.
ICM	Interface Capturing Methods.
ITD	I T D.
KH	Kelvin-Helmholtz.
KIT-ITS	Karlsruhe Institute of Technology - Institute of Thermal Turbomachinery.
LDA	Laser Doppler Anemometry.
LDT	Light Diffraction Technique.
LES	Large-Eddy Simulation.
LS	Level-Set.
MULES	Multidimensional Universal Limiter for Explicit Solution.
MYC	Mixed Youngs Centered.
NGA	N G A.
OpenCV	Open Computer Vision.
OpenFOAM	Open Field Operation And Manipulation.
PAMELA	Primary Atomization Model por prEfilming airbLAst injectors.
PARIS	PArallel Robust Interface Simulator.
PDA	Phase-Doppler Anemometry.
PDF	Probability Density Function.
PISO	Pressure Implicit with Splitting of Operators.
PIV	Particle Image Velocimetry.
PLIC	Piecewise Linear Interface Calculation.
POD	Proper Orthogonal Decomposition.
PRECISE-UNS	Predictive-System for Real Engine Combustors - Unstructured.
PROST	Proper Representation Of Surface Tension.
QUICK	Quadratic Upstream Interpolation for Convective Kinematics.
RANS	Reynolds-Averaged Navier-Stokes.
RMS	Root Mean Square.
SGS	Sub-Grid Scale.

SLIC	Simple Line Interface Calculation.
SMD	Sauter Mean Diameter.
SPH	Smoothed Particle Hydrodynamics.
UHC	Unburned hydrocarbons.
VOF	Volume of Fluid.
VTK	Visualization ToolKit.
WALE	Wall Adapting Local Eddy-viscosity.
WY	Weymouth and Yue.

Greek symbols

α	Liquid volume fraction.
α_u	Shape parameter of the Weibull distribution for streamwise velocity.
α_y	Shape parameter of the Weibull distribution for wall-normal location.
β_u	Scale parameter of the Weibull distribution for streamwise velocity.
β_y	Scale parameter of the Weibull distributionfor wall-normal location.
δ_g	Gaseous vorticity thickness.
δ_S	Dirac delta function for the liquid interface.
δ_{TE}	Trailing edge boundary layer thickness.
γ_u	Threshold parameter of the Weibull distribution for streamwise velocity.
γ_y	Threshold parameter of the Weibull distribution for wall-normal location.
κ	Curvature.
λ_L	Kelvin-Helmholtz instability wavelength.
λ_T	Rayleigh-Taylor instability wavelength.
λ_w	Parameter of the Laplace distribution for spanwise velocity.
μ	Dynamic Viscosity.
μ_d	Parameter of the lognormal distribution for the droplet size.
μ_v	Parameter of the logistic distribution for wall-normal velocity.
∇	Gradient.
ν_l	Liquid kinematic viscosity.

ν_{SGS}	Subgrid scale viscosity.
$\overline{\lambda_{film}}$	Mean film wavelength.
ϕ	Flow property.
ρ	Density.
σ	Surface tension between the liquid and the gas.
σ_d	Parameter of the lognormal distribution for the droplet size.
σ_v	Parameter of the logistic distribution for wall-normal velocity.
σ_{hl}	Standard deviation from the mean film height.
θ	Contact angle.
θ_i	Phase of the signal.

Latin symbols

$\bar{u}$	Characteristic velocity.
$\dot{m}$	Mass flow rate.
$\dot{m}_{fuel}$	Fuel mass flow rate.
$\dot{m}_{norm}$	Normalized liquid mass flow rate.
$\dot{V}$	Volumetric flow rate.
$\overline{f_{film}}$	Mean film wave frequency.
$\mathbf{n_{wall}}$	Wall-normal unit vector.
$\mathbf{n}$	Normal vector.
$\mathbf{u}^*$	Auxiliary velocity field.
$\mathbf{u_{drop}}$	Droplet velocity.
$\mathbf{u_{str2D}}$	String velocity with 2D method (at the tip).
$\mathbf{u_{str3D}}$	String velocity with 3D method (at the tip).
$\mathbf{u_{str}}$	String velocity (at the tip).
$\mathbf{u}$	Velocity field.
A	Amplitude of the signal.
a	Acceleration.
A^n	Advection term.
b	Span.
C	Color function.
C_α	Interface sharpening binary coefficient.
d	Diameter.
D^n	Diffusion term.
d_V	Volumetric diameter.

d_{eq}	Equivalent diameter.
f	Frequency.
F^n	Forces term.
f_σ	Surface tension force term.
f_{bu}	Breakup frequency.
f_{main}	Main frequency among breakup events.
g_c	Cell grading coefficient.
H	Heavyside function.
h	Height function.
h_c	Channel height.
h_l	Liquid film thickness.
h_p	Atomizing edge thickness.
k	Turbulent kinetic energy.
k_A	Standard deviation constant for the signal amplitude.
k_f	Standard deviation constant for the signal frequency.
L	Length scale.
l_0	Integral length scale.
l_η	Kolmogorov length scale.
L_f	Effective film length.
L_p	Prefilming length.
L_x	Domain length.
L_y	Domain height.
L_z	Domain span.
L_{90}	Length where 90% of the ligaments broke up.
L_{bu}	Breakup length.
L_{str2D}	String length with 2D method.
L_{str3D}	String length with 3D method.
L_{str}	String length.
M	Momentum flux ratio.
N_{cells}	Number of cells.
Oh	Ohnesorge number.
P	Pressure.
P_a	Ambient pressure.
q	Parameter of the logistic distribution.

r	Density ratio.
R^2	Correlation coefficient.
Re	Reynolds number.
Re_τ	Friction Reynolds number.
S	Mass transfer source term.
T	Temperature.
t	Time.
T_i	FFT Period.
u	Streamwise velocity.
u^+	Non-dimensional streamwise velocity.
u_{def}	Film deformation velocity.
u_{lig}	Ligament velocity (at the tip).
u_{norm}	Normalized streamwise velocity.
V	Volume.
v	Wall-normal velocity.
v^+	Non-dimensional wall-normal velocity.
V_{cell}	Cell volume.
V_{drop}	Droplet liquid volume.
V_{lig}	Ligament volume.
v_{norm}	Normalized wall-normal velocity.
w	Spanwise velocity.
w^+	Non-dimensional spanwise velocity.
w_{norm}	Normalized spanwise velocity.
We	Weber number.
We_δ	Weber number based on boundary layer thickness at the pre-filmer trailing edge.
We_h	Weber number based on atomizing edge thickness and gas velocity.
We_l	Weber number based on liquid film thickness and relative velocity between gas and liquid.
x	Streamwise location.
x_{max}	Furthest location in streamwise direction.
y	Wall-normal location.
y^+	Non-dimensional boundary layer distance.
z	Spanwise location.

Subscripts

δ	Based on boundary layer.
g	Gas phase.
h	Based on atomizing edge.
l	Liquid phase.
S	Surface.

Chapter 1

Introduction

1.1 General context

The aviation industry, which is a key part in global development and economy, has continued its expansion in the last decades, producing a not negligible part of the pollutant emissions in the world. This contamination problem produced by aircraft has a strong impact in global climate and local air quality affecting human health, and it gets worse because combustion residues at high altitudes of the troposphere are more harmful to the environment than they are at sea level [1]. For this reason, the aviation industry must keep innovating and improving performance to ensure the sustainable growth of the sector and accomplish the increasingly stringent environmental regulations. Organizations like ICAO-CAEP and the Advisory Council for Aviation Research and Innovation in Europe (ACARE) established regulations since the 1990s to which aero-engine designes must adhere, encouraging companies to consistently innovate in combustion technologies and develop new engine concepts that decrease fuel consumption and minimize pollutant and noise emissions [2]. ACARE's objectives for year 2050 primarily aim to reduce CO_2 by 75% per passenger and km, NO_x by 90%, and noise by 65% relative to year 2000 levels [3], but there are other pollutants such as CO, unburned hydrocarbons (UHC) or soot that have negative effects on health and environment. Modern gas turbines have succesfully reduced most of them except for NO_x.

All in all, lean combustion has emerged as a good candidate to solve this problem. During lean combustion the amount of oxygen available is relatively high as the mixture contains less fuel than it is required for the stoichiometric

combustion, resulting in a reduced temperature and minimizing the formation of NO_x and particulate matter like soot. Nevertheless, it requires high control of the process to avoid combustion instability and flameout [4]. As controlling combustion in aero engines highly depends on the atomization, evaporation and mixing phenomena, the research community has increased their interest in those processes, specially the first one as it triggers the whole sequence.

In this context, the ESTiMatE project arises under the European Union's Horizon 2020 research and innovation programme [5]. Its main goal consists in modeling soot formation in aeronautical combustors at relevant conditions of engine operation. This involves many different phenomena to be characterized as fuel atomization, air and fuel mixing, combustion and subsequent emissions formation. As studies deepen our understanding of those processes, the reliability of soot predicitions increases in the aeronautical sector. This project has different work packages focusing on four areas: reference experiments, primary breakup, soot model development and turbulent combustion modelling.

There are different Work Packages (WPs) in this project, one of them focused in the atomization process taking place in airblast atomizers. The present thesis, as part of this specific WP, intends to gain insight into the liquid atomization process in prefilming airblast atomizers. This study is interesting for two reasons: near-field simulation can provide information that is difficult to obtain through experiments, and atomization is the first link in the chain for characterizing spray flames. It is in pursue of a phenomenological breakup model to be coupled with the Integrated Technology Demonstrator (ITD) leader code PRECISE-UNS [6] and the Barcelona Supercomputing Center (BSC) code Alya [7] to reproduce the main characteristics of the spray impacting the flame. To this end, high-fidelity simulations of primary breakup in airblast atomizers have been carried out following the methodology exposed in Chapter 2. The results obtained have been analyzed and post-processed, studying the influence of the key parameters in Chapters 3 and 4. Next, the model is proposed and developed in Chapter 5. In the frame of ESTiMatE, other project partners will implement this model into Alya and PRECISE-UNS solvers, examining its computational efficiency and usability in Large-Eddy Simulations of the reacting flow in aeronautical burners. Finally, the main findings of the document are described in Chapter 6.

1.2 Fundamentals of atomization

The atomization process is the transformation of a liquid into small droplets or particles in a gaseous atmosphere through mechanical devices called atomizers or nozzles. It is achieved by breaking up a liquid jet or sheet through various means, such as the kinetic energy of the liquid itself (e.g. pressure swirl atomizer), the exposure to high-velocity gas stream (e.g. airblast atomizer) or by mechanical energy applied externally through rotating or vibrating devices (e.g. rotatory or piezoelectric atomizers) [8].

Depending on the distance to the nozzle, atomization is cathegorized in two types:

- Primary atomization refers to the initial break-up in the near-field, as it exits the nozzle. This process is primarily governed by the internal flow dynamics of the nozzle, including size and shape of the orifice or the pressure and velocity of the liquid.
- Secondary atomization refers to the further break-up of the liquid structures formed during primary atomization. This process is typically governed by external factors such as airflow, turbulence and surface tension, resulting in a wide range of droplet sizes and shapes.

The ultimate droplet size distribution and spray pattern will depend on a combination of both processes, as well as the specific properties of the liquid being atomized and the conditions under which it occurs.

Atomization has a wide range of applications across various disciplines: agriculture (for pesticides and fertilizers), coating and spray painting, food industry (powders and emulsions), pharmaceutical and medicine industry (inhalable drug formulations, virus spreading studies and prevention) or automotive industry (fuel injection systems). This thesis explores the latter, focusing on fuel atomization in aircraft engines.

There are several dimensionless numbers used to characterize fluid flows and atomization. The density ratio r (Eq. 1.1) relates the ambient gas and injected liquid densities, where bigger values infer more liquid-gas interactions and favour mixture. The Reynolds number Re (Eq. 1.2) represents the ratio of inertial to viscous forces within a fluid, relating high values with turbulent flows and low values to laminar ones. The Weber number We (Eq. 1.3) relates the fluid's inertia to its surface tension, and the Ohnesorge number Oh (Eq. 1.4) compares both Reynolds and Weber numbers (viscous forces to surface tension forces). In these expressions, $\bar{u}$ is the characteristic velocity,

L is the length scale, ρ and μ represent the density and the dynamic viscosity respectively of the phase, and σ is the surface tension between both liquid and gas phases [8].

$$r = \frac{\rho_g}{\rho_l} \tag{1.1}$$

$$Re = \frac{\rho\,\bar{u}\,L}{\mu} \tag{1.2}$$

$$We = \frac{\rho\,\bar{u}^2\,L}{\sigma} \tag{1.3}$$

$$Oh = \frac{\mu}{\sqrt{\rho\,\sigma\,L}} = \frac{\sqrt{We}}{Re} \tag{1.4}$$

There are two main families of atomizers commonly used in aero-engines that contain no moving parts: pressure-swirl atomizers and prefilming airblast atomizers [8]. In the former, liquid fuel is brought into the environment and atomized by means of a pressure difference. This study focuses on the latter type of devices where, in turn, the fuel is first deposited onto a prefilmer and then driven by a surrounding high-velocity airstream towards an atomizing edge as shown in Figure 1.1. When the liquid reaches this edge, a shear instability appears on the film, it breaks up into ligaments and subsequently disintegrates into droplets. On the one hand, the film thickness parameter h_l is mainly used to characterise this kind of liquid structures, but as experimental works ([9–12]) cannot set a specific value, it has to be measured after determining a flow rate. On the other hand, the atomizing edge thickness h_p is another key parameter that influences the primary breakup as identified by Gepperth et al. [13, 14].

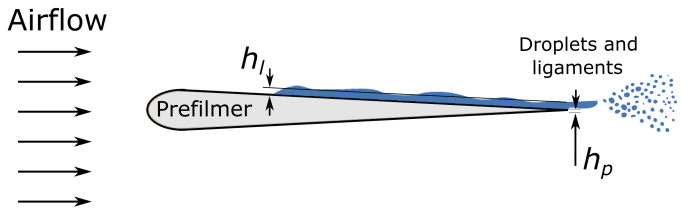

Figure 1.1: Prefilming airblast atomizer scheme.

There are two regimes the film can enter depending on its inertia and the thickness of the atomizing edge [15]. For high inertia films, the major driving mechanism on this devices is the interface shearing induced by the viscosities and relative velocity between both gas and liquid phases. This process induces sequential instabilities (with their corresponding wavelengths) that arise in form of waves at the film surface and end up in the primary atomization [16–19]:

1. The Kelvin-Helmholtz (KH) instability appears when there is a velocity difference in a flow. Figure 1.2 (left) shows a liquid film with two-dimensional waves in the surface of λ_L wavelength induced by this kind of instability. This wavelength is calculated in Equation 1.5, where C is a constant experimentally measured whose value is between 1 and 2, and δ_g is the gaseous vorticity thickness.

$$\lambda_L = C\sqrt{\frac{\rho_l}{\rho_g}\delta_g} \tag{1.5}$$

2. A secondary instability (Rayleigh-Taylor) is triggered by the acceleration of the wave crests due to aerodynamic drag [17, 20], inducing a three-dimensional pattern with wavelength λ_T as shown in Figure 1.2 (right). Afterwards, it is transformed into ligaments that are stretched and decomposed into droplets. This wavelength is calculated in Equation 1.6, where a is the acceleration of the fluid found in the crest of the waves.

$$\lambda_T = 2\pi\sqrt{\frac{3\sigma}{a\,\rho_l}} \tag{1.6}$$

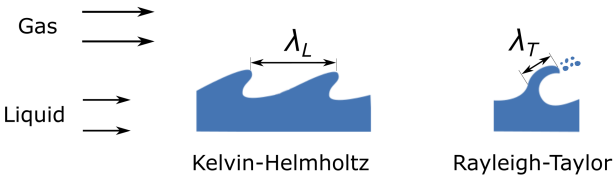

Figure 1.2: Sequential instabilities (left Kelvin-Helmholtz and right Rayleigh-Taylor) induced in the film surface according to Hong [17] and Varga's [20] approach.

On the contrary, lower inertia films accumulate in the wake region of the prefilmer. This liquid accumulation at the edge is then sheared by the air stream, producing a flapping movement that consequently forms bags and ligaments. Finally, those structures disintegrate into droplets [21].

However, in the flowing conditions for a prefilming airblast atomizer waves are not periodic and the predictions differ from linear stability theory [22]. As this is a complex problem, there is no established strategy for predicting the properties of those waves, but Mansour & Chigier [23] studied the liquid sheet as a damped spring and identified two types of oscillations or wave modes: sinusoidal (in-phase) and dilatational (out-of-phase). Experimental works by Stapper & Samuelsen [24], Lozano et al. [25] and Fernández et al. [26] also displayed macroscopic behaviours depending on the wave mode and the momentum flux ratio parameter (Eq. 1.7).

$$M = \frac{\rho_g \, \bar{u}_g^2}{\rho_l \, \bar{u}_l^2} \tag{1.7}$$

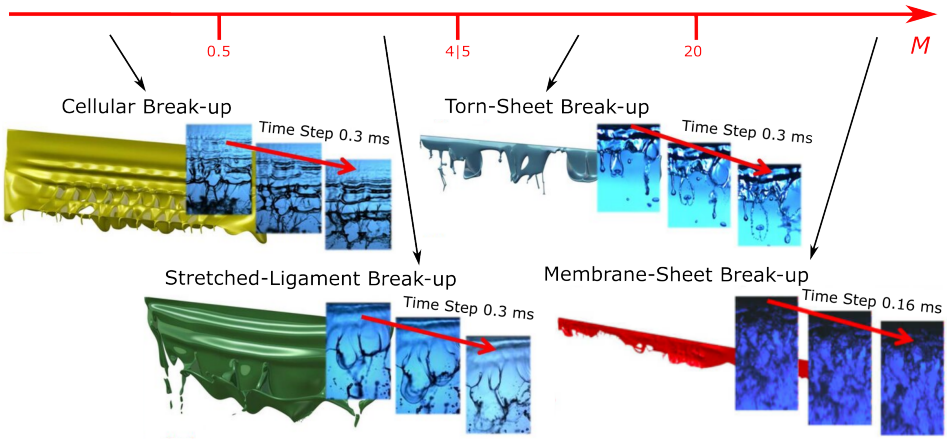

Figure 1.3: Mechanisms of liquid sheet atomization dominated by wave modes, adapted from [15].

The macroscopic behaviours shown in Figure 1.3 are the following:

- The cellular breakup mechanism occurs when gas velocity is low and liquid velocity is high. It is predominant for M values lower than 0.5 [25].

The dilatational mode can combine with the sinusoidal mode to create cells following a two-dimensional pattern. It forms spanwise ligaments and exhibits great penetration and a shallow spray angle.

- The stretched-ligament breakup happens as the value of M raises, having more influence of the sinusoidal mode compared to the longitudinal mode, which becomes negligible. This leads to a wider spray angle and a shorter breakup length. Empirical observations exhibit the formation of liquid bags carried by the gas which ultimately disintegrate into smaller droplets.

- The torn-sheet breakup takes place when M exceeds 4 [15] or 5 [26], forming liquid objects with similar characteristics but originating ligaments straight in the nozzle tip, and resulting in a "torn" profile.

- The membrane-sheet breakup is the result of M surpassing 20 [15]. This regime is characterized by the absence of any discernible pattern and shorter breakup lengths, producing considerably wider droplets distributions.

1.3 Case of study

Many researchers have performed experimental studies on actual annular configurations of airblast atomizers (compiled in Table 1.2). Jasuja [27] compared low- and high-shear design philosophies over a wide range of ambient air densities and kerosene flow rates at an ambient air temperature using Phase Doppler Interferometry and laser sheet imaging. Matsuura et al. [28] investigated the effects of ambient pressure (P_a) on Sauter Mean Diameter (SMD) for a counter double-swirl high-shear-type fuel injector at different air pressure drops, kerosene flow rates and air flow rate than Jasuja [27], using Phase Doppler Anemometry and laser sheet Mie scattering visualization. Gepperth et al [29] explored the coupling of the film flow and primary breakup process for an industrial prefilming airblast nozzle through high speed shadowgraphy. Two dimensionality reduction strategies were used for the first time to analyze the high resolution recordings of such atomizers: proper orthogonal decomposition (POD) and dynamic mode decomposition (DMD). Results revealed an independence between the extracted frequency of the precessing vortex core, film waves and atomization events for this range of operating conditions. In addition, a linear behaviour of the film flow dynamics was observed from the DMD analysis.

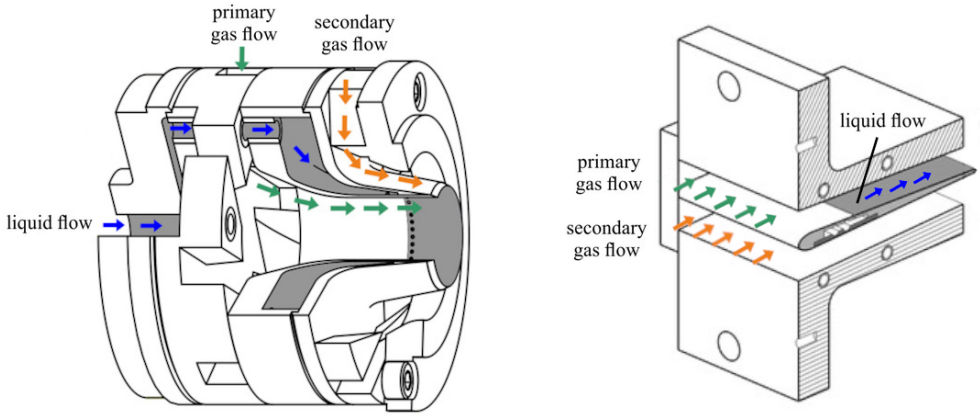

Figure 1.4: Prefilming airblast atomizer: annular configuration (left) versus planar configuration (right). Adapted from [30].

Nevertheless, the annular configuration of the airblast atomizer poses a multi-scale nature problem and presents some geometrical complexity, significantly hindering its study. In this sense, many efforts have been directed to planar configurations, which are much simpler and isolate the breakup phenomenon from other macroscopic effects. Conclusions obtained in those are then extrapolable to the real case due to an analogy by similarity, as pointed out by Berthoumieu and Lavergne [31] and confirmed by Holz et al. [32].

Focusing on the planar configuration, several test rigs have been developed to study the primary breakup in airblast atomizers (compiled in Table 1.3), generally using an airfoil-shaped solid section as a prefilmer. Inamura et al. [33, 34] used this sort of test rig with water as a working fluid under different operating conditions, establishing the primary breakup mechanism of these devices. Matas et al. [35] employed a similar setup to study the shear instability of a planar air-water mixing layer, demonstrating the direct influence of gas turbulence on this instability and showing that mean gas flow quantities do not fully characterize its features. The test rig in KIT-ITS [13], in turn, stands out as it has been used to carry out tests with diverse operating conditions and fuels through a variety of techniques, providing a huge experimental database. In this particular model, the airflow is divided into two ducts by the mentioned airfoil-shaped solid section and the fuel is injected through some holes equally distributed spanwise close to the leading edge of the upper surface. The fuel then develops as a planar liquid film reaching

the atomizing edge. Figure 1.5 shows a cross-section of the KIT-ITS test rig, whose parameters are defined in Table 1.1.

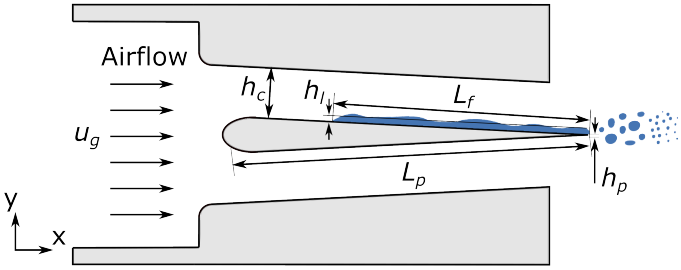

Figure 1.5: Sketch of the KIT-ITS test rig cross-section.

Table 1.1: Geometrical parameters of the planar prefilmer from the KIT-ITS test rig [13].

Description	Parameter	Value [mm]
Length	L_p	70.9
Span	b	50
Edge thickness	h_p	0.23
Channel height	h_c	8.11
Effective film length	L_f	47.6

A first set of experimental studies reported in the KIT-ITS test rig were conducted by Gepperth et al. [13, 14]. For a varied range of operating conditions (fluids, flow rates, prefilmer geometrical dimensions, ...), the influence of parameters like mean air velocity u_g, mean film height h_l or atomizing edge thickness h_p in primary atomization has been studied at ambient pressure and temperature using shadowgraphy, Phase-Doppler Anemometry (PDA) measurements and ligament tracking. The results showed a strong dependence of the mean droplet diameter on mean air velocity and atomizing edge thickness, these being the dominant parameters. Prefilming length, liquid physical properties and liquid volume flow rate had a weaker effect, but still affected the ligament formation process. From these results, correlations were derived to predict the breakup frequency, SMD and mean droplet velocities in the primary atomization region. Unlike previously existing models, their correlation did not require knowledge of film properties, which are difficult to estimate.

In addition to those experiments with steady conditions at the inlet, Chaussonnet et al. [36, 37] carried out similar tests at ambient temperature

and pressure but with fluctuating air flow instead, again using shadowgraphy and LDA velocimetry. A pulsating device generated velocity fluctuations of certain amplitude and frequency, corresponding to usual observed magnitudes in real combustion chambers. Results reported a significant influence on SMD up to a certain frequency, that is, a non-linear transfer function with a low-pass filter type of behaviour.

Results were later extended to higher ambient pressures through new experiments by Chaussonet et al. [38]. The aerodynamic stress $\rho_g u_g^2$ was used instead of the ambient pressure as a more appropriate parameter to characterize prefilming airblast breakup, and the domain was virtually split into several atomizing cells with single ligaments. Besides, two new characteristic lengths were proposed: one based on atomizing cell streamwise surface, related to the air velocity; and another one related to film loading, which showed a correlation with the SMD. This is in line with the idea from all previous works that, for some operating conditions corresponding to certain flow regimes, liquid accumulation is key to determine the primary spray characteristics. Many correlations from the literature were compared with these experiments, most of them underestimating SMD in their predictions. This emphasizes the need of calibrating models using experimental techniques like shadowgraphy [39].

As experimental studies are expensive and involve specialized facilities and resources, many researchers have delved into CFD to model primary atomization in pursuit of accuracy at lower costs (compiled in Table 1.4). Chaussonet et al. studied the prefilming airblast atomizer geometry through Large-Eddy Simulations (LES) to compare with Gepperth [14, 29] experimental results. They developed the Primary Atomization Model for prEfilming airbLAst injectors (PAMELA) and implemented it into the LES solver AVBP [40]. Considering the experimental observations, the droplet size distribution followed a Rosin-Rammler function with both scale and shape parameters depending on flow properties. The PAMELA model links these parameters with two Weber numbers based on the thickness of the atomizing edge and the boundary layer on the prefilmer (We_h and We_δ) and an extra function of h_p, obtaining five constants that are independent from the flow conditions. After calibration of these constants, they were able to predict mean and root-mean square (RMS) velocity profiles of the gas flow, capture the vortex shedding downstream of the atomizing edge and the drop size Probability Density Function (PDF) of the spray with moderate computational effort. Palanti et al. [41] also carried out LES of the study case, coupling Interface Capturing Methods (ICM) with the Eulerian-Lagrangian Spray Atomization (ELSA) approach with the OpenFOAM open source code [42]. Their objective was to catch the main features of the breakup mechanisms with a low-intensity computational strategy and

a novel postprocessing technique, relating curvature of the liquid interface to the droplet size PDF function.

To get a better understanding of the atomization process, other authors opted for Direct Numerical Simulations (DNS) as they can provide detailed information hardly achievable by current optical techniques. Nevertheless, accurate DNS of a full prefilming airblast atomizer geometry are unreasonable with current computational resources, even assuming the planar configuration simplification. To overcome this limitation, these authors relegated the domain to the last part of the prefilmer and the primary breakup zone.

Mukundan et al. [43] and Braun et al. [44] used constant velocity profiles for both the liquid and gas phases at the inlet boundary conditions, gaining some insight on the breakup mechanisms. However, Sauer et al. [45, 46] and Warncke et al. [47] introduced the concept of embedded DNS (eDNS). In this methodology some precursor LES are carried out in order to generate realistic boundary conditions for the gas phase at the DNS inlet. This way, the turbulent fluctuations of velocities are stored in planes that serve as input data for the final target simulation. Warncke et al. [48] specifically showed a strong influence of such turbulent inflow condition on the primary breakup process. Jiang and Ling [49, 50] later presented a work particularly devoted to analyzing the impact of gas turbulence intensity on the development and breakup of interfacial waves, demonstrating an effect of inlet gas turbulence on wave breakup location, dominant mode of breakup and size distribution of the resultant droplets. The method used in the latter works to solve the gas-liquid interface is the Volume of Fluid (VOF), in which an indicator function represents the liquid volume contained in a cell [51, 52]. The advantage of this method is its inherent mass conservation, at the cost of interface smearing. Carmona et al. [53] used the incompressible solver NGA [54] combining the VOF method with the Piecewise Linear Interface Capturing (PLIC) technique for interface reconstruction to study the KIT-ITS configuration, properly replicating the breakup mechanism while mantaining a limited CPU consumption.

Level-Set methods have also been used by other authors, but hybridizing them with the VOF method in the so-called Coupled Level-Set Volume of Fluid (CLSVOF) [43, 55–59] or with the Moment of Fluid method (CLSMOF) [59, 60] in order to counter the mass conservation limitations of the former and capture interface topology.

On the other hand, Lagrangian methods have also been used to model primary breakup in prefilming airblast atomizers. In particular, Smoothed Particle Hydrodynamics (SPH) has been successfully used in 2D [61, 62] and

3D [44] planar configurations. Being a meshfree method, it allows a significantly lower computational cost than grid-based simulations. This advantage is reduced when a high number of particles need to be tracked. As a drawback, the interpolation accuracy is influenced by particle arrangement.

Table 1.2: Experimental studies on the annular configuration of the prefilming airblast atomizer.

Author	Year	Techniques	Fluids	Op. conds.	Main findings
Berthoumieu & Lavergne [31]	2001	Backlight Stereoscopy	Air Water	$T_g = 298\,\mathrm{K}$ $P_g = 0.1\,\mathrm{MPa}$	Frequency oscillation is linear and related to liquid film thickness and velocities.The quantity of liquid can be estimated to calculate initial drop sizes.
Jasuja [27]	2006	PDI PIV	Air Kerosene	$T_g = 325\,\mathrm{K}$ $\rho_g = 14.5\,\mathrm{kg/m^3}$	The impact on spray SMD of increasing P_g varies significantly between low-shear and high-shear injector designs.
Matsuura et al. [28]	2008	PDA Mie scattering	Air Kerosene	$T_g = 325\,\mathrm{K}$ $P_g = 0.1 - 0.82\,\mathrm{MPa}$	Increasing P_a altered the spray pattern from conical to bell-like, but SMD did not vary significantly at a fixed m_f. For a fixed AFR, the dependence was strong on the injector type (low/high-shear).
Gepperth et al. [29]	2014	Shadowgraphy POD DMD	Air Shellsol D70	$T_g = 298\,\mathrm{K}$ $P_g = 0.1\,\mathrm{MPa}$	Linear behaviour of the film flow dynamics.
Holz et al. [32]	2016	Shadowgraphy PLTV	Air Shellsol D70	$T_g = 325\,\mathrm{K}$ $\rho_g = 14.5\,\mathrm{kg/m^3}$	Compare drop size distribution and SMD from experimental results with PAMELA model and confirm trends of planar prefilmers.

Table 1.3: Experimental studies on the planar configuration of the prefilming airblast atomizer.

Author	Year	Techniques	Fluids	Op. conds.	Main findings
Gepperth et al. [13, 14]	2010 2012	Shadowgraphy PDA PTV	Air Shellsol (D100, D70, D60, D40) Propanediol Prop-water	$T_g = 298\,\mathrm{K}$ $P_g = 0.1\,\mathrm{MPa}$	Strong dependence of mean droplet diameter on u_g and h_p, weak effect of liquid properties and volume flow rate. Correlations to breakup frequency, SMD and mean droplet velocities.
Inamura et al. [33, 34]	2012 2019	High-speed video	Air Water	$T_g = 298\,\mathrm{K}$ $P_g = 0.1\,\mathrm{MPa}$	Numerical model proposed where mean droplet diameter is determined by breakup of ligaments in the edge. Coincident with experiments except for low air velocity.
Matas et al. [35]	2015	Optical phase detection	Air Water	$T_g = 298\,\mathrm{K}$ $P_g = 0.1\,\mathrm{MPa}$	Strong impact of turbulence intensity in the gas stream on the shear instability. Breakup of waves affect drop formation.
Chaussonnet et al. [36–38, 40]	2016 2017 2018 2020	Shadowgraphy LDA PIV	Air Shellsol D70 Propanediol	$T_g = 298\,\mathrm{K}$ $P_g = 0.1 - 0.8\,\mathrm{MPa}$	PAMELA model development. Pulsating air velocity, non-linear transfer function with low-pass filter behaviour. Aerodynamic stress has strong influence on spray characteristics and liquid accumulation, independent of u_g and P_g. Momentum of injected liquid has no impact on atomization. SMD better predicted than PDA or LDT.

Table 1.4: Computational studies on the planar configuration of the prefilming airblast atomizer.

Author	Year	Multiphase treatment	Turbulence	Op. conds.	Main findings
Sauer et al. [45, 46]	2014 2016	Eulerian (VOF)	LES DNS	$T_g = 298\,\mathrm{K}$ $\rho_g = 1.2\,\mathrm{kg/m^3}$	Embed DNS methodology. Predominant primary atomization mechanisms depend on Re and We.
Chaussonnet et al. [40]	2016	-	LES	$T_g = 298\,\mathrm{K}$ $\rho_g = 1.2\,\mathrm{kg/m^3}$	Domain split into single ligament cells and film loading relation with SMD through PAMELA model.
Agbaglah et al. [58]	2017	Eulerian (CLSVOF)	LES DNS	$T_g = 298\,\mathrm{K}$ $\rho_g = 1.2\,\mathrm{kg/m^3}$	Inclination of gas inflow enhances primary atomization.
Koch et al. [61]	2017	Lagrangian (SPH, CSF)	DNS	$T_g = 298\,\mathrm{K}$ $\rho_g = 1.0\,\mathrm{kg/m^3}$	2D comparison of SPH vs VOF and experimental results. Accumulation at higher h_p increases droplet size and decreases frequency of droplet generation.
Zandian et al. [55–57]	2017 2018 2019	Eulerian (CLSVOF)	DNS	-	Interaction of streamwise and spanwise vortices produce liquid structures. Smallest length scale is determined by σ and liquid inertia more than ν_l. Gas inertia and σ are key parameters for spray angle and droplet size.
Holz et al. [62]	2018	Lagrangian (SPH)	DNS	$T_g = 293\,\mathrm{K}$ $P_g = 0.1\,\mathrm{MPa}$	2D simulations but many breakup phenomena is captured. 3 dwetting modes observed. Liquid film waves and ligaments breakup are slightly decoupled by liquid accumulation at h_p.

Warncke et al. [47, 48]	2017 2019	Eulerian (VOF, CSF)	LES DNS	$T_g = 298\,\mathrm{K}$ $\rho_g = 1.2\,\mathrm{kg/m^3}$	Underestimate large ligaments and droplets. 2D top view comparison with shadowgraphy experiments. Turbulent scales in the gaseous flow increase quantity of fine droplets.
Braun et al. [44]	2019	Lagrangian (SPH)	DNS	$T_g = 298\,\mathrm{K}$ $\rho_g = 1.0\,\mathrm{kg/m^3}$	Constant velocity profiles for liquid and gas inlet boundaries. Single event analysis of volumetric droplet diameters and SMD.
Mukundan et al. [43, 59, 60]	2019 2021	Eulerian (CLSVOF) (CLSMOF)	DNS	$T_g = 298\,\mathrm{K}$ $\rho_g = 1.2\,\mathrm{kg/m^3}$	Constant velocity profiles for liquid and gas inlet boundaries. Sheet breakup mechanism is dominant and 1D ligament lengths under-predicted.
Jiang and Ling [49, 50]	2020 2021	Eulerian (VOF, CSF)	DNS	$T_g = 298\,\mathrm{K}$ $\rho_g = 50\,\mathrm{kg/m^3}$	Effect of inlet gas turbulence on wave breakup location, dominant mode and droplet size distribution.
Palanti et al. [41]	2021	Eulerian (ICM-ELSA)	LES	$T_g = 298\,\mathrm{K}$ $\rho_g = 1.2\,\mathrm{kg/m^3}$	Breakup mechanisms using low computational resources and novel postprocessing technique.
Carmona et al. [53]	2021	Eulerian (VOF, PLIC)	DNS	$T_g = 298\,\mathrm{K}$ $\rho_g = 1.2\,\mathrm{kg/m^3}$	Longitudinal and transverse instability waves well predicted. 3 zones in film development, 2 breakup mechanisms identified.

1.4 Objectives

The purpose of this research is to study the primary breakup in airblast atomizers representative of aero engines by means of high-fidelity simulations. A numerical workflow is proposed to carry out non-reactive DNS simulations covering a wide range of relevant conditions in aero engines performance. Fulfilling the objective would place the foundations for a specific phenomenological model that could be able to reproduce the main characteristics of the spray with enough precision to be used for reactive flow simulations. Such a model could replace the existing primary breakup models in the literature, which are either theoretical or highly calibration-dependent experimental ones. This would be a great tool for improving combustors efficiency and reducing air pollutant emissions.

All in all, the specific objectives of this investigation are the following:

- To define a computational methodology in order to analyze the primary breakup process through DNS simulations, including any required adaptations to existing numerical tools.
- To define a post-processing strategy to extract and treat raw data from the simulations results, comparing relevant magnitudes like breakup length, breakup frequency, velocities and sizes of the liquid structures generated.
- To validate the computational methodology and the post-processing strategy implemented against experimental and computational data from the literature.
- To study the influence of the inlet boundary condition on the primary atomization due to the previous behaviour of the film in the precursor simulations.
- To study the influence of operating conditions on the primary atomization process, with different values of the relevant dimensionless numbers: Re, We, Oh and M.
- To propose an injection model based on the previous study that mantains its phenomenology and can be used in Lagrangian LES reactive flow simulations.

Chapter 2

Computational methodology

When it comes to multiphase flows, they can be studied from both experimental or computational point of view. The present work is based on Computational Fluid Dynamics (CFD), particularly using the finite volume method as it conserves mass, momentum and energy within each element. Nevertheless, experimental results from literature will be taken into account for validation purposes.

One of the key aspects of the CFD analysis is turbulence modelling. Turbulence is a chaotic and complex phenomenon characterized by irregular fluctuations in fluid properties that take place over a wide range of spatial and temporal scales. The cascade theory of energy in turbulence, first mentioned by Richardson [63] and extended by Kolmogorov [64], proposes that kinetic energy is transferred from large to smaller eddies until the energy is dissipated as heat at the smallest scales, as illustrated in Figure 2.1. The intermediate range between production and dissipation, i.e. inertial range, has a $k{-}5/3$ slope.

There are three main methods to treat turbulence that may have a significant impact on the outcome and computational cost of the simulation:

- Most CFD simulations currently use the Reynolds-Averaged Navier-Stokes (RANS) approach in which flow variables are averaged over a time interval, decomposing them into mean and fluctuating quantities. The Navier-Stokes equations can be solved with the mean magnitudes,

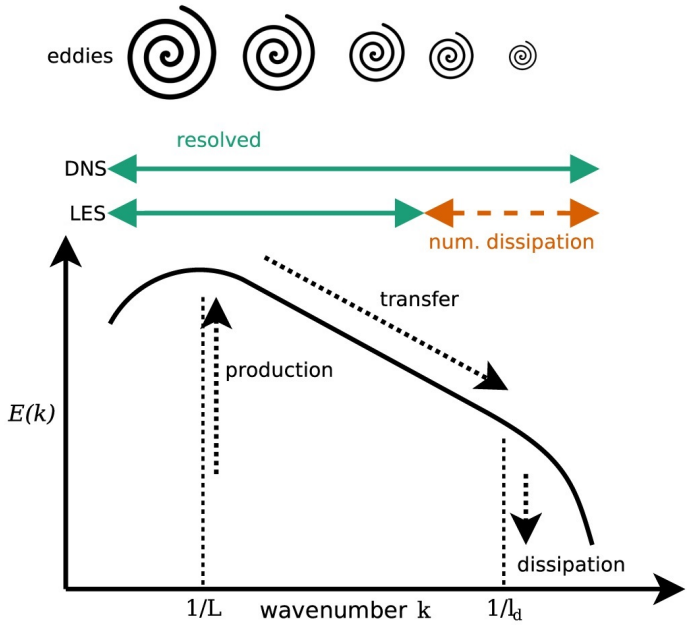

Figure 2.1: Illustrative sketch of the energy spectrum for idealized turbulence adapted from [65].

but additional equations are required to handle the turbulence spectrum. This set of additional equations is known as the turbulence closure model, and represent the correlation between the fluctuating velocity components and the Reynolds stress tensor. The accuracy of the RANS approach depends strongly on the turbulence model used.

RANS models are classified based on the number of additional equations and variables they introduce: e.g. $k-\epsilon$ or $k-\omega$ models propose two equations to solve turbulence kinetic energy and dissipation rate, but make simplifying assumptions to estimate eddy viscosity. RANS models are computationally efficient and easy to implement, but have firm limitations when dealing with complex turbulent flows.

- The Large Eddy Simulations (LES) approach applies an spatial or temporal filter to the Navier-Stokes equations in the inertial range, so the turbulence spectra is decomposed into large and small scales. Large scales (which contain most of the kinetic energy) are resolved, increasing computational cost and providing a more accurate representation of turbulence, but subgrid-scale models are employed for small dissipative

eddies. This is the method used to generate the boundary conditions for the main simulations of this work, as discussed in Subsections 2.2.1 and 2.2.2.

- Direct Numerical Simulations (DNS) approach solves the Navier-Stokes equations numerically without any turbulence model. As all the spatial scales must be resolved, including Kolmogorov microscales, the size of the elements in the computational mesh has to be small enough. Consequently, it has a strong limitation with domain size and complexity, as it is extremely computationally intensive. At the moment, its application is limited to academic and research cases because it provides the most accurate representation of the turbulence. The main simulations of the project are conducted with this method as stated in Subsection 2.2.3.

Due to the presence of different phases in the primary atomization problem, an additional treatment is required beyond that of single-phase CFD modeling. Given its importance, interface treatment will be adressed in Section 2.1 introducing some of the computational methods available for it. Numerical methods, spatial and temporal discretization of the domain, boundary conditions, etc. are explained in Section 2.2.

2.1 Overview of computational methods for interface treatment in primary atomization

The atomization problem is a particular case of two-phase flow where gas and liquid phases coexist, and the interface between them plays a crucial role in determining the behaviour of the system. For this reason, the interface treatment is particularly relevant in this problem and there are countless methods to deal with it.

Typically, these methods are classified according to the two main frames of reference to describe the motion of fluid particles: Lagrangian and Eulerian. On the one hand, the Lagrangian specification follows the motion of individual fluid particles as they move through space, treating the fluid as a collection of discrete particles and tracking their trajectories as they move with the flow. On the other hand, the Eulerian specification treats the fluid as a continuous medium and tracks its properties at fixed points in space as the fluid moves past them.

Figure 2.2 displays a scheme where many of these methods are classified. In the one-fluid model a single set of equations is solved to describe the behaviour

of both phases, in contrast to the two-fluid model where a separate set of equations is formulated for each phase. However, for illustrative purposes, this Section only focuses on some of the most commonly used methods for one-fluid models, which are enclosed in red: Front-Tracking, Volume-of-Fluid and Level-Set. Additionally, Figure 2.3 presents an example of how the interface is treated in each of them.

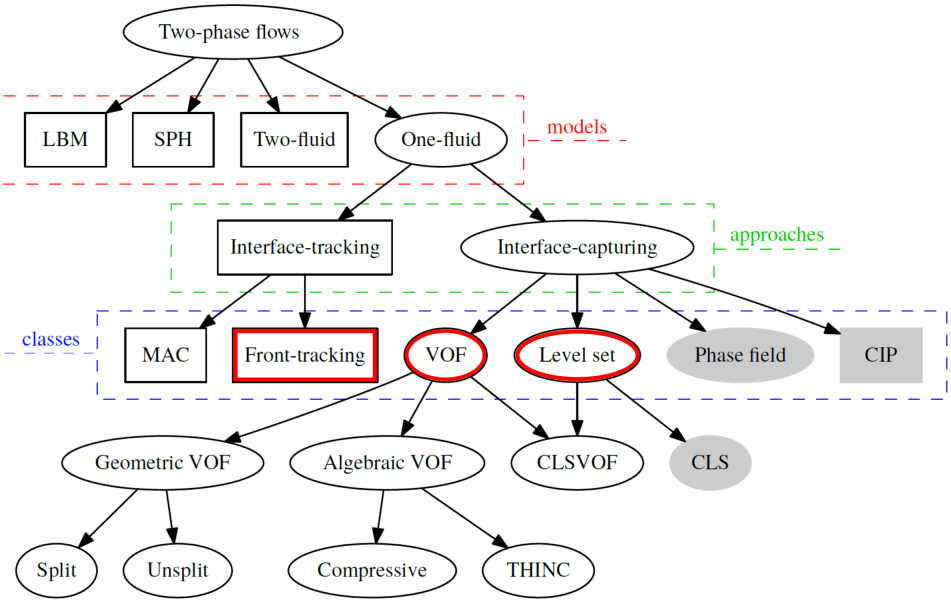

Figure 2.2: Scheme of numerical methods for two-phase flows adapted from [66]. Sharp-interface methods are distinguished by a white background, whereas diffuse-interface approaches are represented with a grey background.

2.1.1 Front-Tracking

A common interface-tracking method is Front-Tracking (FT) first proposed by Glimm et al. [68] and extended by Unverdi, Tryggvason et al. [69, 70]. According to the Lagrangian approach, it tracks the position of the interface between the fluids as it moves through space and evolves over time. The interface is divided into connected small segments called "fronts", represented as blue dots in Figure 2.3 a), and calculates the motion of each of them based on the local fluid properties and forces acting on them through the kinematic

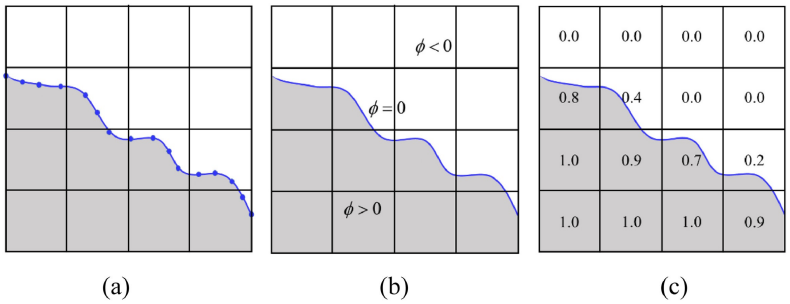

Figure 2.3: Diagram of three methods for interface tracking/capturing: a) Front-Tracking, b) Level-Set and c) Volume-of-Fluid (adapted from [67]). Blue line represents the interface between liquid (grey) and gas (white) phases.

equation (Equation 2.1).

$$\frac{\partial x_S}{\partial t} = u(x_S, t) \tag{2.1}$$

An Eulerian grid is still needed to locate said particles and determine fluid properties associated to each cell.

This method provides a precise representation of the interface simplifying the determination of surface curvature and forces, but it is not suitable for primary atomization as it has strong limitations treating with topological changes such as fluid fragmentation or merging [69], needing to re-mesh the surface in order to keep a valid description of it by its markers.

2.1.2 Level-Set

Another interface-capturing method is the Level-Set (LS) which uses a signed-distance function ϕ whose values are positive for one side of the interface, negative in the other side and 0 in the interface as shown in Figure 2.3 b). This function is transported with an advection equation (Equation 2.2) where $S = \dot{m}|\nabla\phi|$ is the mass transfer source term due to phase change across the interface.

$$\frac{\partial \phi}{\partial t} + \mathbf{u}^m \cdot \nabla\phi = S \tag{2.2}$$

The direction of this motion is normal to the surface, that can be calculated using Equation 2.3. Curvature is calculated using Equation 2.4.

$$\mathbf{n} = -\frac{\nabla\phi}{|\nabla\phi|} \tag{2.3}$$

$$\kappa = -\nabla \cdot \mathbf{n} \tag{2.4}$$

It is relatively easy to implement, since it does not require interface reconstruction or tracking and has a high degree of numerical stability. However, it is sensitive to the numerical algorithms that update the Level-Set function (like ENO), usually requiring the use of an initialization procedure for ϕ. However, implementations showed significant issues with mass conservation.

Many researchers have combined the LS method with Volume-of-fluid resulting in hybrid CLSVOF method [43, 55, 58, 59], or with Moment-of-Fluid resulting in CLSMOF [59, 60], in order to counter the LS inherent mass conservation limitations and capture interface topology, but losing its original simplicity and increasing computational cost.

2.1.3 Volume-of-Fluid

One of the most extended interface-capturing methods is the Volume-of-Fluid (VOF) [71]. This method has been chosen to perform the two-phase flow simulations in this thesis, as its advantages are inherent mass conservation, simplicity and efficiency; even though precision is limited by the resolution of the computational mesh, especially in regions with high shear and curvature [51, 52].

As an interface-capturing method, a marker function as the Heaviside (Equation 2.5) is used to avoid having two different meshes defining the solution. It is a discontinuous function that is often defined as 1 for the liquid and 0 for the gas. To describe the motion of the interface, the advection of the Heaviside function is shown in Equation 2.6.

$$H(x) = \begin{cases} 1 & \text{if inside a closed interface.} \\ 0 & \text{if outside a closed interface.} \end{cases} \tag{2.5}$$

$$\frac{\partial H(x)}{\partial t} + \mathbf{u}\nabla H(x) = 0 \tag{2.6}$$

In the particular case of the VOF method, the color function C is employed as the marker function, serving as a computational approximation of the Heaviside function in its implementation. Equation 2.7 shows the expression of C for a two-dimensional cell. Values of the color function vary between 0 and 1 as shown in Figure 2.3 c).

$$C_{ij} = \frac{1}{\Delta x \Delta y} \int_V H(x, y) dx dy \tag{2.7}$$

The Navier-Stokes equations are solved for the mixture phase where the color function of every cell is applied to weight the properties of both phases at the interface, as in Equations 2.8 (density and viscosity respectively).

$$\begin{aligned} \rho_{ij} &= \rho_l C_{ij} + \rho_g (1 - C_{ij}) \\ \mu_{ij} &= \mu_l C_{ij} + \mu_g (1 - C_{ij}) \end{aligned} \tag{2.8}$$

Unlike the previous method, the advection of the interface is the main issue of the VOF method (except for 1D problems). Both algebraic methods and geometric methods have been proposed for a proper interface advection. As far as the geometrical methods are concerned, various approaches have been developed to address this problem:

- Noh and Woodward [72] proposed the Simple Line Interface Calculation (SLIC) method where the interface is approximated using straight lines, parallel or perpendicular to the coordinate direction. These lines are computed in every direction, taking into account the color function value in the neighbour cells following the direction selected. Figure 2.4 b) shows an example of SLIC interface reconstruction.

- Hirt and Nichols [71] proposed a similar method than SLIC with parallel straight lines, but taking into account all neighbour cells and choosing the advection direction depending on surface normal components. It uses a combination of first-order upwind and downwind fluxes guaranteeing stability while minimizing diffusion. Figure 2.4 c) shows an example of the Hirt and Nichols interface reconstruction.

- DeBar [73] and Youngs [74] developed the Piecewise Linear Interface Calculation (PLIC) method, which also estimates the interface using straight line segments. Figure 2.4 d) shows an example of PLIC interface reconstruction. However, unlike the previous methods, these lines can extend in any direction, relying on properly computing the face normal vector $\mathbf{n}$ for every cell based on the values of C in the surrounding cells. Some of the algorithms that stand out to compute $\mathbf{n}$ are: Youngs' finite-difference method [75, 76], the height method [77], the Efficient Least Squares VOF Interface Reconstruction Algorithm (ELVIRA) [78] or the least-squares fit method [79].

Additionally, to compute the surface tension force term $\mathbf{f}_\sigma$ in the momentum equation (correspondingly divided by ρ), not only the normal vector $\mathbf{n}$ is

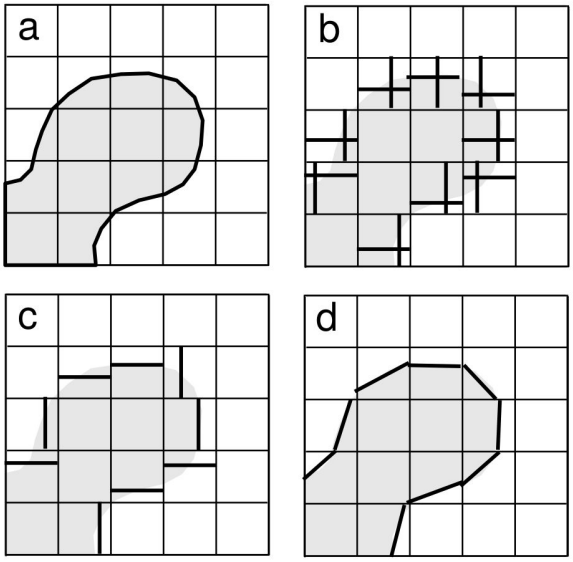

Figure 2.4: 2D surface reconstruction methods (image from [77]): a) The original interface, b) SLIC reconstruction, c) Hirt and Nichols reconstruction and d) PLIC reconstruction.

needed but also the curvature κ and the Dirac delta function δ_S that concentrates the effects of the surface tension on the liquid interface only:

$$\mathbf{f}_\sigma = \sigma\kappa\delta_S\mathbf{n} \tag{2.9}$$

In the VOF application δ_S can be approximated by $|\nabla C|$, but κ can be obtained with different methods:

- In the Continuous Surface Force (CSF) method by Brackbill et al. [80], curvature is estimated with the expression in Equation 2.10. It can achieve a precise balance between pressure and surface tension in certain cases, such as spherical droplets or round cylinders, but when the VOF color function is not continuous it needs to smooth the field (smoothed CSF). Despite its simplicity, this method can introduce noise and spurious current propagations, so it has been improved by Renardy and Renardy [81] in the Proper Representation Of Surface Tension (PROST) which employs quadratic curvature fitting but requires extra computational effort to obtain the least-squares curve.

$$\kappa = -\nabla \cdot \mathbf{n} \tag{2.10}$$

- The Height Function (HF) method first proposed by Torrey et al. [82] has been successfully tested in several studies [83–85] to perform curvature estimations. The process first involves determining the interface orientation by identifying the dominant component of the normal vector **n** and selecting an appropriate stencil for evaluation. Then the height function is obtained by summing the volume fractions in each column or row, and the local curvature can be calculated with centered finite differences with the Equation 2.11.

$$\kappa = \frac{h"}{(1 + h'^2)^{3/2}} \tag{2.11}$$

  Nevertheless, when the radius of curvature is similar to the mesh size this method becomes inconsistent, particularly in scenarios involving topology changes. In response to this issue, Popinet [85] introduced a solution in which, if the HF fails to accurately reconstruct the surface curvature due to irregularities in the C field, a fitting curve based on these points is employed to provide an estimation.

It is important to note that PLIC is used for reconstructing the interface in two-phase simulations from this thesis, but different algorithms are employed to compute **n** and κ, as it will be discussed in later Sections.

2.2 Proposed methodology for the case of study

This Section covers the details of both different approaches used in this work. They are shown in Figure 2.5: embedded DNS (eDNS) concept introduced by Sauer et al. [45] on the left and a proposed extension on the right to account for the film history upstream of the prefilmer edge.

In the former, single-phase flow LES simulations are carried out to account for the gas inflow turbulence generated upstream of the atomizing edge, along the prefilmer channel. Then, by mapping velocity data, this turbulence is embedded into the two-phase flow DNS simulations downstream of the prefilming edge. In this case, a constant liquid film thickness is established (Figure 2.5 left, $h_l \neq f(t, z)$ case). In Chapter 4, the study of the influence of operating conditions through this method is carried out.

In the latter, an additional two-phase flow LES simulation is proposed where the previously calculated gas turbulence is mapped to the air inlet and a constant liquid flow rate is introduced. This simulation develops the interaction between both gas and liquid phases, imitating the process taking

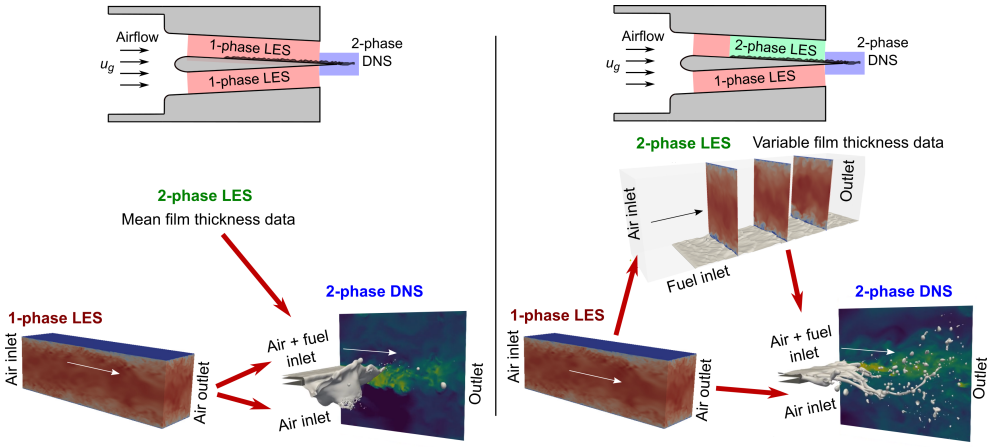

Figure 2.5: Simulation workflow of eDNS concept to account for gas inflow turbulence and a constant liquid film thickness at the DNS inlet (left, $h_l \neq f(t,z)$ case) and proposed workflow extension to account for the liquid film thickness evolution at the DNS inlet (right, $h_l = f(t,z)$ case).

place in the experimental setup and obtaining a liquid film thickness variation in time and space (Figure 2.5 right, $h_l = f(t,z)$ case). Hence, both the liquid film thickness variation and the velocity data are mapped from the two-phase flow LES to the DNS inlet. This extension of the eDNS method is analyzed in Chapter 3, as it constitutes one of the main original contributions from the present thesis.

For all three types of simulations required to carry out the two described approaches, the following Subsections present respectively the governing equations, meshing strategy and computational setup, as well as the post-processing techniques used. Validation against experimental or computational results in the literature for both single-phase and two-phase LES simulations are also present in this Section for the condition reported in Table 2.1. Hereinafter, this operating condition will be referred to as the *reference condition*. Finally, validation for two-phase DNS simulations and comparison between both approaches will be adressed in Chapter 3.

Dimensionless numbers for every condition are computed with Equations 1.1 to 1.4 particularized for this problem as follows. The Reynolds numbers are calculated according to Equations 2.12, where the half-channel height $h_c/2$ is chosen as the reference length for Re_g while the volumetric flow rate is used

Table 2.1: Functional parameters of the reference operating condition.

Description	Parameter	Value	Units
Temperature	T	298	K
Pressure	P	1	atm
Gas: Air			
Gas bulk velocity	$\overline{u_g}$	50	m/s
Gas density	ρ_g	1.21	kg/m^3
Gas dynamic viscosity	μ_g	1.82×10^{-5}	Pa · s
Liquid: Shellsol D70			
Liquid normalized volumetric flow rate	$\dot{V}/b$	50	mm^2/s
Liquid mean velocity	$\overline{u_l}$	0.5	m/s
Liquid density	ρ_l	770	kg/m^3
Liquid dynamic viscosity	μ_l	1.56×10^{-3}	Pa · s
Liquid surface tension	σ	0.0275	kg/s^2
Density ratio	r	636.36	-
Gas Reynolds number	Re_g	13 480	-
Liquid Reynolds number	Re_l	24.63	-
Weber number (traditional)	We_l	8.62	-
Weber number (based on atomizing edge)	We_h	25.30	-
Weber number (based on boundary layer)	We_δ	151.48	-
Ohnesorge number	Oh	0.022 35	-
Momentum flux ratio	M	15.71	-

for Re_l.

$$Re_g = \frac{\rho_g \overline{u_g} h_c/2}{\mu_g} \qquad Re_l = \frac{\rho_l \dot{V}/b}{\mu_l} \tag{2.12}$$

As far as the Weber numbers are concerned, their definitions are in Equations 2.13, where the main differences come from the characteristic dimension considered.

$$We_l = \frac{\rho_g(\overline{u_g} - \overline{u_l})^2 h_l}{\sigma} \qquad We_h = \frac{\rho_g \overline{u_g}^2 h_p}{\sigma} \qquad We_\delta = \frac{\rho_g \overline{u_g}^2 \delta_{TE}}{\sigma} \tag{2.13}$$

For We_l, the relative mean velocity between gas and liquid $\overline{u_g} - \overline{u_l}$ is used while h_l is estimated from the volumetric flow rate and later verified in the computed two-phase LES. The interest of We_h, which uses mean gas velocity $\overline{u_g}$ and atomizing edge thickness h_p, resides in the fact that Chaussonnet et al. [40] found that the SMD in part scales with $1/\sqrt{We_h}$. On the other hand, We_δ is based on the boundary layer thickness at the prefilmer trailing edge

δ_{TE}, which is in turn estimated according to Equation 2.14 by analogy to a turbulent boundary layer on a flat plate [86]:

$$\delta_{TE} = 0.16 \frac{L_f}{Re_{Lf}^{1/7}} \tag{2.14}$$

where Re_{Lf} is a specific gaseous Re based on the effective film length (Table 1.1) as the relevant dimension. The Ohnesorge number is obtained using the liquid properties and the prefilmer edge thickness h_p as in Equation 2.15:

$$Oh = \frac{\mu_l}{\sqrt{\rho_l \sigma h_p}} \tag{2.15}$$

Finally, the momentum flux ratio is calculated directly with Equation 1.7, but the density ratio has been inversely defined as $r = \rho_l/\rho_g$ for illustrating purposes.

It is important to emphasize that the proposed methodology relies on the assumption that the flow in each region represented by a simulation is one-way coupled. This may be true if the interfacial instability generated in the planar airblast atomizer is convective, so that perturbation only propagates downstream of the instability source. But if the instability is absolute, the internal and external flows will be two-way coupled, meaning it also influences the flow upstream of the instability source. Fuster et al. [87] investigated the transition between both regimes generated in a similar configuration (a splitter plate among planar air–water coflowing sheets), finding the threshold between regimes to be governed by the dynamic pressure ratio and the density ratio. In particular, for a density ratio $r = 10$ the study reports a critical momentum flux ratio $M = 8$ above which the interfacial instability is absolute, but this value decreases to $M = 1$ for $r = 1000$. From here, it follows that the operating conditions analyzed in the present study are deemed to trigger an absolute instability, constituting a limitation for this methodology. However, this drawback may be addressed including part of the prefilmer surface upstream of its edge in the DNS domain, so that at least the film in this region is influenced by the interfacial instability. Despite not fully accounting for the effects of the absolute interfacial instability, the comparison of the spatiotemporal film thickness evolution from the two-phase precursor LES against available experimental data will show the extent of validation of the methodology from a practical standpoint.

2.2.1 Precursor single-phase flow LES

2.2.1.1 Governing equations and related submodels

To solve the transient incompressible and turbulent channel flow along the planar prefilmer duct, the Pressure-Implicit with Splitting of Operators (PISO) algorithm [88] is used through the *pisoFoam* solver in the OpenFOAM open source CFD toolbox [42]. It solves Equations (2.16) and (2.17) as the filtered governing equations for continuity and momentum conservation, respectively:

$$\nabla \cdot \bar{\mathbf{u}} = 0 \tag{2.16}$$

$$\frac{\partial \bar{\mathbf{u}}}{\partial t} + \nabla \cdot (\bar{\mathbf{u}}\bar{\mathbf{u}}) = -\frac{1}{\rho}\nabla \bar{P} + \nabla \cdot \left[(\nu + \nu_{SGS})\,\nabla \bar{\mathbf{u}}\right] \tag{2.17}$$

Closure on the filtered governing equations is achieved through the subgrid scale viscosity ν_{SGS}, which is modelled by the Wall Adapting Local Eddy-viscosity (WALE) sub-grid scale (SGS) model from Nicoud and Ducros [89].

2.2.1.2 Computational domain and mesh

Figure 2.6 shows the geometrical dimensions of the computational domain and the mesh for the turbulent channel. The domain height in the wall-normal y direction replicates the full prefilmer channel height from the KIT-ITS test rig, h_c. The width in the spanwise z direction is chosen as $\pi/2 \cdot h_c$, according to Moser et al. [90]. The domain length in the streamwise x direction is $\pi \cdot h_c$, even though a periodic boundary condition is set in the streamwise edges in order to virtually mimic an infinitely long channel.

A zonal mesh strategy with hexahedral cells is adopted as in the work by Sauer et al. [46] using *blockMesh* [91]. Figure 2.6 (left) shows the geometry of the domain and the direction of the flow. The grid spacing is uniform in the streamwise and spanwise directions for every mesh zone, but a symmetric cell-size grading is applied in the wall-normal y direction to refine the domain from the channel core to the walls. Figure 2.6 (right) presents the number of cells and a grading coefficient for all the 3 zones. This grading coefficient g_c is the proportion between the sizes of the first and last cell in that zone, following the arrow direction: $g_c = \frac{cell_0}{cell_N}$. The intermediate cell size increases or decreases linearly. A $y^+ < 1$ condition is fulfilled at the walls, preventing the use of wall functions. This strategy yields a total of 20.1 M cells for the reference condition.

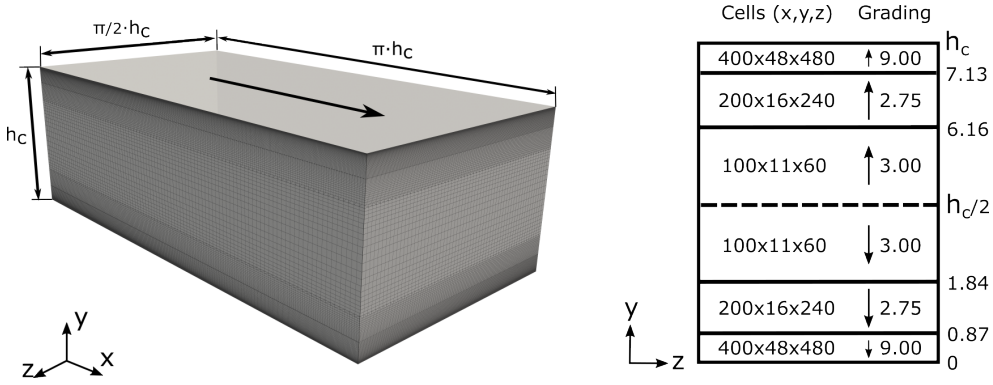

Figure 2.6: Geometry and mesh sketch for the single-phase turbulent channel flow LES (left) and detail of the number of cells and cell grading in each of the mesh zones (right).

2.2.1.3 Boundary conditions and discretization schemes

As far as the boundary conditions are concerned, nominal gas velocity is initially prescribed at the inlet (X- boundary) by a Dirichlet boundary condition, whereas a Neumann boundary condition is used at the outlet (X+ boundary). A no-slip condition is used at the bottom and top walls (Y- and Y+ boundaries) and a periodic condition is used spanwise (Z- and Z+ boundaries). The *boxTurb* tool from OpenFOAM [92] is used to initially trigger turbulence in the domain, generating a divergence-free random initial velocity field consistent with the mesh that accelerates the initialization process. After a transient, both the inlet and outlet boundaries (X- and X+) are also converted into periodic boundary conditions. This configuration mimics an infinitely long turbulent channel where turbulence can develop to simulate the prefilmer channel. After more than 25 washout times in this virtually infinite configuration, the resultant turbulent velocity field is independent from the initialization, and may be passed on to the subsequent simulations according to Figure 2.5 workflow. To this end, velocity data are sampled at the central YZ plane of the domain every 1 µs.

All chosen discretization schemes are 2^{nd} order in space and time. As far as time discretization is concerned, a backward scheme (also known as 2^{nd} order upwind Euler scheme [93]) is used, which replaces the time derivative of

a flow property ϕ as given by Equation 2.18:

$$\frac{\partial \phi}{\partial t} \rightarrow \frac{3\phi - 4\phi_{t-1} + \phi_{t-2}}{2\Delta t} \tag{2.18}$$

Space discretization is needed for the divergence, laplacian and gradient operators of the convective, diffusive and pressure terms of Equation 2.17, respectively. In this regard, OpenFOAM's Finite Volume Method (FVM) makes use of the Gauss theorem to convert cell-based volume integrals of a field divergence to surface integrals of the related vector field over the volume surface (i.e. flux across cell faces). Since flow properties are stored at the cell centroids after each time step in a collocated arrangement, the advection of a flow property ϕ requires the computation of cell face fluxes, for which interpolation from adjacent cell centroids is required. Linear interpolation of ϕ to the cell faces is chosen in what is known as a *Gauss linear* 2^{nd} order scheme. Laplacian discretization also requires the computation of surface-normal gradients at cell faces. The surface normal gradients of a property ϕ are also computed by linear interpolation of the property from cell centroids to the cell faces, normalized by the distance among cell centroids. The same procedure is used for the discretization of the pressure gradient term. It must be noted that during the PISO loop for pressure-velocity coupling, the calculations are done with pressure at the cell centroids and the velocity components being interpolated at cell faces to compute the flux across them, thus in a staggered fashion. For further details on OpenFOAM's predefined discretization schemes, the reader is referred to Greenshields and Weller [94].

Finally, a Geometric Agglomerated Algebraic Multi-Grid (GAMG) is used as the linear solver. The time step is let to vary during simulation runtime, being set by restricting the maximum CFL number to 0.6. For the reference operating condition of Table 2.1, this results in time steps in the order of 1×10^{-7} s.

2.2.1.4 Post-processing and validation

For illustrating purposes, Figure 2.7 shows an example of the instantaneous data samples in a YZ plane, where the spatial variability of each velocity component can be appreciated.

The velocities gathered in the YZ plane are spatially averaged over the Z axis and temporally averaged (a 5.6 ms window in the reference condition) in order to analyze the wall-normal velocity profile and whether it conforms with the law of the wall. Results for the mean dimensionless streamwise velocity

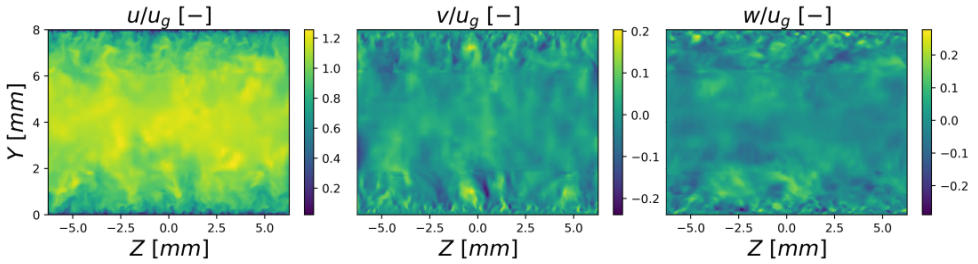

Figure 2.7: Snapshots with the three normalized components of the velocity at $t = 2.5\,\text{ms}$ for the reference condition. Note the different scale in each case.

profile in the reference condition ($Re_\tau \approx 685$) are shown in Figure 2.8 (left), where they are also compared to the theoretical law of the wall and to accepted turbulent channel flow DNS data by Iwamoto et al. [95] (being $Re_\tau \equiv 650$ the closest value available in the literature). LES data show a reasonable agreement with the theoretical relations, with a smooth transition from the viscous sublayer to the log-law region. The agreement is comparable to that of a DNS computation, highlighting the level of resolution achieved by this precursor LES.

The root mean square (RMS) of each velocity component are similary computed and averaged. Their wall-normal evolution is plotted against Iwamoto's

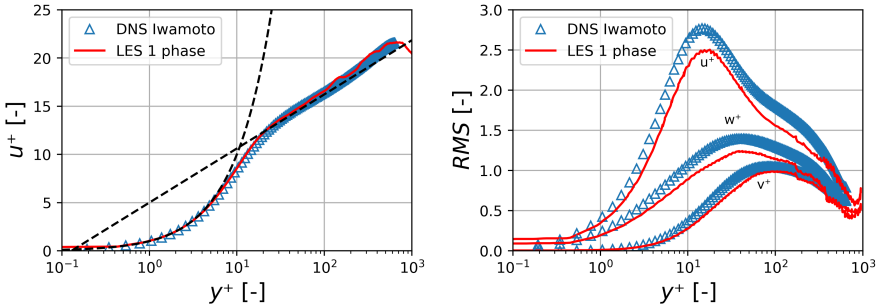

Figure 2.8: Comparison of a single-phase LES temporally and spatially averaged velocity results against DNS data from Iwamoto et al. [95]: non-dimensional mean streamwise velocity profile (left, with the theoretical law of the wall sublayers also depicted in black), non-dimensional root mean square velocity components (right).

DNS data in Figure 2.8 (right) with a similar level of agreement, although a slight underprediction is present for all components.

Additionally, the turbulence spectra were also analyzed through the autocorrelations of the velocity components to ensure sampled data correspond to a statistically steady time series and no artificially induced frequencies are passed on to subsequent simulations.

2.2.2 Precursor two-phase flow LES

2.2.2.1 Governing equations and related submodels

In order to solve the transient two-phase flow the *interFoam* solver within OpenFOAM is used. It applies the VOF interface-capturing approach mentioned in Section 2.1.3, which introduces the cell liquid volume fraction $\alpha = V_l/V_{cell}$ as a variable and advects it according to Equation 2.19.

$$\frac{\partial \bar{\alpha}}{\partial t} + \bar{\mathbf{u}} \cdot \nabla \bar{\alpha} + \bar{\mathbf{u_c}} \cdot \nabla \left[\bar{\alpha}\left(1 - \bar{\alpha}\right)\right] = 0 \tag{2.19}$$

This equation is derived combining the separate mass conservation equations for both phases, under the assumptions that both of them are incompressible, isothermal and immiscible. Hence, the consideration is made that the flow velocity normal to the interface is zero. The last term in Equation 2.19 is an artificial compression term that only acts in the vicinity of the interface (i.e. it is different than zero only when $0 < \alpha < 1$), creating a flux that counters numerical diffusion keeping a sharp interface [96]. The velocity vector $\boldsymbol{u_c}$ is defined according to Equation 2.20:

$$\mathbf{u_c} = C_\alpha \left|\mathbf{u}\right| \mathbf{n} \tag{2.20}$$

where C_α is a binary coefficient that switches interface sharpening on (with a value of 1) or off (with a value of 0), and $\mathbf{n}$ is the interface unit normal vector, used to define the direction of the applied compression velocity and determined by Equation 2.21:

$$\mathbf{n} = \frac{\nabla \alpha}{|\nabla \alpha|} \tag{2.21}$$

In this work C_α has been set as 1 so that interface sharpening is active. Additionally, the geometric method PLIC is used for interface advection while surface tension is modelled through CSF (see Section 2.1.3).

Last, the WALE SGS model is again used to model sub-grid turbulence. Since this model was originally conceived for single-phase flow, this does not allow for a full modeling of the subgrid terms arising from the two-phase flow filtered equations, thus being a source for uncertainty. Noteworthy advances have been performed by the scientific community developing such models specific for two-phase flows [97–99], but they have not yet been benchmarked in practical engineering flows applications. Future works should count on these specific submodels to increase the reliability of the predictions.

2.2.2.2 Computational domain and mesh

Figure 2.9 shows the geometry considered for the computational domain of the two-phase channel flow, together with the mesh used. The domain dimensions keep the full channel height h_c in the wall-normal y direction. In the streamwise x direction, there is enough space from the fuel inlet (included at the bottom of the domain) to the domain outlet for the film to develop half of the prefilmer effective film length L_f. Including some space to separate

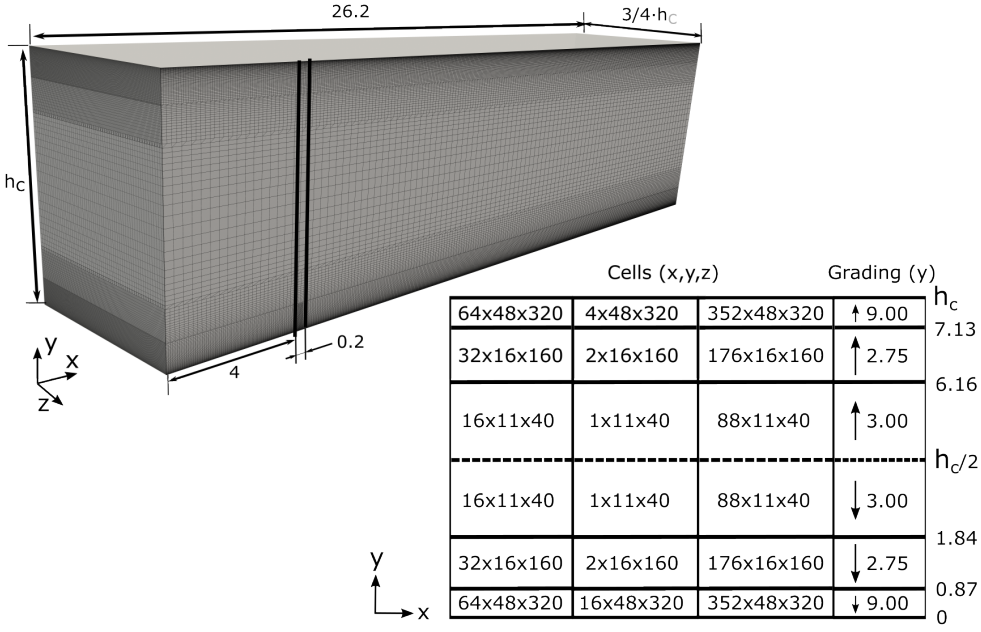

Figure 2.9: Geometry and mesh sketch for the two-phase turbulent channel flow LES.

the fuel inlet from the air inlet, this yields a total length of 26.2 mm. Since the mesh in this case is finer than the one for the single-phase flow precursor LES, the width in the spanwise z direction is chosen as $3/4 \cdot h_c$ (nearly half of the single-phase flow precursor LES) in order to keep a limited amount of computational resources.

A zonal mesh strategy is utilized again. A cell-size grading is prescribed in the wall-normal y direction, similar to the one used in the single-phase flow precursor LES. In this case, however, an additional refined zone is added at the lower part of the domain in order to better represent the gas-liquid interface. This yields a 4-step sequence from the wall-normal domain center to the bottom, keeping the condition of $y^+ < 0.9$ at the top and bottom walls, again preventing the use of wall functions. A local refinement is added at the streamwise location where the fuel inlet is placed. The grid spacing is uniform in the spanwise direction, but a slight grading is applied streamwise towards the outlet. This strategy yields a total cell count of 21.4 M cells for the reference condition.

2.2.2.3 Boundary conditions and discretization schemes

Air velocity is provided at the gas inlet (X- boundary) as a Dirichlet boundary condition with time-varying data mapped from the single-phase LES simulation, linearly interpolating among sampled planes. The fuel inlet at the Y- boundary occupies part of the streamwise direction and is uniformly distributed spanwise, so as to replicate the uniform fuel injection achieved upstream of the prefilmer edge at all operating conditions in the KIT-ITS test rig. A Dirichlet boundary condition is also used, liquid velocity being imposed according to the inlet area in order to prescribe the flow rate. A Neumann boundary condition is used at the domain outlet (X+ boundary). A no-slip condition is used at the bottom (except for the fuel inlet region) and top walls (Y- and Y+ boundaries) and a periodic condition is again used spanwise (Z- and Z+ boundaries).

This configuration mimics the upper part of the KIT-ITS planar prefilmer so both the liquid film waves and the air-fuel boundary layer may be passed on to the subsequent atomizing edge DNS according to Figure 2.5 (right) workflow. To this end, velocity and liquid volume fraction data are sampled at a YZ plane close to the domain outlet every 2 µs.

The pressure-velocity coupling is again solved using the PISO algorithm. The Multidimensional Universal Limiter for Explicit Solution (MULES) method within *interFoam* is used to solve for the liquid volume fraction advection given by Equation 2.19. This method uses a Flux-Corrected Transport

(FCT) algorithm [100] and ensures the boundedness of the solution thanks to a predictor-corrector procedure. As it happened for the single-phase precursor LES, the chosen discretization schemes are 2^{nd} order in time and space. The Crank-Nicolson method [101] is now used for the temporal discretization of α in Equation 2.19, whereas the vanLeer scheme [102] is chosen for the MULES limiter. The fully discretized version of Equation 2.19 using MULES and the description of the predictor-corrector procedure used in this investigation are given by Kim et al. [103]. The discretized version of the momentum equation using *interFoam* is given by Deshpande et al. [104].

The Geometric Agglomerated Algebraic Multi-Grid (GAMG) is again used as the linear solver. A fixed time step of 5×10^{-8} s is used in the reference case, ensuring the maximum CFL number never surpasses 0.25. The resulting time steps are also checked to comply with additional criteria for capillary velocity and viscosity constraints in order to reduce the growth of spurious currents as stated by Deshpande et al. [104], even though they state this phenomenon not to be a major issue for inertia-dominated flows.

It must be noted that the chosen interface compression and curvature evaluation methods are in general not as physically accurate as interface reconstruction methods (such as PLIC) and other curvature approaches (such as Height Functions, used in subsequent DNS simulations, or hybridization with the Level Set method). However, it must be considered that the precursor two-phase flow LES does not look at solving for liquid atomization, but for the inertia-dominated free-surface flow, where the exact reproduction of curvature is not deemed to be critical. Hence, the fact that the chosen method is mass conservative [96] is the reason for its choice towards coupling with the two-phase flow DNS. This approach for the VOF method and curvature handling has been succesfully validated elsewhere for two-phase wave simulation with an orthogonal mesh [103].

2.2.2.4 Post-processing and validation

For the two-phase flow LES, results were analyzed once the liquid injection transient was finished. Figure 2.10 (left) shows the qualitative appearance of the film for a given instant of the reference condition. Normalized velocity data at three different YZ planes are shown to illustrate the influence of the liquid film on the gaseous phase velocity, as a liquid-gas boundary layer is developed. Figure 2.10 (right, top) depicts a side view of the liquid film. Vorticity magnitude data at the mid XY plane is shown, where it may be seen how the liquid-gas interaction along the film crests and valleys generates additional vortex to the ones generated at the gas-wall boundary layer on the

upper wall. These vortex also spread for a larger distance from the film in the wall-normal direction than they do in the case of the gas-wall interaction. This fact also highlights the generation of a thicker boundary layer among liquid and gas. A top view of the film is also shown in Figure 2.10 (right, bottom) to complete the qualitative appearance of the liquid film, showing the wavy behavior with crests and valleys being shaped and propagated in the streamwise direction. Several wave crests or valleys can be contained in the spanwise direction.

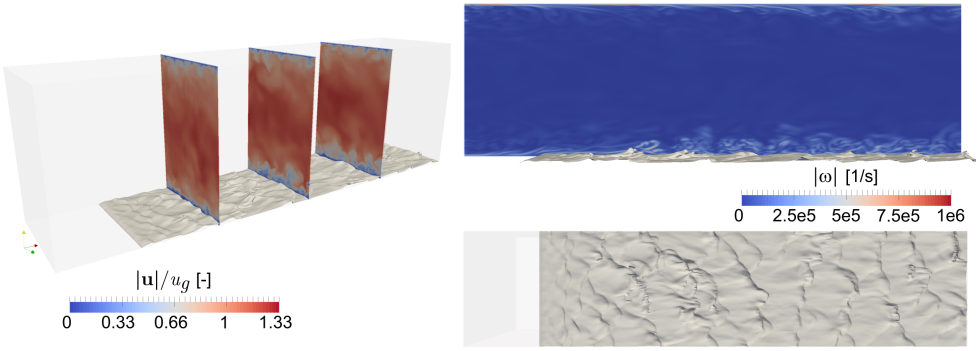

Figure 2.10: Qualitative appearance of the liquid film on the prefilmer depicted through a $\alpha = 0.5$ iso-surface for a given time instant. 3D representation with velocity data at three different streamwise locations (left), side view with vorticity magnitude in a mid-plane (right, top), top view (right, bottom).

In this case, liquid volume fraction α data sampled at the three YZ planes and at the domain mid-plane XZ were processed to compute the liquid film height at all locations and their temporal evolution. The analysis allowed determining that data at the $x = 2 \cdot h_c$ location is already not influenced by the inlet boundaries and thus can be passed on to the atomizing edge DNS. As a parametric study is performed in Chapter 4, computational results of those additional operating conditions are also shown in this Section for illustrating purposes, including additional gas velocities ($\bar{u}_g = 20\,\mathrm{m/s}$ and $\bar{u}_g = 70\,\mathrm{m/s}$) and an additional liquid (a $H_2$0-1,2-Propanediol mixture) which is denser ($1008 > 770\,\mathrm{kg/m^3}$), more viscous ($0.00606 > 0.001\,56\,\mathrm{Pa\,s}$) and has a higher surface tension ($0.0466 > 0.0275\,\mathrm{kg/s^2}$) than Shellsol D70. For further details on these conditions, the reader is referred to Chapter 4 (Table 4.2).

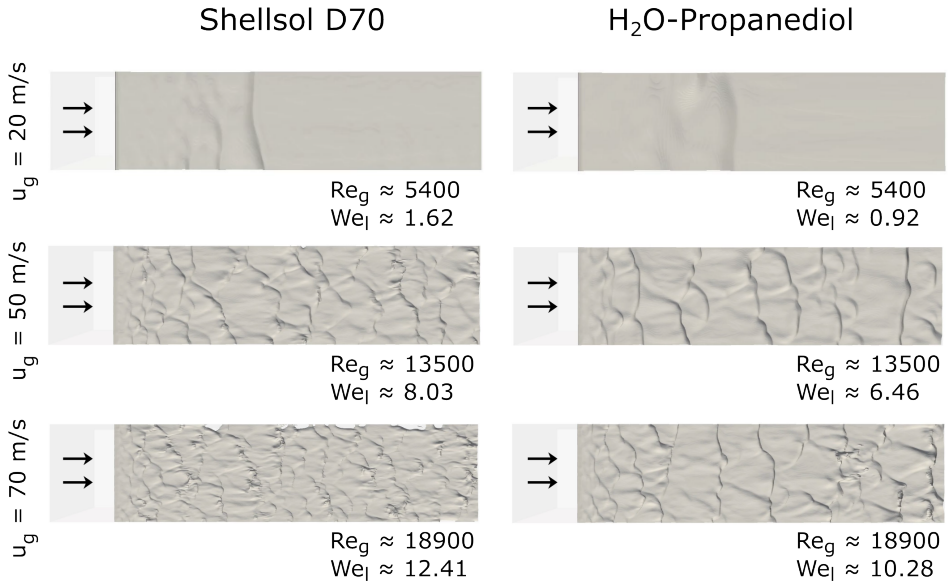

Figure 2.11: Qualitative top view comparison of the liquid films between different operating conditions.

A qualitative comparison between these conditions is presented in Figure 2.11, from where some trends are identified. When increasing velocity (and therefore, Re_g values) for a given liquid, more waves emerge on the surface. Comparing both liquids for a given velocity, the denser one experiences slightly less rippling than the other. This comparison also reveals that the higher We_l is, the more the liquid film wrinkles.

The temporally averaged mean liquid film height and the corresponding standard deviation found at this location are plotted in Figure 2.12 against experimental data for similar conditions reported by Gepperth et al. [13]. Further averaged results at this location are displayed in Table 2.2. It must be stated that the mean temporal frequency value obtained by the LES in the reference condition ($\overline{f_{film}} = 585.9\,\text{Hz}$) is also very close to the one reported by Holz et al. [62] ($\overline{f_{film}} = 595\,\text{Hz}$) for the same operating condition.

Computational results are thus compatible with available literature data. The model is sensitive to the variations in global inputs, as given by the expected trends: for a given fluid, mean film thickness decreases with the mean gas velocity; whereas for a given gas velocity, mean film thickness increases

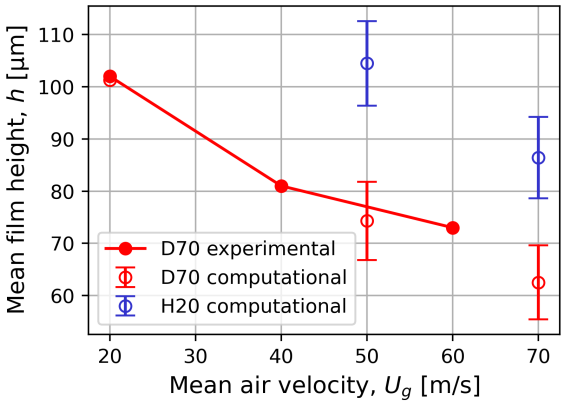

Figure 2.12: Mean film height $\bar{h_l}$ as a function of the bulk gas velocity for the simulations and experimental data. Computational values, gathered for two different fluids, were obtained at $x = 2 \cdot h_c$ and also depict the standard deviation σ_{hl} (both temporally and spatially along the Z axis) from the mean film height. Experimental data were reported for Shellsol D70 and the same normalized volumetric flow rate [13].

Table 2.2: Temporally averaged data for the 2-phase flow LES at $x = 2 \cdot h_c$, where $\bar{u}_g$ is the gas bulk velocity, $\overline{h_l}$ and σ_{hl} are the mean and standard deviation of the film height respectively, $\overline{f_{film}}$ is the mean film wave frequency and $\overline{\lambda_{film}}$ is the mean film wavelength. Reference condition is in bold.

Parameter	Units					
Liquid	-	**Shellsol D70**			H_20-1,2-Propanediol	
$\bar{u}_g$	m/s	20	**50**	70	50	70
$\overline{h_l}$	μm	101.3	**74.3**	62.5	104.5	86.4
σ_{hl}	μm		**7.5**	7.1	8.1	7.8
$\overline{f_{film}}$	Hz		**585.9**	822.8	435.9	554.6
$\overline{\lambda_{film}}$	mm		**2.28**	1.99	2.59	2.61

with increasing liquid density, viscosity and surface tension (i.e. decreasing We_l). The standard deviation with respect to the mean value is similar among moderate gas velocities cases, but the value could not be reported for $\bar{u}_g = 20\,\mathrm{m/s}$, as a long simulation time is needed to account for a statistically significant number of wave peaks. As far as the film wave frequencies are concerned, they increase with increasing gas velocity and decrease for the denser, more viscous fluid.

The predictions by this precursor 2-phase flow LES are successfully validated by these means, considering that the proposed methodology implies one-way coupling among simulations so that the effect of the interfacial instability generated by the prefilmer edge on the upstream flow is not accounted for. The averaged value of h_l is passed on to the $h_l \neq f(t,z)$ atomizing edge DNS, whereas sampled data are provided to the $h_l = f(t,z)$ case.

2.2.3 Two-phase flow DNS

2.2.3.1 Governing equations and related submodels

To solve the incompressible, isothermal and immiscible two-phase flow at the atomizing edge with a Direct Numerical Simulation (DNS) approach, the PARIS (PArallel, Robust, Interface Simulator) code [105] was used. It applies the Navier–Stokes equations in the one-fluid formulation of two-phase flow, using the finite volume approach with mass and momentum conservation, and including also the surface tension forces term:

$$\rho \left[\frac{\partial \mathbf{u}}{\partial t} + \nabla \cdot (\mathbf{uu}) \right] = -\nabla p + \mu \nabla^2 \mathbf{u} + \sigma\, \kappa\, \delta_S\, \mathbf{n} \tag{2.22}$$

The VOF method (see Section 2.1.3) is used to capture and advect the interface following Equation 2.23, leaving aside the artificial interface compression term introduced in the two-phase precursor LES (Equation 2.19).

$$\frac{\partial \alpha}{\partial t} + \mathbf{u} \cdot \nabla \alpha = 0 \tag{2.23}$$

In contrast to the two-phase precursor LES, the Calcul d'Interface Affine par Morceaux (CIAM) approach [76] is used to advect the interface. CIAM is French translation for PLIC, but while PLIC refers to generic methods with a piecewise linear reconstruction step, CIAM refers to a particular type of advection method also named Lagrangian Explicit. To reconstruct the interface, the normal vector $\mathbf{n}$ is computed with the Mixed-Youngs-Centered scheme (MYC) [106], while the curvature κ is estimated through the Height

Functions (HF) approach [85]. These methods are mentioned in Section 2.1.3, however for full implementation details in PARIS the reader is referred to the work by Aniszewski et al. [105].

2.2.3.2 Computational domain and mesh

The geometry of the atomizing edge DNS domain is showed in Figure 2.13 and its dimensions are compiled in Table 2.3. These dimensions are very similar to the ones used in comparable computations in the literature [43, 45, 47, 59, 60]. Including a prefilming length (L_p), rather than directly mapping the data from the precursor simulations at the prefilming edge axial location, allows the film to evolve on the prefilmer surface accounting (to a limited extent) for the absolute nature of the interfacial instability. Additionally, the prefilmer edge thickness h_p was shown in Table 1.1. As per the liquid film thickness, the value used depends on the two-phase LES simulations: a constant value is used in the $h_l \neq f(t, z)$ case whereas it fluctuates in the $h_l = f(t, z)$ case.

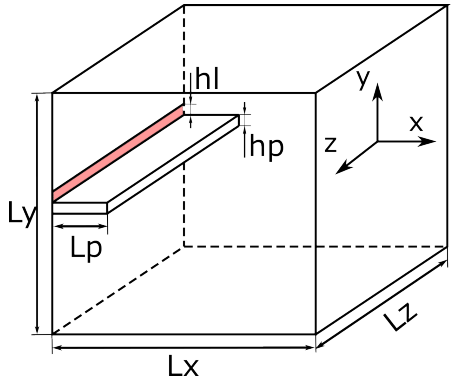

Figure 2.13: Atomizing edge DNS computational domain.

A fixed Cartesian grid is used by PARIS, which is easily generated and parallelized. The resulting cubic control volumes have pressure collocated at the cell centres and velocities located at the face centers. This kind of grid is known as *staggered grid*, and when used for incompressible flows it has some advantages over using a collocated one (where all variables are stored in cell centres): they simplify conservative methods (mass and momentum), increase accuracy as it performs on kind of a finer grid and provide less numerical fluctuations [77].

The calculated $Re_\tau = 267$ for the reference condition and the integral length scale $l_0 = 0.8\,\text{mm}$ (set to 20% of the channel half height $h_c/2$) yields

Table 2.3: Main dimensions of the atomizing edge DNS computational domain.

Description	Parameter	Value [mm]
Domain length	L_x	6.08
Domain height	L_y	6.08
Domain span	L_z	4.00
Prefilming length	L_p	1.00

a Kolmogorov length scale $l_\eta = 12\,\mu m$ (Equation 2.24), implying a minimum grid spacing of $\Delta x_{min} = 25\,\mu m$ according to Pope's criterion [107] (Equation 2.25). Sauer et al. [46] had performed a detailed discussion about the droplet representation with different grid sizes (20 µm and 10 µm). They found that a resolution of the entire liquid mass is hardly achievable, but that the 10 µm cell size allowed a resolution of 80% of the liquid mass. This resolution matches the one by Warncke et al. [47].

$$\frac{l_\eta}{l_0} \sim Re_\tau^{-3/4} \tag{2.24}$$

$$\frac{\Delta x_{min}}{l_\eta} = \frac{\pi}{1.5} \approx 2.1 \tag{2.25}$$

According to these previous studies, a mesh sensitivity study was planned to test the reference condition with three different cell sizes: 20 µm, 10 µm and 5 µm. In the first case, convergence problems were experienced, being unable to get more than a single atomization event. Furthermore, a problem of dewetting appeared in this simulation, in contrast with the experimental results reported in the literature. Consequently, its origin was not physical but numerical instead, due to the lack of resolution in the liquid film. For the 5 µm case, computational cost was higher than the resources available for the project, so the cell size 10 µm was finally chosen, resulting in 147.87 M cells for the reference condition.

The lack of sensitivity study has been addressed by reproducing the reference simulation as close as possible in the Basilisk [108] CFD code, which shares most of the numerical methods and schemes, the VOF approach, as well as the same developers with PARIS Simulator. The main advantage is that Basilisk, contrary to PARIS Simulator, can use an Adaptive Mesh Refinement (AMR) tool based in octrees, which allows refining the grid only in certain interesting locations instead of the whole domain. This may reduce

the numerical effort required for the DNS simulations while mantaining similar precision in the results, opening a way to actually perform a mesh sensitivity study.

For the sake of continuity in the text, the mesh sensitivity study in Basilisk is reported in Appendix A. While the study revealed no mesh independence in the targeted results, it allowed concluding that mesh refinement by itself did not grant a better reproduction of the experimentally observed breakup mechanisms than the proposed methodology.

2.2.3.3 Boundary conditions and discretization schemes

A Dirichlet boundary condition is provided at the inlet (X- boundary), with time-varying velocity data mapped from the precursor LES in the $h_l \neq f(t,z)$ case, and both time-varying velocity and liquid volume fraction α in the $h_l = f(t,z)$ case. Linear interpolations among temporally sampled planes are used in both cases. A special convective and time-varying boundary is used in the outlet (X+ boundary) to reduce reflections [109], as expressed in Equation 2.26, where u_m is computed at each time step as the average streamwise velocity at the inlet.

$$\frac{\partial u_i}{\partial t} + u_m \frac{\partial u_i}{\partial x} = 0 \tag{2.26}$$

For the bottom and top bounds (Y- and Y+ boundaries) a slip boundary condition (i.e. moving wall) is used with a streamwise velocity equal to the mean gas velocity. This condition allowed containing major flow vortices, with the chosen L_y dimension ensuring no influence on the region of interest for primary atomization. A periodic condition is used spanwise (Z- and Z+ boundaries).

Last, a no-slip boundary condition is used for the immersed boundary (prefilmer solid wall). A static contact angle among the prefilmer solid wall and the liquid has been introduced as a VOF condition to account for wettability. As formulated by Lacis et al. [110] following Legendre & Maglio's work [111], this boundary condition is mathematically set by defining the interface normal unit vector at the boundary ($\mathbf{n}$) through Equation 2.27 wherever the interface is attached to the prefilmer wall:

$$\mathbf{n} \cdot \mathbf{n_{wall}} = \cos(\theta) \tag{2.27}$$

where $\mathbf{n_{wall}}$ is the wall-normal unit vector. A contact angle $\theta = 60°$ has been set between the liquid and the prefilmer according to Braun et al. [44].

In the case of spatial discretization, the QUICK algorithm [112] is used, and the diffusive flux is solved with a 2nd order central scheme as in Equation 2.28:

$$\phi_{face} = \frac{6}{8}\phi_{i-1} + \frac{3}{8}\phi_i - \frac{1}{8}\phi_{i-2} \tag{2.28}$$

For temporal discretization, the Chorin projection-correction method [113] is used, involving two steps. Equation 2.29 expresses the variation of the velocity field separated into two terms, one for every step. Superscripts n and $n+1$ refer to the current and the next time steps, and $\mathbf{u}^*$ is the intermediate velocity field.

$$\frac{\partial \mathbf{u}}{\partial t} = \frac{(\mathbf{u}^{n+1} - \mathbf{u}^*) + (\mathbf{u}^* - \mathbf{u}^n)}{\Delta t} \tag{2.29}$$

In the first step, the velocity field is projected using Equation 2.22 without the pressure gradient, obtaining the intermediate velocity field $\mathbf{u}^*$ which is generally not a divergence-free field. Equation 2.30 presents a first-order formulation of this step simplified for readability, where A is the advection term, D is the diffusion term and F is the forces term.

$$\frac{(\mathbf{u}^* - \mathbf{u}^n)}{\Delta t} = -A^n + \frac{D^n + F^n}{\rho^n} \tag{2.30}$$

The second step corrects that velocity field using the pressure gradient as shown in Equation 2.31, and the divergence of this equation results in the Poisson equation expressed with no dependance of $\mathbf{u}^{n+1}$ (Equation 2.32).

$$\frac{(\mathbf{u}^{n+1} - \mathbf{u}^*)}{\Delta t} = \frac{-\nabla p}{\rho^n} \tag{2.31}$$

$$\nabla \cdot \left(\frac{\nabla p}{\rho^n}\right) = \frac{\nabla \mathbf{u}^*}{\Delta t} \tag{2.32}$$

The algorithm is repeated twice and the final result is averaged to extend this method to the 2nd order.

A variable time step is used ensuring the maximum CFL number never surpasses 0.2 (limited to a maximum of 2×10^{-8} s), requiring 0.21M core-hours per each millisecond of simulated physical time in the reference condition.

For a more detailed description of time and spatial discretization schemes, the reader is referred to [77, 105].

2.2.3.4 Post-processing methods

Different post-processing tools have been implemented and applied to the atomizing edge DNS data in order to generate and analyze quantitative results.

The first step to post-process the DNS data is to identify each individual continuous liquid structure. This is done scanning the whole domain looking for free surfaces according to an α threshold. A parametric study of these threshold values was conducted by Crialesi et al. [114] to investigate the impact on the detected droplet size distribution. Higher values lead to underestimation of larger droplets (mainly ligaments), while lower values lead to lower number of small droplets detected (most of them without physical meaning, as they are close to the simulation mesh size). Figure 2.14 (left) shows a sample visualization of the instantaneous liquid-gas interface through an iso-contour of $\alpha = 0.5$. After a binarization using that threshold, the connectivity algorithm from The Visualization Toolkit (VTK) [115] is applied to the domain for all time steps in order to identify every isolated liquid structure, obtaining their position and size. Once this is achieved, the intact core is identified as the first structure (including the film and any ligament directly attached to it, as shown in Figure 2.14 right) and separated from the droplet cloud and any detached ligaments. This way, the intact core and ligaments can be independently processed on the one hand, whereas the droplet characteristics can be analyzed on the other hand.

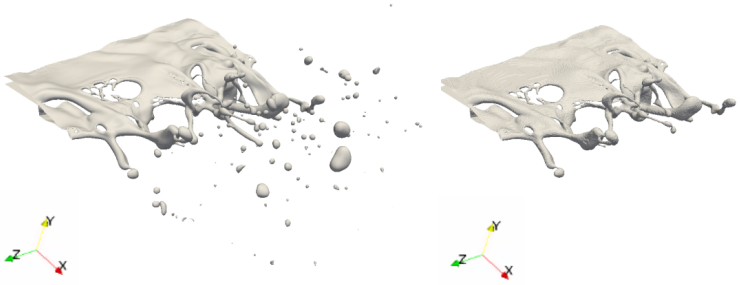

Figure 2.14: All liquid structures identified in the domain for a given instant of the reference condition through an iso-surface of $\alpha = 0.5$ (left), liquid core extracted through the connectivity algorithm (right).

Intact core and ligament analysis

As far as the ligaments are concerned, it must be noted that experimental results available in the literature provide 2D shadowgraphy images [14, 38,

47]. Hence, as a first approach, the liquid data from the DNS is projected on the XZ plane in order to obtain comparable images for validation purposes. Below are the steps to identify the 2D ligaments:

- First, the liquid projection is obtained by aggregating the values of the α variable along the Y axis at each XZ plane location. The resulting data is binarized with a chosen threshold ($\alpha = 1$), yielding images such as the one labelled as Step 1 in Figure 2.15.

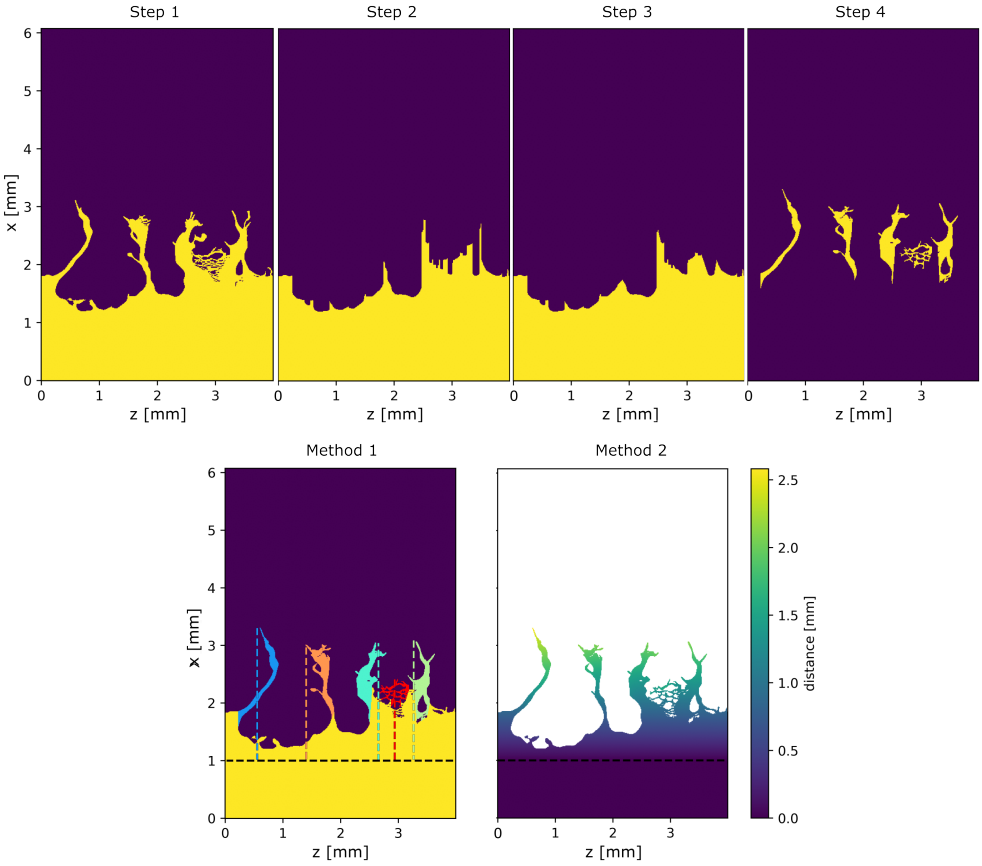

Figure 2.15: Steps for 2D ligament analysis (top): liquid core and ligaments projected over the XZ plane and binarized (Step 1), mask construction (Steps 2 and 3) and isolated ligaments obtained (Step 4). Methods for ligament length measurement (bottom): Axial distance method (Method 1) and Fast Marching Method (Method 2). Images correspond to a given instant of the $h_l \neq f(t, z)$ case.

- Then, the isolated ligaments must be extracted from the intact core or liquid film. The method proposed to this end is as follows. For each Z coordinate, a function expressing the number of liquid cells before the first gas cell along the X axis is computed (Figure 2.15 Step 2).
- Next, large slopes are detected with the derivative of this function and erased with a cutting and smoothing algorithm, obtaining the main liquid core except for the elongated structures (Figure 2.15 Step 3).
- This structure is then used as a cutting mask, substracting it from the projected domain from Step 1 and obtaining the ligaments as isolated structures, noise being removed by deleting structures with very small areas (Figure 2.15 Step 4).
- Finally, each ligament is labeled using the connectivity algorithm from OpenCV [116].

Once a ligament is characterized, the cell with the maximum X coordinate is considered to be the tip of that ligament. With that information, there are two methods for measuring string length $L_{str2D,i}$ as shown in Figure 2.15 (bottom):

- Method 1 (left) considers the ligament length as the axial distance between the prefilmer edge and the ligament tip, following a straight line in the X direction. This is the simplest method and is also used in the literature shadowgraphy experiments and the simulations by Warncke et al. [47]. Hence, it has been used to validate the computations of the present work.
- Method 2 (right) uses the *distance* function of the *scikit-fmm* package in Python, which is an implementation of the Fast Marching Method by Sethian et al. [117] to solve an Eikonal equation. Defining the prefilmer edge as a propagating surface, and setting the same constant velocity for every node in the domain, it returns a distance matrix that is equivalent to the continuous shortest path along ligament connectivity points between the prefilmer edge and each ligament cell. This post-processing method proposed stands as a primary contribution in this thesis.

In this work, ligament length data are complemented with ligament velocity data. During the 2D ligament projection step, at each XZ plane location, liquid velocities are obtained by adding the values of velocity along the Y axis

weighted by α. An example of the resulting velocity projected data for a given time step is shown in Figure 2.16. Velocity data at the tip of each ligament i ($\mathbf{u_{str2D,i}}$) are obtained from this projection.

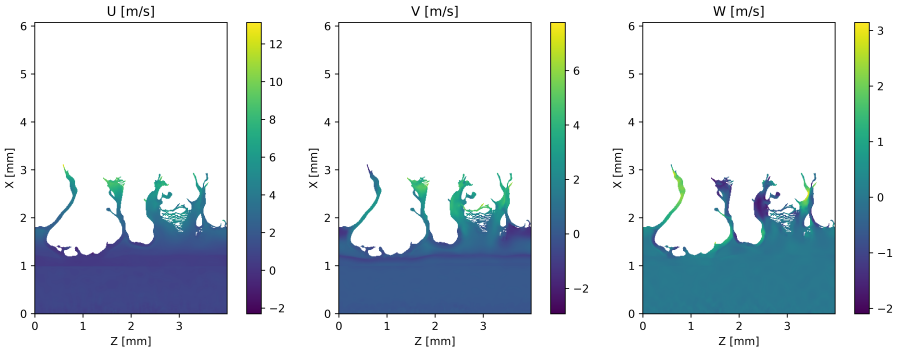

Figure 2.16: Liquid core velocity components projected on the XZ plane for a given time step of the $h_l \neq f(t,z)$ case.

Besides, a characteristic streamwise velocity of the liquid film is also computed according to the procedure by Warncke et al. [47]. From the liquid volume projection (Figure 2.15 Step 1) of a given time step t_k, the furthest location of the attached liquid ($x_{max,zk}$) is determined for each z position. The streamwise deformation velocity at each z location is directly computed among time steps t_k and t_{k-1} as $u_{def,zk} = (x_{max,zk} - x_{max,zk-1})/\Delta t$. The characteristic film deformation velocity of the t_k time step ($u_{def,k}$) is then defined by the 90% percentile of all $u_{def,zk}$ locations.

After 2D data for validation are obtained, a novel 3D methodology is proposed to prevent DNS information loss during the projection step. The objective is to preserve the 3D nature of the ligaments both in terms of ligament size and tip velocity components for a more realistic description of these structures. To this end, the cutting mask obtained in the 2D analysis is extruded along the Y axis so it can be used as a 3D cutting mask. When applied to the connected liquid in the domain, only the ligaments are left. It is then possible to apply another connectivity filter, identifying ligaments sizes and positions as depicted in Figure 2.17. Properly locating ligaments and the film in the 3D domain in this way then allows processing string tips, string lengths $L_{str3D,i}$ with the Fast Marching Method (Method 2), and the velocities $\mathbf{u_{str3D,i}}$ directly from the DNS output data. This 3D procedure represents one of the main contributions of the present thesis to the post-processing of liquid structures in sprays.

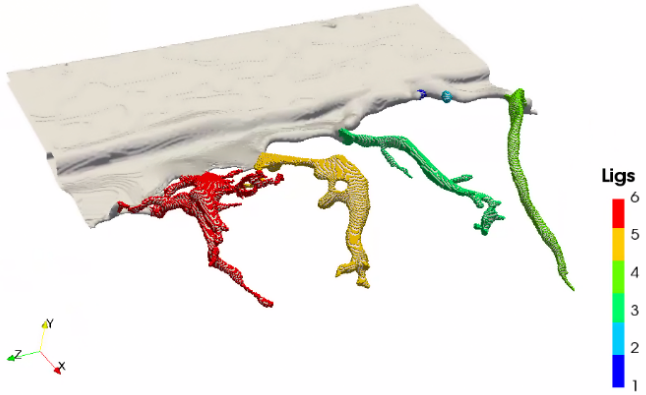

Figure 2.17: Sample of ligament detection in the 3D domain for a given time step of the $h_l \neq f(t,z)$ case.

Regardless of the geometrical treatment given to the ligaments (2D and 3D), some additional quantities derived from their features can be used to globally characterize the breakup process. A global breakup length is defined by averaging ligament lengths for all time steps ($L_{bu} = \overline{L_{str}}$) and a mean ligament tip velocity can be computed by averaging ligament velocities for all time steps ($\mathbf{u_{lig}} = \overline{\mathbf{u_{str}}}$). Besides, a mean film deformation speed is also computed as the average among time steps ($u_{def} = \overline{u_{def,k}}$). From these quantities, a mean breakup frequency (f_{bu}) is estimated according to Equation 2.33 [47]:

$$f_{bu} = \frac{u_{def}}{L_{bu}} \tag{2.33}$$

Finally, in the case of the 3D analysis, an equivalent diameter of each ligament can be defined from their determined length and volume according to Equation 2.34:

$$d_{eq,i} = \frac{V_{lig,i}}{L_{str3D,i}} \tag{2.34}$$

Droplet cloud analysis

Focusing on the droplet cloud, it has been processed through the same method used and validated by Crialesi-Esposito et al. [114] for a round spray, which is here summarized. Taking the assumption of spherical droplets, each individual droplet i is assigned its volumetric diameter according to Equation

2.35, where the droplet i liquid volume ($V_{drop,i}$) is calculated as the sum of the liquid volume for every cell j belonging to the droplet. This can be seen in Equation 2.36, where $Ncells$ is the number of cells representing droplet i and V_{cell} is constant since all cells in the domain are of equal size.

$$d_{V,i} = \sqrt[3]{\frac{6}{\pi} V_{drop,i}} \tag{2.35}$$

$$V_{drop,i} = \sum_{j=1}^{Ncells} \alpha_j V_{cell,j} = V_{cell} \cdot N_{cells} \cdot \sum_{j=1}^{Ncells} \alpha_j \tag{2.36}$$

Droplet velocities are computed as weighted averages of the velocity from each cell j composing the droplet as shown in Equation 2.37, using the liquid volume fraction as the weighting factor after some simplification.

$$\mathbf{u_{drop,i}} = \frac{\sum_{j=1}^{Ncells} \alpha_j \cdot V_{cell,j} \cdot \mathbf{u_j}}{\sum_{j=1}^{Ncells} \alpha_j \cdot V_{cell,j}} = \frac{\sum_{j=1}^{Ncells} \alpha_j \cdot \mathbf{u_j}}{\sum_{j=1}^{Ncells} \alpha_j} \tag{2.37}$$

Any other droplet characteristics of interest (local Re, local We, etc.) can be computed from these magnitudes. Probability density function (PDF) graphs of both diameters and velocities are provided and analyzed in Chapters 3 and 4. Droplets with $d_V < 20\,\mu m$ are discarded from the analysis for two reasons: it is the smallest droplet size detected by the reference experiments used for validation [47] and this value corresponds to twice the cell size realized by the proposed DNS simulations.

Chapter 3

Accounting for the influence of film history on the primary atomization process

In this Chapter, the results of the atomizing edge DNS simulations (in the reference condition) for both strategies proposed in Section 2.2 are analyzed to find out the influence of the film previous history in the primary breakup process: the eDNS concept to account for gas inflow turbulence with a constant liquid film thickness at the inlet, $h_l \neq f(t,z)$, compared to the proposed extension of the method with a variable liquid film thickness at the inlet, $h_l = f(t,z)$. Table 3.1 summarizes the names of the cases of study and the main differences between them.

Table 3.1: Cases of study of the influence of film history on the primary atomization process.

Case	Air velocity	Liquid velocity	Film thickness
$h_l \neq f(t,z)$	Variable	Constant	Constant
$h_l = f(t,z)$	Variable	Variable	Variable

The parameters of the reference condition and the dimensions of the domain in these simulations were presented in Tables 2.1 and 2.3 respectively. The mean film height used in the $h_l \neq f(t,z)$ case is $h_l = 0.08\,\text{mm}$ (corresponding to the rounded value obtained in the precursor two-phase LES),

whereas it fluctuates in the $h_l = f(t, z)$ case, this being the object of investigation. Computations were run with 4096 CPU cores for a total simulated time of about 9 ms, so that 3 main breakup events were accounted for in both cases (a first event was discarded, as it corresponds to a simulation transient).

A qualitative analysis is carried out in Section 3.1, describing the atomization mechanism and comparing the appearance of the cases. Next, a quantitative analysis of the ligament development and the generated droplet clouds is conducted in Section 3.2. Finally, Section 3.3 summarizes the main findings of this study.

3.1 Qualitative analysis

Figure 3.1 illustrates the temporal evolution of the flow for a given breakup event of both simulated cases. To this end, it represents a series of snapshots depicting the evolution of the airblasted sheet.

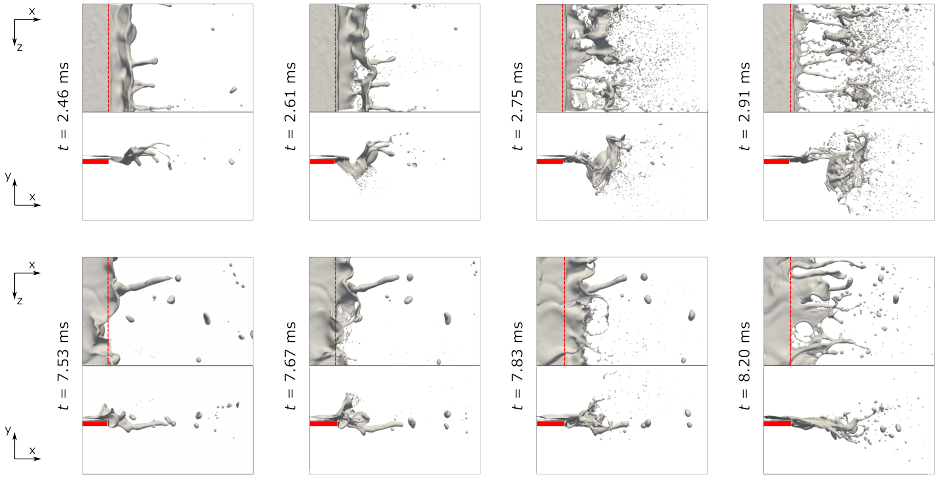

Figure 3.1: Time sequence of the DNS results for the $h_l \neq f(t, z)$ case (top) and the $h_l = f(t, z)$ case (bottom). The liquid is depicted through an isosurface of $\alpha = 0.5$, and the prefilmer is in red.

Focusing on the $h_l \neq f(t, z)$ case on the one hand, the breakup mechanism phenomenology already described in the literature [14, 38, 40, 46, 47] is reproduced. First, the liquid transported along the prefilmer tends to accumulate behind the prefilmer edge, generating a liquid reservoir ($t = 2.46$ ms).

Two structures then emanate from this reservoir: elongated structures (ligaments) on the one hand, and most importantly a liquid sheet that tends to flap upwards or downwards. This liquid sheet then gets exposed to the free gas stream coming from above or below the prefilmer surface, shaping bag-like structures (observed at $t = 2.46\,\text{ms}$ and $t = 2.61\,\text{ms}$) that keep growing in size. Eventually, surface tension cannot keep the bag structures attached to the liquid sheet, so they get punctured and break into droplets in the so-called *bag breakup* ($t = 2.61\,\text{ms}$ and $t = 2.75\,\text{ms}$). Additionally, some rims are shaped from the sides of the bag structures ($t = 2.75\,\text{ms}$), generating separated ligaments that also break into droplets ($t = 2.91\,\text{ms}$). Some of these ligaments keep attached to the liquid film that starts generating a new reservoir behind the prefilmer edge. If these ligaments do not detach among main breakup events, they get thicker by receiving some liquid transported from the film (back to $t = 2.46\,\text{ms}$). Therefore, in the end, droplets are generated by two main mechanisms: bag breakup, which generates a large amount of small droplets only during the main breakup events; and ligament breakup, which generates a lower amount of relatively bigger droplets, some of them still being generated among breakup events. The coexistence of these distinct breakup mechanisms and the importance of the liquid accumulation process is justified considering the value of the momentum flux ratio ($M = 15.7$) achieved for this operating condition, getting a *torn-sheet breakup* (recall Figure 1.3).

On the other hand, a look at the $h_l = f(t, z)$ case highlights the qualitative differences when accounting for the liquid film history upstream of the prefilmer edge. In this case, the liquid film above the prefilmer surface appears more wrinkled than in the $h_l \neq f(t, z)$ case, as a consequence of the two-phase LES data mapping procedure. Therefore, the reservoir behind the prefilmer edge is less uniformly distributed spanwise than it was for the constant film thickness case, as the film crests and valleys do not reach the reservoir in a synchronized manner (recall Figure 2.10). As a result, by the time a bag is formed and flapping, not the complete prefilmer span is filled with enough liquid to shape bags. Hence, while the breakup mechanism remains the same as in the $h_l \neq f(t, z)$ case, the aforementioned fact results in a less violent main bag breakup event. The amount of generated droplets is substantially lower, and the resulting cone-like injection zone is narrower in the $h_l = f(t, z)$ case than in the $h_l \neq f(t, z)$ case. Also, the shaped ligaments tend to be thicker, thus resulting in larger droplets from ligament breakup. In short, even though there are still main breakup events, the atomization is inhibited to a certain extent, but seems more continuous in time.

3.2 Quantitative analysis

3.2.1 Ligaments analysis

Ligaments are characterized in 2D through the liquid volume fraction α projection in the XZ plane and the identification of individual elongated structures, as detailed in Section 2.2.3.4. The histogram of ligament lengths is shown in Figure 3.2 for both simulated cases and both experimental and DNS data from the literature.

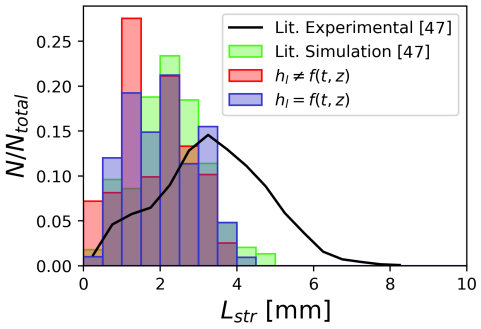

Figure 3.2: Ligament 2D length distribution for both simulated test cases (Method 1 used for ligament length measurement). Literature DNS and literature experiments are also reported [47].

First, it must be mentioned that both ligament size distributions obtained by the DNS simulations presented in this investigation importantly differ from the experimental data reported in the literature. However, Warncke et al. [47] already justified that the experiment occasionally reports several ligament lengths beyond the DNS domain ($L_{str} > 5\,\text{mm}$), with a wide time window (i.e. a long amount of breakup events) being analyzed. In the simulations, no structure attached to the intact core was found to trespass the domain outlet, with maximum lengths around $L_{str} = 4\,\text{mm}$. Reliably predicting the maximum ligament length for the operating condition studied would then imply enlarging the DNS domain and analyzing a greater amount of breakup events. Both actions are beyond the current affordable computational resources for a DNS study. In any case, the comparison of both $h_l \neq f(t,z)$ and $h_l = f(t,z)$ cases with the literature DNS (which uses the same domain length as the one used in the present study) shows fairly similar distributions, with ligament lengths spanning from 0 to 4.5 mm and most values being found among 1.5 and 2.5 mm. An improvement in the predictions is found in the $h_l = f(t,z)$

case with respect to the $h_l \neq f(t,z)$ case, as the distribution as a whole and its mode are shifted towards longer lengths when the liquid film thickness evolution is accounted for at the DNS inlet. Besides, the distribution more closely resembles a normal distribution, as it was found for the experiments. The irregular shape from the distribution can be attributed to the fact that only 3 breakup events could be simulated.

Before analyzing the results found through the 3D post-processing strategy, it is interesting to assess the differences among Method 1 (axial distance method) and Method 2 (Fast Marching Method) for ligament length determination, since 3D sizes can only be determined through Method 2. Figure 3.3 shows this comparison for the $h_l \neq f(t,z)$ and $h_l = f(t,z)$ cases. In both cases, the distributions found through both methods are relatively similar. Ligament sizes predicted through Method 2 are statistically slightly displaced towards larger values, as expected considering that the whole ligament path is computed as opposed to only accounting for streamwise variations in the ligament tip location. Anyway, this method displays its potential for the 3D ligament detection case, for which it is strictly needed.

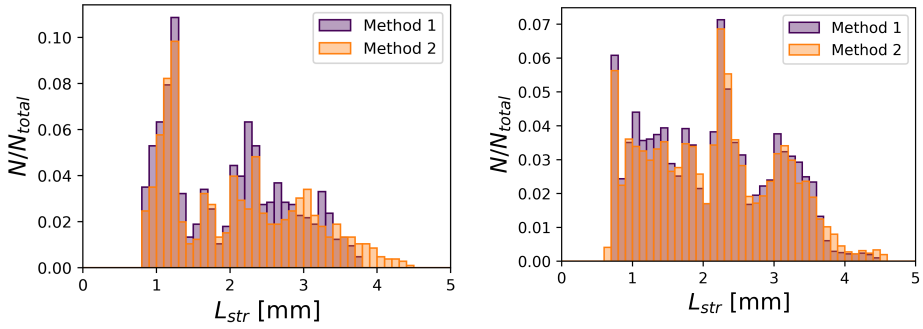

Figure 3.3: Comparison among the ligament 2D length distributions found for Methods 1 and 2 for the $h_l \neq f(t,z)$ case (left) and $h_l = f(t,z)$ case (right).

Once the differences among ligament length determination methods have been assessed, Figure 3.4 depicts the results obtained in the ligament 3D lengths between simulated test cases. Focusing on one of the simulated test cases separately, a certain shift towards greater ligament lengths is observed compared to the analogous 2D distributions obtained with Method 2 from Figure 3.3, as logical. Except for the shortest ligaments (hardly distinguishable from the intact film), the $h_l \neq f(t,z)$ case more closely resembles a normal

distribution. Despite the comparison in 2D (Figure 3.2) showing longer ligament lengths for the $h_l = f(t,z)$ case, the 3D ligament length distribution found for the $h_l \neq f(t,z)$ case is more shifted towards greater values. Hence, these differences must be attributed to the more acute flapping observed when liquid accumulation behind the prefilmer edge is synchronized along the span, as commented in the view of Figure 3.1. This fact highlights that any ligament length comparisons with experimental data are not fully representative unless flapping is also taken into account.

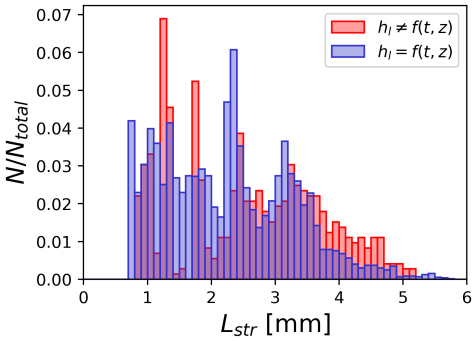

Figure 3.4: Ligament 3D length distributions found for both simulated cases (Method 2 used for ligament length measurement).

As far as ligament tip velocities $\mathbf{u_{str}}$ are concerned, the distributions obtained for each of the three components in each simulated case are shown in Figure 3.5. Important differences are found in all cases. Focusing on the streamwise velocity component, the distribution for the $h_l \neq f(t,z)$ case is significantly shifted towards higher values (the distribution is centered around $u/u_g = 0.12$) than the distribution for the $h_l = f(t,z)$ case (most ligaments found in the $u/u_g = 0$ to 0.1 range). This may be explained considering the locations at which it is more probable to find a ligament tip in each simulated case, shown in Figure 3.6. In the $h_l \neq f(t,z)$ case, the liquid film flaps more importantly about the prefilmer center line (recall also Figure 3.1). Thus, in this case the ligaments extend towards more external wall-normal locations, where the influence from the liquid and gas-liquid boundary layers is less severe. At these locations the gaseous phase travels faster, leading to a greater momentum exchange with the liquid film and the resulting ligaments, increasing their streamwise velocities. The locations at which the ligament tips are found also explain the different distributions obtained in Figure 3.5 for the wall-normal ligament tip velocity components: the $h_l = f(t,z)$ case resembles a normal distribution centered about $v/u_g = 0$, as the ligament tips

are equally found around the prefilmer center line in Figure 3.6. However, the $h_l \neq f(t,z)$ case yields a bimodal distribution, one of the modes being centered around a value $v/u_g \geq 0$. This mode corresponds to the fact that, in this case, the ligament tips are preferentially found above the prefilmer edge (see Figure 3.6) or close to its center (please note that this result might be biased by the fact that only 3 breakup events could be simulated, potentially not resulting in a statistically representative sample in this strategy). Ligaments that extend above the prefilmer tend to move away from the prefilmer surface in the wall-normal direction as they penetrate axially, thus possessing positive wall-normal velocities. Finally, the differences among test cases in the spanwise component distributions are less severe, being centered around $w/u_g = 0$ in both cases. The deviation about this value is more acute in the $h_l \neq f(t,z)$ case, since the film disintegration into ligaments is more violent in this simulation.

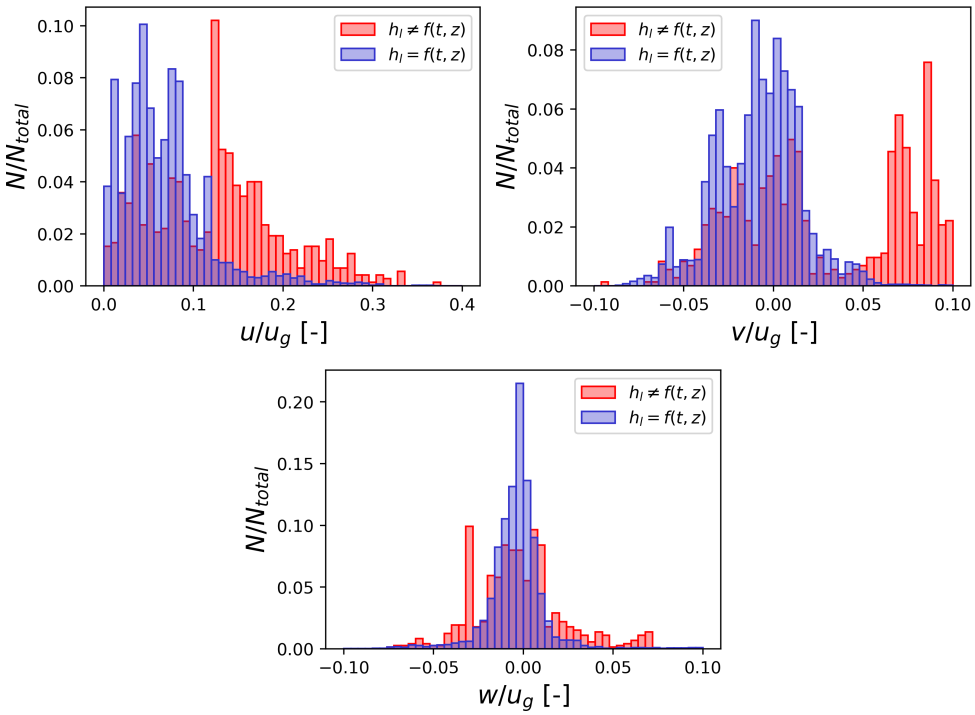

Figure 3.5: Distributions of 3D ligament tip velocity components for both simulated test cases: streamwise velocity (top left), wall-normal velocity (top right), spanwise velocity (bottom). All values are normalized with the gas bulk velocity.

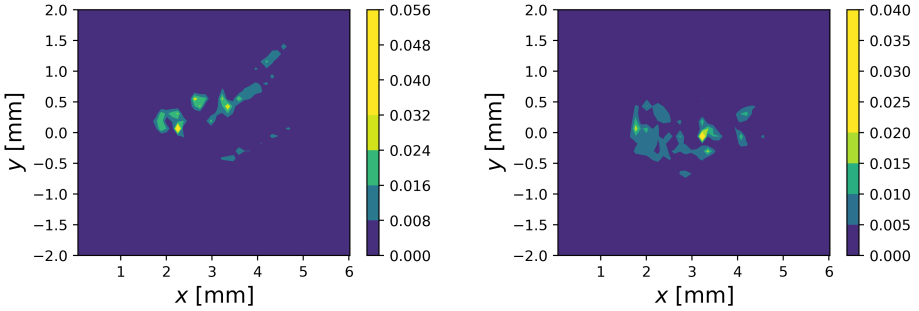

Figure 3.6: Contours displaying the probability of finding a ligament tip in the different locations of the XY plane: $h_l \neq f(t,z)$ case (left) and $h_l = f(t,z)$ case (right).

Figure 3.7 depicts the histogram of ligament equivalent diameters d_{eq} for both simulated cases. For each distribution, there are several peaks or clusters of ligaments with similar equivalent diameter. Hence, it may be expected that the sizes of the droplets generated from ligament breakup are related to these values. However, since the ligament equivalent diameter embeds the evolution of the ligament diameter along its length, the quantitative values cannot be directly comparable to drop size diameter values (droplets generated by ligament breakup are strictly generated at the ligament tip). Anyway, the qualitative comparison among simulation methodologies is insightful, as a strong influence of the simulated test case is observed on the processed data. In the $h_l \neq f(t,z)$ case, equivalent diameters are shifted towards significantly lower values than their $h_l = f(t,z)$ counterpart. It may then be expected for the droplets generated from ligament breakup in the $h_l \neq f(t,z)$ case to have statistically lower sizes than the droplets generated from ligament breakup in the $h_l = f(t,z)$ case. A closer look at this phenomenon will be given in the analysis of the droplet cloud generated in each simulation.

Finally, characteristic quantities from the ligament analysis are displayed in Table 3.2. As expected according to the view of the size PDFs, the mean breakup length L_{bu} is sensibly underpredicted in all cases, but it reaches values similar to the literature DNS [47, 59] with the $h_l = f(t,z)$ case being slightly closer, specially in the 2D analysis. The values extracted through the 3D analysis are higher for both cases, but the increase is more noticeable in the $h_l \neq f(t,z)$ case due to the larger extension of the ligaments found in the wall-normal direction. The film deformation velocity u_{def} and mean breakup frequency f_{bu} values are underpredicted in the $h_l \neq f(t,z)$ case while the $h_l = f(t,z)$ case overpredicts them. Furthermore, the 3D analysis yields

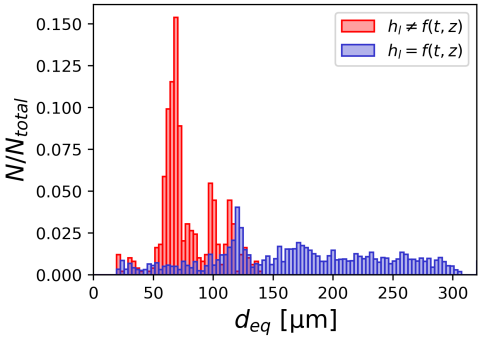

Figure 3.7: Ligament equivalent diameter distributions found for both simulated test cases (Method 2 used for ligament length measurement, only 3D data considered).

lower values than the 2D analysis for both parameters. In terms of u_{def}, the $h_l = f(t,z)$ case shows again a better agreement with the experiments. All in all, it is observed that mean values may not be representative of the agreement in the related distributions.

Table 3.2: Characteristic quantities obtained from the ligament 2D and 3D analysis for both simulations and size post-processing methods. Literature DNS and literature experimental data from [47] are also provided. Note: the u_{lig} value of the literature experimental data was found for $\dot{V}/b = 25$ mm^2/s.

Source	L_{bu} [mm]	u_{lig} [m/s]	u_{def} [m/s]	f_{bu} [kHz]
Lit. Exp. 2D [14]	3.2	5.00	-	4.91
Lit. DNS 2D [47]	2.2	-	8.2	3.73
$h_l \neq f(t,z)$ 2D	2.0	5.79	6.53	3.27
$h_l = f(t,z)$ 2D	2.1	6.2	11.97	5.70
$h_l \neq f(t,z)$ 3D	2.56	6.87	6.28	2.45
$h_l = f(t,z)$ 3D	2.25	3.50	11.51	5.12

3.2.2 Droplets analysis

The post-processing technique described in Section 2.2.3.4 allowed detecting distinct droplets in both simulated cases. The temporal evolution of the number of detected droplets in each simulation is shown in Figure 3.8, where the initial transient has been omitted and results are normalized with the mean amount of droplets detected in the depicted interval. These values are

406 droplets/frame in the $h_l \neq f(t,z)$ case and 62 droplets/frame in the $h_l = f(t,z)$ case. This large variation could be appreciated from the flow evolution depicted in Figure 3.1. While other literature works using VOF on the test case did not specifically report this quantity, their qualitative comparisons among experimental and computational snapshots also showed a clear overprediction of the amount of droplets computationally predicted (especially noticeable in the side views, considering the actual prefilmer span b is an order of magnitude greater than the simulated span) [47, 59]. This fact is aligned with the finding of the present investigation, in the sense that accounting for the liquid film evolution upstream of the prefilmer edge results in a less violent breakup and a substantially lower amount of generated droplets.

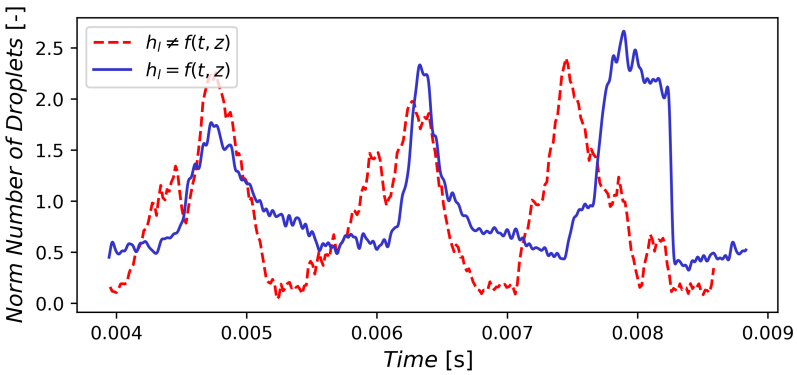

Figure 3.8: Temporal evolution of the number of detected droplets for both simulated cases. Results are normalized with the mean number of droplets detected in the time series in each case: 406 droplets for the $h_l \neq f(t,z)$, 62 droplets for the $h_l = f(t,z)$ case.

Coming back to Figure 3.8, it is possible to distinguish three main breakup events where the number of droplets suddenly increases, substantially rising above the average. These instants correspond to the stages of *bag breakup* illustrated in Figure 3.1. After a main breakup event, the number of generated droplets decreases as only ligament breakup is present while liquid is being accumulated in the reservoir behind the prefilmer edge prior to a new bag breakup event. Important differences are observed among the simulated cases. In the $h_l \neq f(t,z)$ case, the amount of generated droplets after a main event decays practically down to zero, importantly inhibiting atomization. In the $h_l = f(t,z)$ case, however, the amount of generated droplets only gets down to half of the average amount. This implies that ligament breakup is more

relevant in this case and atomization is more continuous. As discussed in the view of Figure 3.8, the fact that temporal and spanwise variations in the film thickness are included at the DNS inlet results in film waves reaching the liquid reservoir behind the perfilmer edge in a non-synchronized manner. Hence, the film reservoir is not uniform spanwise and bags are not generated along the whole span by the time some of them break. This yields a less violent main bag breakup event and a greater relative importance of the ligament breakup, as the resulting ligaments are also shaped by the remaining reservoir prior to the formation of new bags.

Additionally, the frequency among main events also differs for both simulations. A value of $f_{main} = 656.2\,\text{Hz}$ is observed for the $h_l \neq f(t,z)$ case, whereas $f_{main} = 630.0\,\text{Hz}$ is found for the $h_l = f(t,z)$ case. Even though both values are similar to the reported $\overline{f_{film}} = 585.9\,\text{Hz}$ from the 2-phase flow precursor LES (recall Table 2.2), the $h_l = f(t,z)$ case is closer, despite not accounting for the effect of the interfacial instability on the complete prefilming surface. Holz et al. [62] already reported a direct relation among film wave frequency and breakup frequency, but justifying the minor differences through the slight decoupling by the accumulation of liquid at the trailing edge. This also justifies the differences observed in the present study among film wave frequency and breakup frequency. Even though the decoupling is present, not the same breakup frequency is retrieved if the film wave behavior is not introduced to the DNS. While this decoupling among frequencies is observed for this operating condition with $M = 15.7$, it must be noted that operating conditions with higher momentum flux ratios [26] or with a lower ratio among film thickness and prefilmer thickness [34] (as is the case of commonly used aero engines) are expected to become dominated by the film evolution rather than by liquid accumulation. In such cases, the presented results highlight the importance of accounting for the liquid film evolution upstream of the prefilmer edge, either through the inlet boundary condition proposed in the study (one-way coupling among domains), or by means of a larger computational domain for two-way coupling hardly affordable currently.

As far as the droplet sizes are concerned, Figure 3.9 shows the drop diameter PDFs for both simulated cases compared against experimental data. As mentioned in Section 2.2.3.4, it is important to note that droplets exhibiting a diameter $d_V \leq 20\,\mu\text{m}$ have been discarded from the analysis, also corresponding to the resolution limit of the experimental data [47]. The comparison highlights that a substantially fairer agreement with experimental data is achieved when accounting for the liquid film history in the $h_l = f(t,z)$ case. This result may be justified in the view of the ligament equivalent diameter (d_{eq}) distributions (Figure 3.7): droplets generated from ligament

breakup in the $h_l \neq f(t,z)$ case have statistically lower sizes (comparable to the ones generated from bag breakup) than the droplets generated from ligament breakup in the $h_l = f(t,z)$ case (which are significantly larger than the ones generated from bag breakup). This explains why the drop size PDF of the $h_l \neq f(t,z)$ case seems to have a single mode, as the ligament breakup mechanism is obscured by the large amount of droplets produced at the bag burst stage. The drop size PDF of the $h_l = f(t,z)$ case, in turn, recovers a multi-modal distribution, since the droplets generated from ligament breakup are substantially larger than the ones generated from bag breakup. The fact that the multi-modal distribution is recovered when accounting for the liquid film thickness evolution upstream of the prefilmer edge implies that this simulation correctly balanced the relative importance among *bag breakup* and *ligament breakup*, better resembling the experimental results despite showing a slight underprediction of the size values of the peaks in the first two modes.

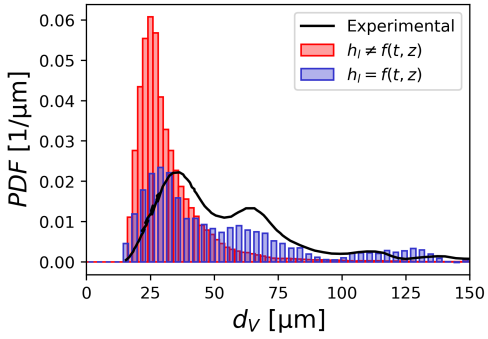

Figure 3.9: Droplet size Probability Density Function (PDF) for both simulations and experimental data from Warncke et al. [47].

Figure 3.10 shows the PDFs obtained for each of the droplet velocity components, including a comparison with experimental data from [47] in the case of the streamwise component. Despite the differences in the number of predicted droplets and their size PDFs, the distributions are relatively similar among simulated cases. In the case of the streamwise velocity component, both predicted PDFs resemble a normal distribution. The agreement with experimental data seems slightly better in the $h_l = f(t,z)$ case, although values are underpredicted for a relevant amount of droplets. The distribution shape and dispersion about the average is similar for both simulated cases, but the distribution is shifted towards larger velocities in the $h_l \neq f(t,z)$ case. This fact is reasonable considering that a larger proportion of small droplets (subject to less aerodynamic drag when interacting with the gaseous phase) was

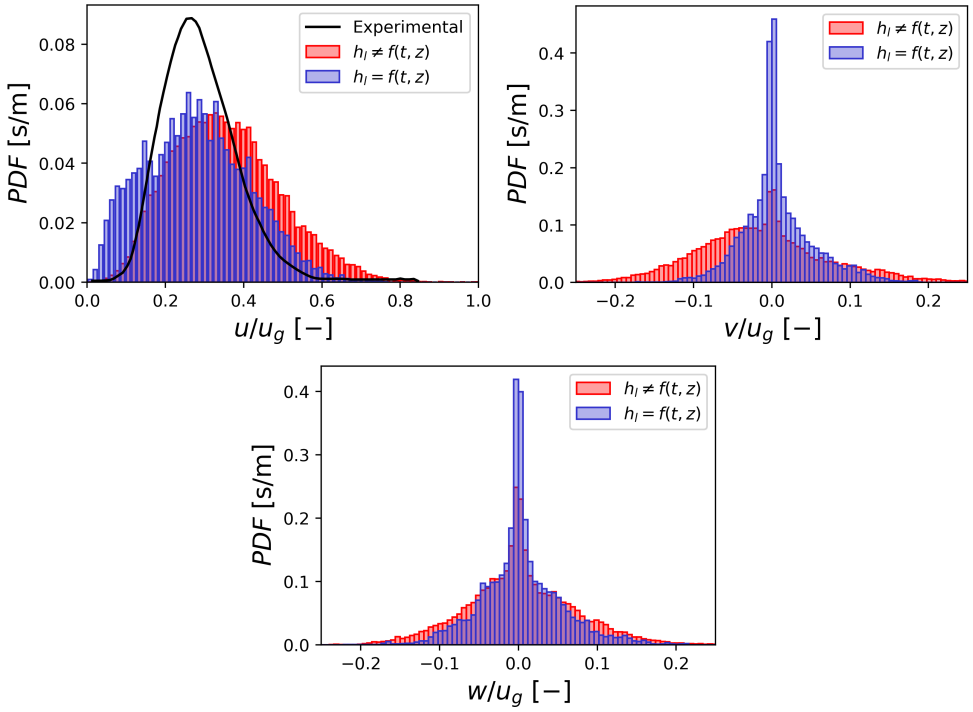

Figure 3.10: PDFs for the droplet velocity components for both simulated test cases: streamwise velocity (top left, including also experimental data from Warncke et al. [47]), wall-normal velocity (top right), spanwise velocity (bottom). All values are normalized with the gas bulk velocity.

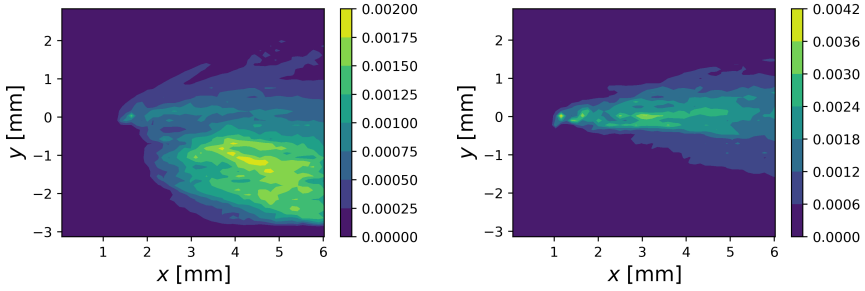

Figure 3.11: Contours displaying the probability of finding a droplet in the different locations of the XY plane: $h_l \neq f(t,z)$ case (left) and $h_l = f(t,z)$ case (right).

found, and results in a substantial overprediction compared to experimental data. As far as the wall-normal velocities are concerned, the PDF is centered around 0 for the $h_l = f(t,z)$ case, exhibiting low dispersion. Nevertheless, the $h_l \neq f(t,z)$ case predicts a noticeably higher dispersion and its average is displaced towards negative values. As it happened for the ligament tips, this may be explained considering the locations at which it is more probable to find a droplet in each simulated case, as shown in Figure 3.11. As already explained in the view of Figure 3.1, in the $h_l \neq f(t,z)$ case the liquid film flaps more importantly about the prefilmer center line, resulting in a wider spray angle. Figure 3.11 also highlights that droplets in the $h_l \neq f(t,z)$ case are preferentially found below the prefilmer center line, whereas they are quite uniformly distributed on both sides of the prefilmer in the $h_l = f(t,z)$ case. It is important to recall that, in the former case, ligaments were preferentially found above the prefilmer, as shown in Section 3.2.1. Figure 3.1 showed a situation for this case for which ligaments indeed extended above the prefilmer. Such ligaments were generated from a film flapping motion whose bags got punctured towards the opposite side of the prefilmer, yielding a substantially higher amount of droplets below the prefilmer center line. Droplets generated below the prefilmer through this mechanism tend to travel further away from the prefilmer center line, reaching negative wall-normal velocities as reflected in Figure 3.10. In any case, it must be again noted that this shift towards negative wall-normal velocities may be biased by the fact that only 3 breakup events could be simulated. Results for the $h_l = f(t,z)$ case seem more statistically representative as the film accumulation behind the prefilmer edge is desynchronized spanwise, providing bag breakup both above and below the prefilmer center line and resulting in a spray more uniformly spread in the wall-normal direction. Finally, the differences among simulated cases in the spanwise component distributions are not so relevant, being centered around $w/u_g = 0$ in both cases and slightly more deviated about this value in the $h_l \neq f(t,z)$ case.

It is interesting to analyze the correlation among droplet size and droplet velocity. Figure 3.12 (left) shows the scattered information (focused on streamwise velocity) for all the detected droplets in both simulated cases. Results show that in both simulated cases large droplets statistically possess a lower streamwise velocity. Additionally, the dispersion in the velocity PDF is greater the lower the drop size, as confirmed in the view of Figure 3.12 (right) where it is seen that the mean velocities are noticeably shifter towards high values as the droplet size decreases. These trends follow a non-linear fashion. As already implied by Figure 3.10, the comparison among test cases highlights

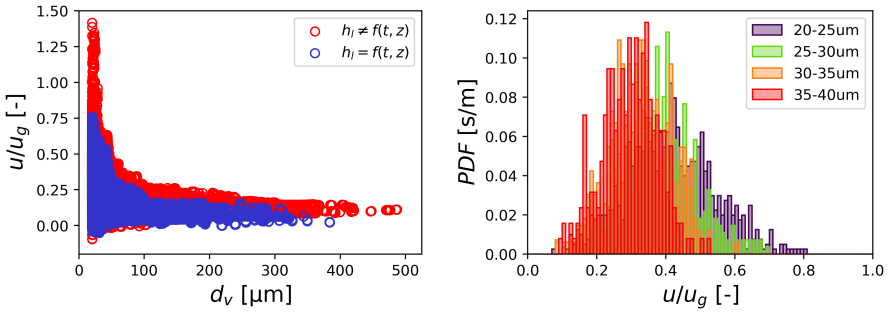

Figure 3.12: Scatter plot for the streamwise droplet velocity as a function of the drop diameter for both simulated cases (left), and detail on the streamwise droplet velocity PDFs corresponding to different drop size classes in the $h_l \neq f(t,z)$ case (right).

the greater velocities achieved by the droplet cloud in the $h_l \neq f(t,z)$ case compared to the $h_l = f(t,z)$ case.

3.3 Conclusions

In this Chapter, results for an operating condition widely studied in the literature were discussed comparing two DNS simulations with different inflow conditions: a DNS that only accounted for a constant (timewise and spanwise) liquid film thickness at the domain inlet on the one hand; and the DNS that took advantage of the full proposed methodology by accounting for the oscillations in the liquid film thickness at the domain inlet on the other hand. The inflow condition of both simulations accounted for gas turbulence.

Qualitative comparisons among the primary breakup simulations showed important differences among simulation strategies. Even though the predicted breakup mechanism sequence was the same in accordance with the momentum flux ratio of the chosen operating condition (liquid accumulation behind the prefilmer edge followed by bag formation, bag breakup, ligament formation and ligament breakup), the resulting ligament distribution and droplet cloud were fairly different. Accounting for the liquid film evolution upstream of the prefilmer edge resulted in the liquid reservoir formed behind its edge being less uniformly distributed spanwise than it was for the constant liquid film thickness case, as the film crests and valleys do not reach the reservoir in a synchronized manner along the prefilmer span. This eventully results in a less violent main bag breakup event when the film evolution upstream of

the prefilmer edge is accounted for, inhibiting atomization to a certain extent but producing breakup more continuously in time than for the constant liquid film thickness case. Even though both simulation strategies lead to a substantially greater amount of droplets being generated by bag breakup than by ligament breakup, the latter mechanism gains relative importance when accounting for the liquid film evolution upstream of the prefilmer edge. Additionally, ligaments predicted through this methodology have a statistically larger equivalent diameter than the ones predicted when the film evolution is not considered. This allowed the prediction of a clearly multimodal drop size distribution in this case.

DNS ligament and droplet cloud processed data were quantitatively validated against experimental results available in the literature. A reasonable agreement was found in both simulated cases, with a noticeable improvement in the predictions when accounting for the liquid film evolution upstream of the prefilmer edge, despite not accounting for the absolute nature of the interfacial instability produced at this location. The multi-modal feature of the droplet size distribution exhibited by the experiments could only be retrieved when making use of the proposed methodology, as explained above. The observed differences in the velocity distributions, splitted among velocity components, could be explained by the fact that the spray was differently spread in the wall-normal direction in both cases. Accounting for the liquid film evolution along the prefilmer surface resulted in a uniformly spread spray within a relatively narrow cone. However, the constant liquid film thickness case resulted in a wider spray due to the greater importance achieved by film flapping in this case. In this simulation, the film behaves similarly at all spanwise locations for a given breakup event, meaning that all the shaped bags get punctured and breakup at the same stage of flapping, generating all droplets at the same side of the prefilmer, thereby also conditioning their velocities. In any case, the averaged and aggregated quantities considered in the analysis of the constant liquid film thickness case might be biased by the fact that only a few distinct breakup events were simulated and not accounting for a wide range of variability of breakup events. This limitation is in fact attenuated if the liquid film evolution along the prefilmer surface is accounted for.

Additionally to the commented shortcoming concerning the realizable simulated time, other limitations of the methodology must be highlighted. The large amount of resources required for the calculations implied only a small computational domain could be considered. This fact hindered the characterization of the ligament formation stage, as the experiments reported longer ligaments than the ones possibly found in the simulations. Nevertheless, this

limitation is acknowledged in most literature works achieving a similar resolution than the one here presented. Precisely the mesh resolution is another limitation. Even though a proper turbulence reproduction was ensured by comparison with the Kolmogorov length scale, achieving lower cell sizes would have resulted in a better description of the liquid-gas interface, as a large amount of droplets was found to have diameters in the order of twice the cell size. Moreover, the artificial instability triggered by the prefilmer edge is of absolute nature, implying said instability is also transmitted upstream of the generating source. This phenomenon is not fully accounted for in the proposed methodology, which splits the geometry in different computational domains assuming one-way coupling among them. The upstream effect of this instability is thus only accounted for in the limited part of the DNS domain covering the prefilming surface.

Finally, it must be noted that the study is restricted to a given operating condition corresponding to the *torn-sheet breakup* regime, for which liquid accumulation behind the prefilmer edge is significant and the breakup frequency is partially decoupled from the film wave frequency. Conditions with a higher gas-to-liquid momentum flux ratio, realizable in aero engines, lead to the so-called *membrane-sheet breakup*, where the accumulation mechanism loses importance in favor of a direct disintegration in ligaments and droplets behind the prefilmer edge. In such circumstances the breakup frequency is expected to be more closely coupled to the film wave frequency. This should result in a more realistic description and more accurate predictions being obtained by the methodology proposed in the present Chapter.

Chapter 4

Study of the influence of flow properties on the primary atomization process

In this Chapter, the eDNS concept described in Section 2.2 to account for gas inflow turbulence with a constant liquid film thickness at the inlet is used to perform a parametric study on the primary breakup process. The choice to employ this approach instead of the novel approach proposed in Chapter 2 (whose results are analyzed in Chapter 3) with variable film thickness stems from the fact that some of the operating conditions to be studied induce an exceptionally thin film at some particular instants and local positions along the prefilmer span corresponding to the DNS inlet. Under these circumstances, using the mesh resolution described in Section 2.2.3.2, the low number of cells locally describing the film at some instants induced unexpected dewetting phenomena, contradicting the behaviour based on experimental observations. This fact is attributed to a local lack of resolution in this region during some time steps. Consequently, achieving a more refined simulation was imperative, but unfortunately, as discussed in Section 2.2.3.2, further refinement was not feasible within the scope of this thesis.

Four simulations were conducted analysing the effect of both the gas velocity and the liquid properties (and their related relevant non-dimensional groups) on the atomization phenomena. At least two atomization events were simulated, as the first one was considered transient and was excluded from the

Table 4.1: Unchanged parameters in the parametric study.

Description	Parameter	Value	Units
Temperature	T	298	K
Pressure	P	1	atm
Gas density	ρ_g	1.21	kg/m^3
Gas dynamic viscosity	μ_g	1.82×10^{-5}	Pa s
Liquid normalized volumetric flow rate	$\dot{V}/b$	50	mm^2/s
Liquid velocity	$\bar{u_l}$	0.5	m/s

Table 4.2: Variable parameters of the operating conditions. Descriptions of every parameter are not included for means of readability, but they were reported in Table 2.1. Mean film height values $\bar{h_l}$ were rounded to the value shown under parentheses to fit the coarsest mesh cell size.

Parameter	OP#1	OP#2	OP#3	OP#4	Units
Label	D70_Ug50	D70_Ug70	H20_Ug50	H20_Ug70	-
$\bar{u_g}$	50	70	50	70	m/s
Fuel	Shellsol D70		H_2O-Propanediol		-
ρ_l	770		1008		kg/m^3
μ_l	0.00156		0.00606		Pa s
σ	0.0275		0.0466		kg/s^2
$\bar{h_l}$	74.3 (80)	62.5 (60)	104.5 (100)	86.4 (80)	µm
Re_g	13480	18870	13480	18870	-
Re_l	24.63	24.63	8.32	8.32	-
We_l	8.62	12.75	6.36	10.03	-
We_h	25.3	49.6	14.93	29.26	-
We_δ	151.48	282.97	89.39	166.99	-
Oh	0.0224	0.0224	0.0583	0.0583	-
M	15.71	30.8	12	23.53	-

analysis. It is worth noting that, while simulating a larger number of events would allow for a more statistically robust analysis, nowadays it is unfeasible to do it through DNS for every operating condition. The dimensions of the domain in these simulations were presented in Table 2.3. The parameters that remain unchanged in the parametric study are summarized in Table 4.1 while the ones that change for each operating condition are shown in Table 4.2.

A qualitative analysis is carried out in Section 4.1, describing the atomization mechanism and comparing the appearance between cases. Then, a quantitative analysis of the ligament development and the generated droplet

cloud is conducted in Section 4.2. Finally, Section 4.3 summarizes the main findings of this study.

4.1 Qualitative analysis

Figure 4.1 shows a time sequence of one major breakup event for all the operating conditions tested. Results show in all cases the expected breakup mechanism and phenomenology for prefilming airblast atomizers described in Section 1.2. An atomization event starts with liquid accumulation behind the prefilmer edge. Once enough liquid is accumulated, it shapes the so-called bags, which break up leading to fine droplets. At the same time, from bag breakup, rims and ligaments are formed. As explained in Section 3.2.2 using the reference condition, ligament breakup generates larger droplets compared to those generated by bag breakup.

While all the operating conditions show the aforementioned breakup mechanism, it may be seen that OP#1 and OP#3 present more liquid accumulation behind the prefilmer edge prior to a major breakup event. Thus, the film importantly flaps before a violent breakup occurs due to puncturing of the flapping film. This violent breakup results in the droplets not being uniformly produced in the wall-normal direction. In OP#2 and OP#4, however, breakup starts with less liquid accumulation behind the prefilmer edge. In these cases, the film does not flap so violently prior to breakup, resulting in a more uniform spray cone and a scattering of the droplets. This is especially noticeable in OP#2, with OP#4 appearance still exhibiting some flapping. Later in the atomization process, they consistently display a greater quantity of ligaments, albeit small in size, distributed more evenly along the Z-axis of the domain. Furthermore, increased film wrinkling is exhibited at the end, attributed to the higher Re_g and We_l values. These observations may also be justified through the momentum flux ratio M as explained in Section 1.2. Reminding the macroscopic behaviours of the Figure 1.3 and the threshold values from Chaussonnet [15], OP#1 and OP#3 correspond to M values between 4 and 20 (15.71 and 12 respectively) closer to the *torn-sheet breakup* regime, while OP#2 and OP#4 have M values higher than 20 (30.8 and 23.53 respectively) being related to the *membrane-sheet breakup* regime.

On the other hand, OP#2 led to the finest atomization, due to the combined effect of achieving a greater gas velocity and reducing the liquid density, viscosity and surface tension (i.e. the combination of high Re_g and high We_l numbers). As a result, this condition exhibits the highest number and the smallest size of the droplets. Conversely, the operating condition exhibiting a

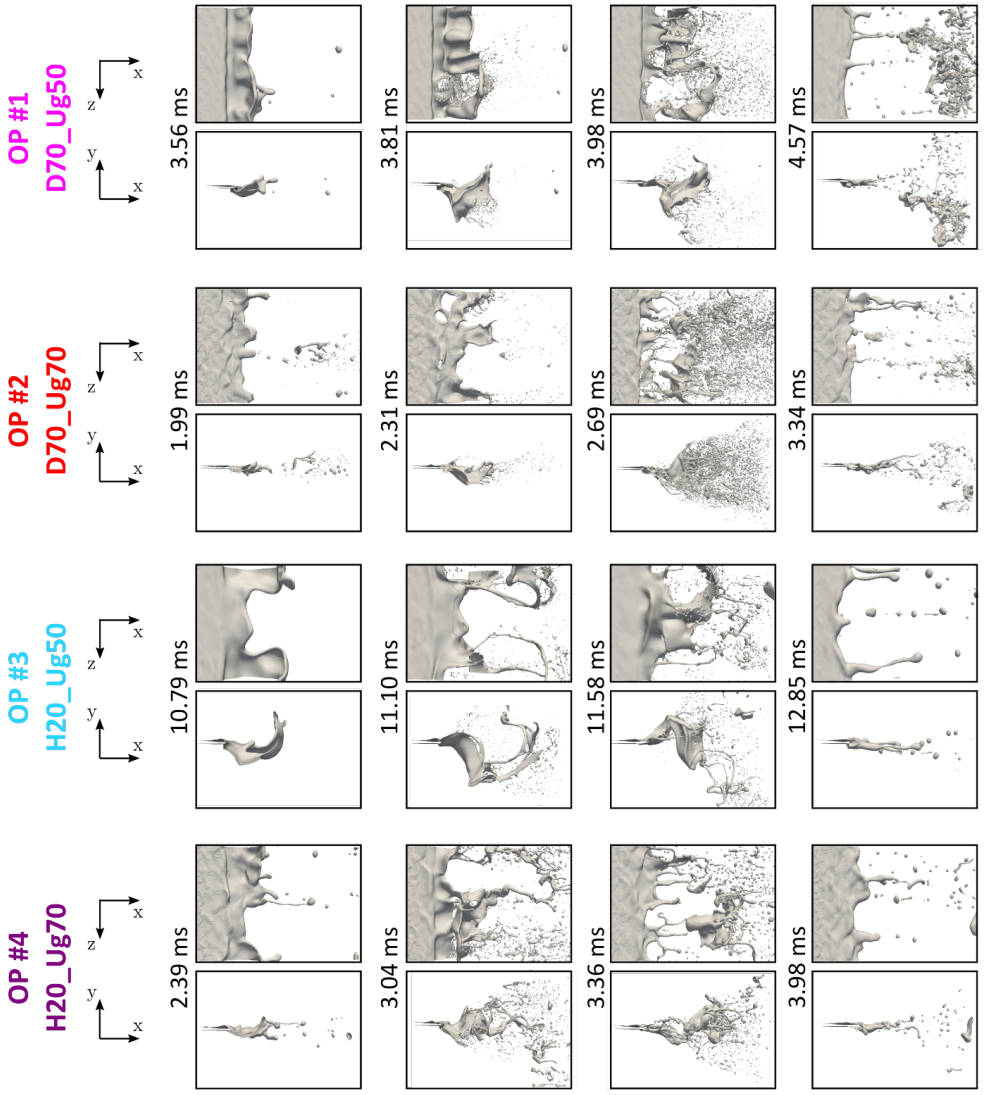

Figure 4.1: Time sequence of the DNS results for the operating conditions tested. Liquid film and structures are depicted through an iso-surface of $\alpha = 0.5$. *For each condition, the upper row represents a top view, whereas the lower row represents a side view.*

poorer atomization is OP#3, as expected also in the view of the gas velocity and liquid properties (i.e. the combination of low Re_g and low We_l numbers). This condition exhibits the thickest and longest ligaments at the end of the atomization process, resulting in larger droplets compared to all other cases as evidenced by its lower values of Weber numbers (We_l, We_h and We_δ) and momentum flux ratio M. In between, OP#1 seems to exhibit a finer atomization than OP#4 despite its lower Re_g and We_l number, which could be explained by the different atomization regime induced by M in both cases, as the film flapping is more violent in OP#1. The quantitative analysis and statistical treatment of the data should confirm this explanation.

4.2 Quantitative analysis

Different post-processing tools have been implemented and applied to the DNS data to generate and analyse quantitative results. These tools, reported in Section 2.2.3.4, allowed independently analysing the intact core with ligaments and the separated droplet cloud for all the tested operating conditions.

4.2.1 Ligaments analysis

The parameters extracted from the 3D ligament analysis are global breakup length L_{bu} and mean ligament tip velocity u_{lig}. The mean breakup frequency f_{bu} value is calculated from Equation 2.33, requiring mean film deformation speed u_{def} (please note that these values differ from [118] because u_{def} was obtained there after the ligaments were removed from the intact core as in Figure 2.15 Step 3). The length at which 90% of the ligaments break up L_{90} is computed from the 2D treatment, as it will be used in Chapter 5 for the breakup model. All these results are reported together in Table 4.3 for every operating condition.

Table 4.3: 3D ligament post-processing main results.

Parameter	OP#1	OP#2	OP#3	OP#4	Units
L_{bu}	2.56	1.87	3.75	2.50	mm
u_{lig}	6.87	6.38	6.27	6.29	m/s
u_{def}	7.11	8.34	11.16	8.89	m/s
f_{bu}	2.78	4.46	2.98	3.56	kHz
f_{main}	630.0	724.6	414.1	632.9	Hz
L_{90}	3.25	2.76	5.50	3.72	mm

An examination of the ligament properties across all operating conditions reveals minimal differences between u_{lig} values. In terms of breakup length, both L_{bu} and L_{90} follow a consistent trend: OP#2 exhibits the lowest values, OP#3 the highest, while OP#1 and OP#4 share closely intermediate values. This order matches closely with the one revealed in previous Section 4.1, in which the level of atomization achieved ranges from finest to most inhibited. Considering f_{main} values, they follow the opposite trend as expected. In terms of u_{def}, their values display uniformity among OP#2 and OP#4, corresponding to the *membrane-sheet breakup* regime. For OP#1 and OP#3, corresponding to the *torn-sheet breakup* regime, values are also close enough, but somewhat altered by the film flapping in the atomization events processed. Taking into account Warncke's results [47] for OP#1 ($u_{def} = 8.2\,\mathrm{m/s}$), the value obtained in the present investigation may be underpredicted as the strong film flapping induced many negative values of $u_{def,i}$ spanwise. On the other hand, the value obtained for OP#3 may be overpredicted as there are

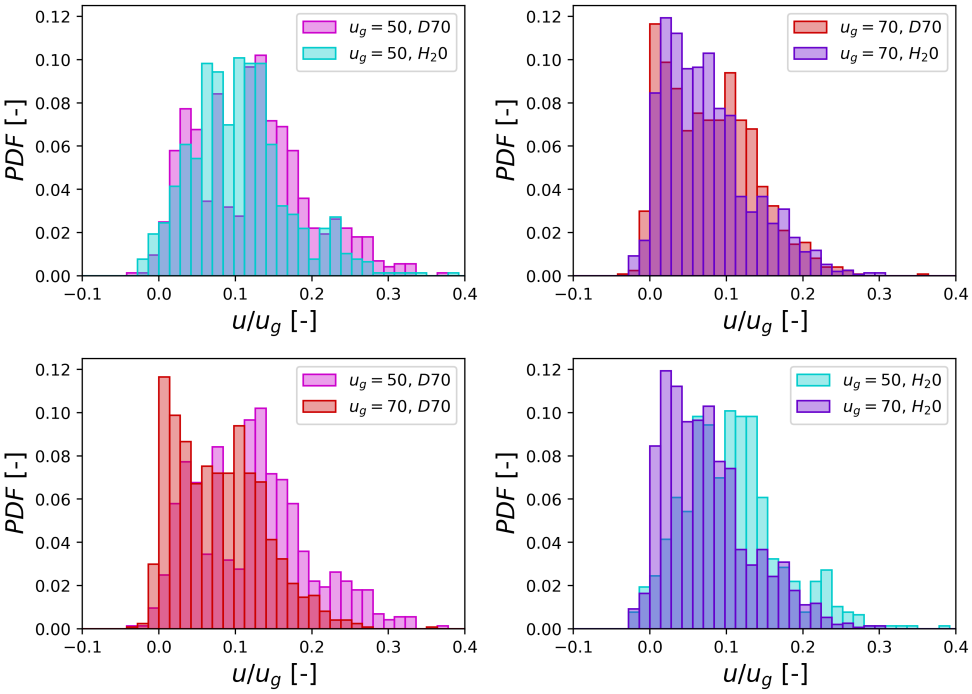

Figure 4.2: Probability density functions for the normalized streamwise velocity component of the 3D ligaments.

less negative velocity values caused by ligaments breaking off. In consequence, the trend obtained with f_{bu} values is different than the one for f_{main} values.

Next, comparisons between the probability density functions (pdf) for the streamwise, wall-normal and spanwise components of the velocity (normalized using u_g) in the tips of the ligaments after 3D postprocessing are discussed. Every figure compares cases with the same mean gas velocity but different liquids in the top part (OP#1 versus OP#3 left, OP#2 versus OP#4 right) and cases with the same liquid but different mean gas velocities in the bottom part (OP#1 versus OP#2 left, OP#3 versus OP#4 right).

Figure 4.2 corresponds to the normalized streamwise velocity component. When comparing cases with the same mean gas velocity but different liquids no big influence is observed: the liquid with higher Re_l and lower Oh (Shellsol D70) show slightly higher normalized streamwise velocities at the tip of the ligaments (also valid for absolute streamwise velocities as they were normalized using the same value). However, there is a clear difference for cases with

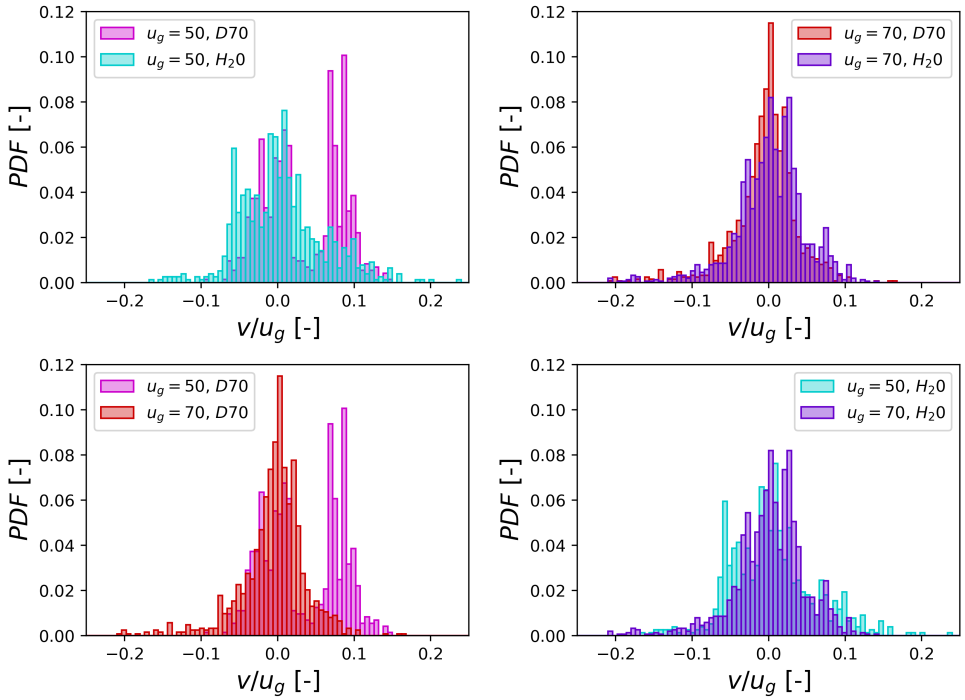

Figure 4.3: Probability density functions for the normalized wall-normal velocity component of the 3D ligaments.

the same liquid: lower mean velocities imply substantially higher normalized streamwise velocities, indicating higher momentum exchange between phases.

Figure 4.3 corresponds to the wall-normal velocity component. When comparing cases with the same lower mean gas velocity value, the liquid with higher Re_l, higher We values and lower Oh (Shellsol D70) shows a huge bias into positive wall-normal velocities at the tip of the ligaments. OP#3 is also biased towards non-zero values but in a much more subtle way. As stated before, the accumulation of the film plays a more dominant role in the breakup mechanism for operating conditions with lower M values, triggering film flapping as displayed in Figure 4.1. For cases with a higher mean gas velocity value, pdfs are centered around the null value, OP#2 being slightly more centered than OP#4. For cases with the same liquid, higher mean gas velocity tend to center the pdfs of the wall-normal velocities at the tip of the ligaments towards 0, as the film flapping effect disappears.

Figure 4.4 corresponds to the spanwise velocity component. When comparing cases with the same mean gas velocity, there is a difference between

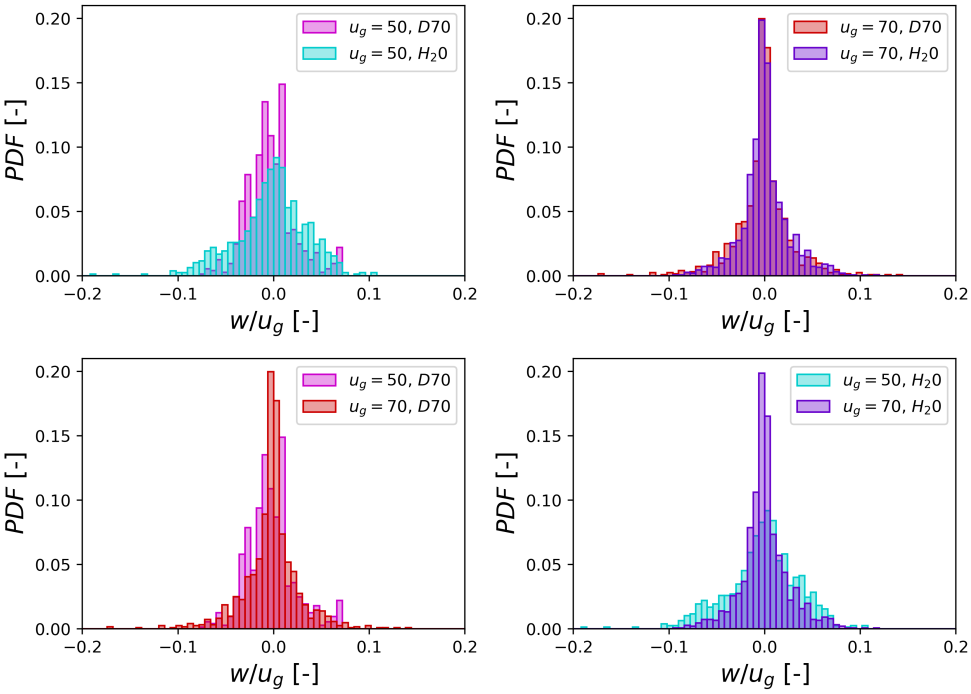

Figure 4.4: Probability density functions for the normalized spanwise velocity component of the 3D ligaments.

cases if this value is lower. Case OP#1 with higher Re_l, higher We values and lower Oh shows a more centered pdf around the 0 spanwise velocity value at the tip of the ligaments than and OP#3. Nevertheless, for a higher mean gas velocity (cases OP#2 and OP#4) these differences dissappear. For cases with the same liquid, higher mean gas velocities also tend to center the pdfs around the null value.

4.2.2 Droplets analysis

At this point, it is interesting to compare the results of the droplet cloud among the operating conditions to get a broader perspective on the behaviour of the primary breakup process. Additionally, the probability density functions obtained in this study constitute the basis for the proposed model in Chapter 5.

First, the distribution of droplets in the wall-normal direction is analysed. Figure 4.5 displays the contour of the regions in the XY plane where it is more probable to find a droplet during a given atomizing event, as it is considered more illustrative than the sole wall-normal location pdf (reproduced anyway in Figure 4.6 for illustrating purposes). The sampling of the droplets for the

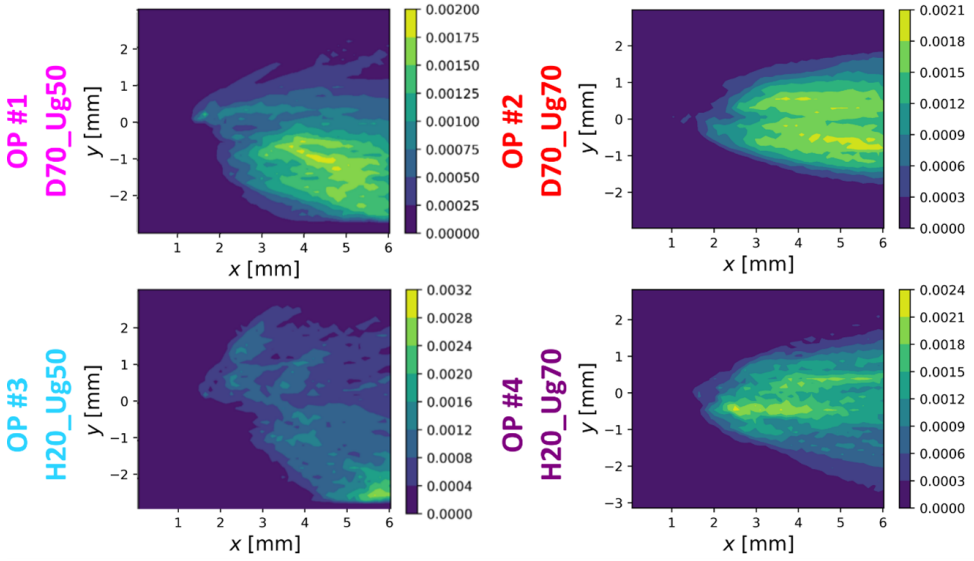

Figure 4.5: Probable droplet location contour for the different operating conditions tested.

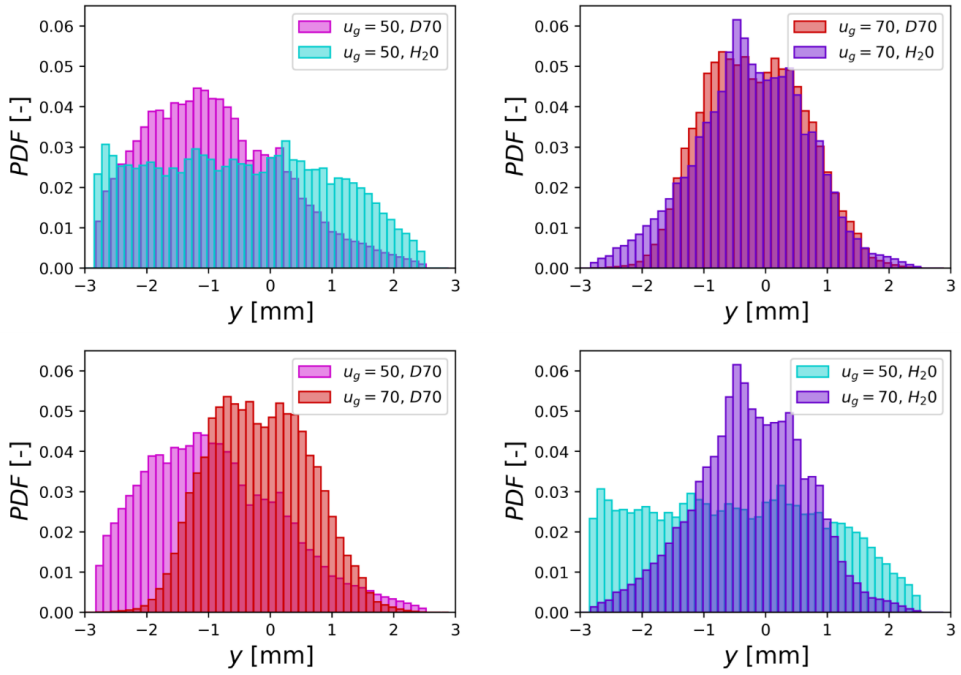

Figure 4.6: Droplet wall-normal location pdf comparisons: liquid influence for a given gas velocity (top), gas velocity influence for a given liquid (bottom).

PDFs in the subsequent Figures presented in this Section covers the entire domain.

Results show that the droplets are more concentrated around the prefilmer wall-normal location in the high velocity cases (OP#2 and OP#4), shaping a spray cone with a narrower angle. In these cases, the values of the parameter M are higher, and the accumulation of the film plays a less dominant role in the atomization mechanism, resulting in a smaller spray cone angle.

Conversely, in the low velocity cases (OP#1 and OP#3), the film (and its detached ligaments) preferentially breaks up either above or below the prefilmer in different instances due to film flapping, in accordance with the observations made in Section 4.1. As a single atomization event has been analyzed, there exists a bias in the droplet location along the Y-axis. This bias would probably be less pronounced with a statistically large enough sample of atomization events, which is not feasible with the DNS methodology employed. However, the observations regarding the dispersion around the prefilmer and the spray cone angle remain valid.

Next, Figure 4.7 shows comparisons among droplet diameter d_V pdfs to analyse the liquid influence for a given gas velocity and the velocity influence for a given liquid. In the first case, it can be seen that using Shellsol D70 as a liquid leads to a distribution with noticeably smaller droplets than the ones generated with H_2O-1,2-Propanediol, as it was qualitatively observed and justified in Section 4.1. Increasing gas velocity for a given liquid also leads to a finer atomization, even though the variation induced by the tested values of gas velocity led to shorter variations in the pdfs than the ones observed due to the differences in tested liquids. It is essential to remind from Section 3.2.2 and Figure 3.9 that, with the constant film thickness methodology, the large amount of droplets produced by *bag breakup* with a lower size hides the *ligament breakup* peak at a slightly higher size. This results in an apparent single mode breakup, in contrast to the obvious multimodal droplet size pdf observed in the variable film thickness methodology.

Last, the droplet velocity distributions are analysed, comparing the pdfs observed for each velocity component. It is important to note that all velocity

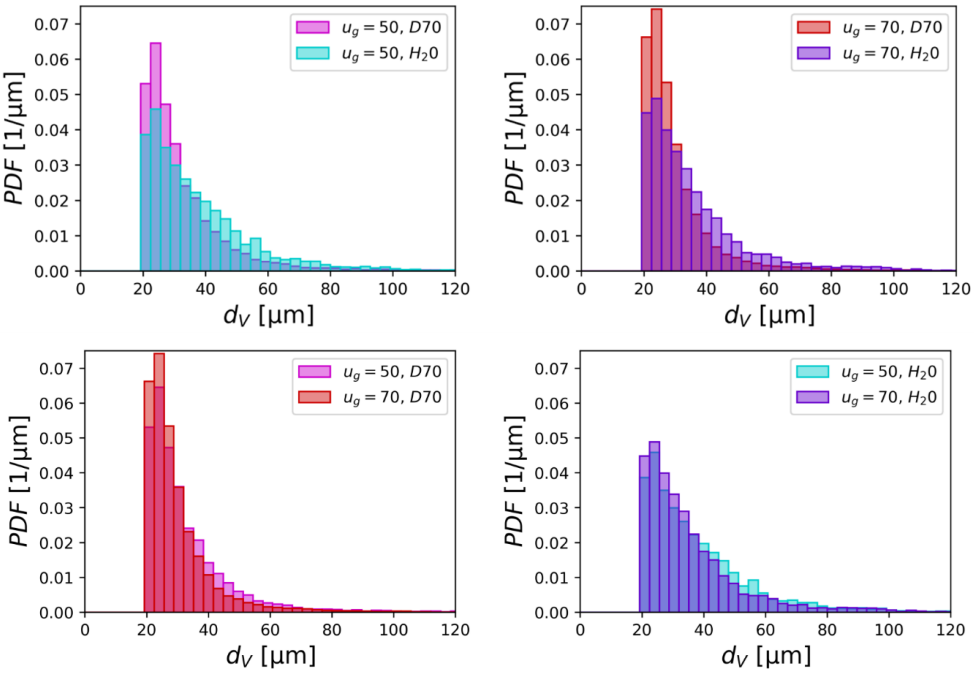

Figure 4.7: Droplet size pdf comparisons: liquid influence for a given gas velocity (top), gas velocity influence for a given liquid (bottom).

components have been normalized with the gas bulk velocity of each operating condition.

Figure 4.8 shows selected comparisons for the streamwise velocity component u of the droplets. It may be observed that using H_2O-1,2-Propanediol instead of Shellsol D70 leads to lower droplet velocities. The greater liquid viscosity in the former seems to reduce the momentum exchanged with the surrounding gas. Most importantly, the distribution seems to depart from a normal distribution, showing a certain bias. While this observation could be linked to the breakup mechanism, the distribution for OP#4 also presents this shape. On the other hand, while increasing the gas velocity for a given liquid also increases the absolute values of droplet streamwise velocity compared to the low velocity cases, the distribution for the normalized values is slightly shifted towards low normalized velocities. This suggests a loss in efficiency transferring momentum to the liquid when the gas momentum is increased as stated previously in the ligaments analysis (Section 4.2.1).

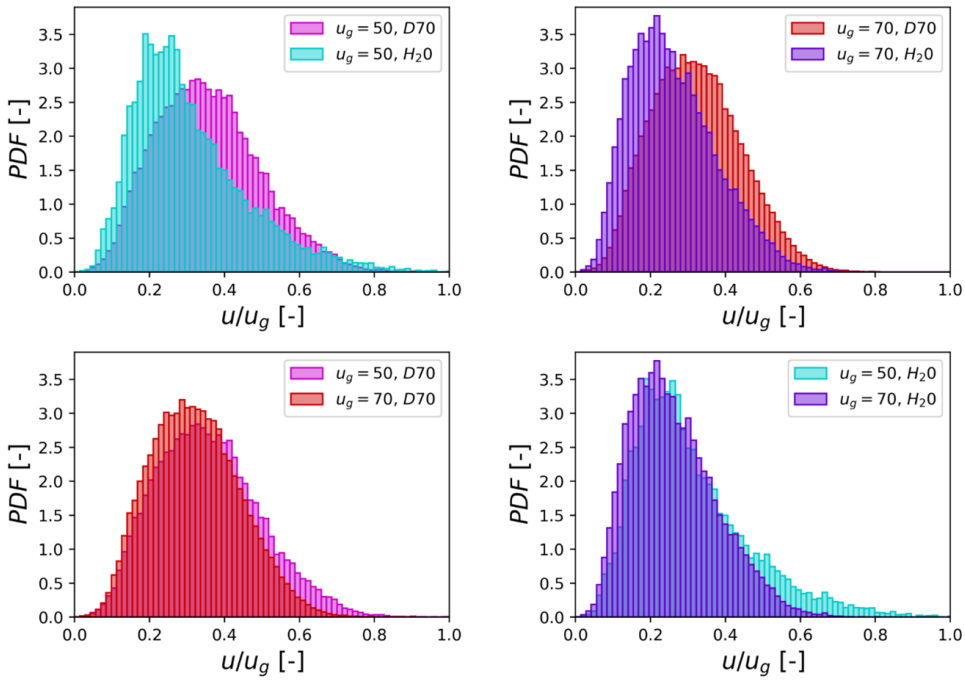

Figure 4.8: Droplet streamwise velocity pdf comparisons: liquid influence for a given gas velocity (top), velocity influence for a given liquid (bottom). Velocities are normalized with the gas bulk velocity for each operating condition.

As far as the droplet normalized wall-normal velocities v are concerned, the comparisons among pdfs are shown in Figure 4.9. Results show a noticeable influence of the liquid at low gas velocities (OP#1 and OP#3), with high asymmetry in the distributions, although this observation is not reproduced at high gas velocities. The differences in the low velocity cases may be attributed again to the violent film flapping observed in these conditions, scattering droplets not uniformly above and below the prefilmer. As reported in Section 4.1 and observed in Figure 4.10, the wall-normal velocity distributions of droplets generated above the prefilmer were biased towards positive values, whereas the ones for droplets generated below the prefilmer were biased towards negative values (i.e. most droplets tending to depart from the prefilmer in the wall-normal direction). Thus, generating more droplets either above or below the prefilmer, also biases the wall-normal velocity pdf. In any case, the comparisons from Figure 4.9 show that the influence of the gas velocity for a given liquid is not so accused. Increasing the gas velocity leads to a more

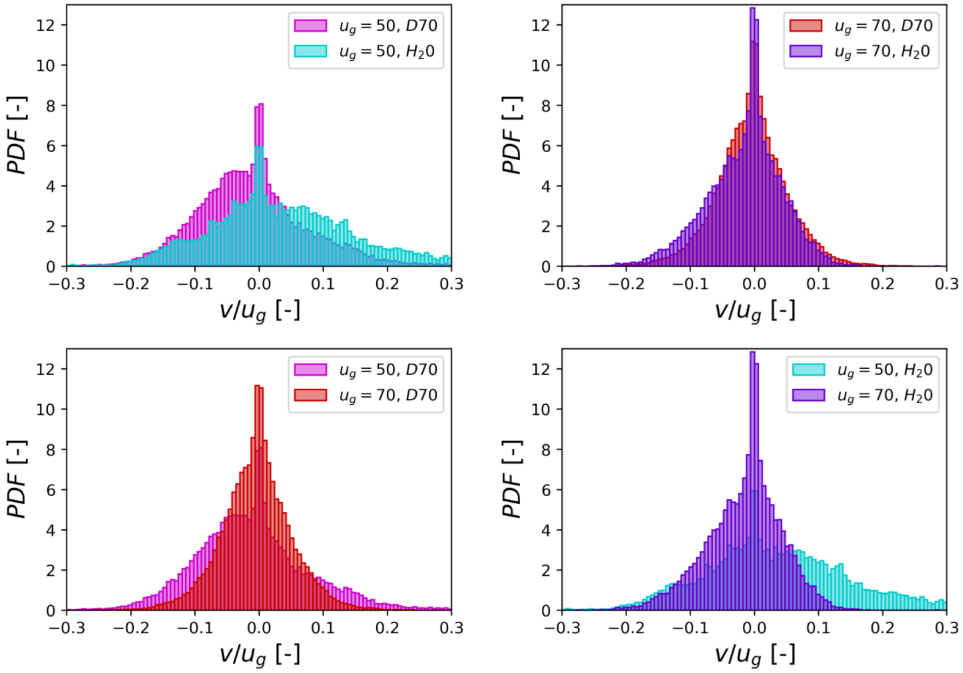

Figure 4.9: Droplet wall-normal velocity pdf comparisons: liquid influence for a given gas velocity (top), velocity influence for a given liquid (bottom). Velocities are normalized with the gas bulk velocity for each operating condition.

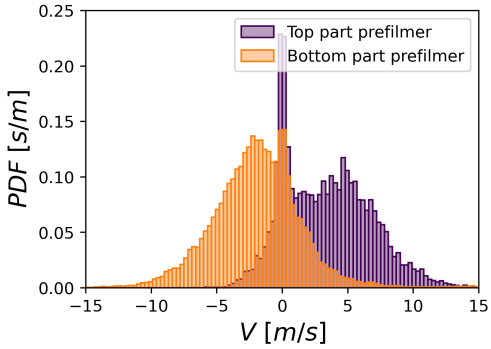

Figure 4.10: Wall-normal velocity pdf of the droplets generated above and below the prefilmer for the reference condition (OP#1).

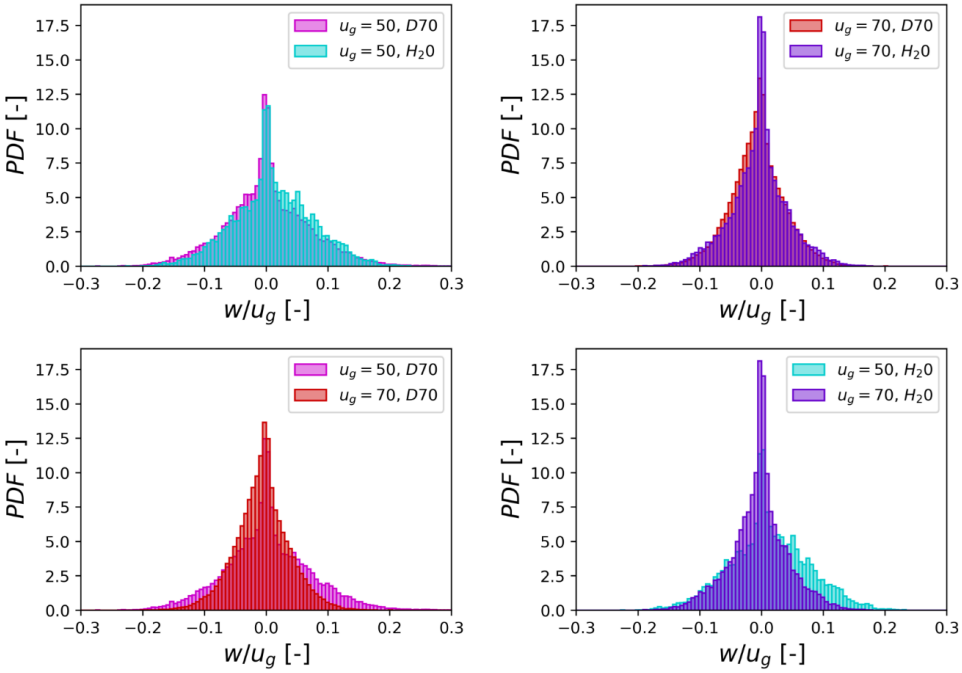

Figure 4.11: Droplet spanwise velocity pdf comparisons: liquid influence for a given gas velocity (left), velocity influence for a given liquid (right). Velocities are normalized with the gas bulk velocity for each operating condition.

symmetrical distribution, with lower normalized velocities and less dispersion around 0 in the distribution. However, it has been checked that the bias of the distribution for droplets falling above or below the prefilmer is still present.

Finally, the comparisons among the normalized spanwise velocity w pdfs are shown in Figure 4.11. No substantial differences among liquids are found in this case, as expected since droplets should be randomly scattered along the Z axis. For a given liquid, increasing the gas velocity reduces the dispersion of the distribution about the null velocities.

4.3 Conclusions

In this Chapter, the influence of several parameters on the primary breakup process in prefilming airblast atomizers has been discussed through the comparison of four simulations with different operating conditions, which involve the combination of two main gas velocities (50 m/s and 70 m/s) with two distinct liquids (Shellsol D70 and H_2O-Propanediol mixture), each characterized by unique thermophysical properties (i.e. liquid density, liquid viscosity, surface tension) and relevant dimensionless numbers (Reynolds, Weber, Ohnesorge, momentum flux ratio).

The methodology used is eDNS (recall first approach in Section 2.2 and Figure 2.5 left), where the air velocity introduced in the inflow boundary condition is variable to account for gas turbulence, but liquid velocity and film thickness are constant. This is due to the unexpected dewetting that appeared in some operating conditions when using the proposed novel approach with variable liquid velocity and film thickness combined with the cell sizes described in Section 2.2.3.2 for the reference condition. In those conditions implying the formation of a thinner liquid film above the prefilmer (i.e. at the inlet of the DNS), additional refinement would be required.

The qualitative analysis revealed that the atomization process reproduced a consistent pattern across different operating conditions, characterized by the formation of bags, followed by rim and ligament generation. The extent of liquid accumulation behind the prefilmer edge was found to influence the violence of the film flapping (only a single atomization event is analyzed, as currently a full statistical study through DNS is not feasible), impacting the uniformity and distribution of droplet production specially in the wall-normal direction. This behaviour was correlated with the momentum flux ratio M: lower velocity operating conditions (correponding to lower M values) which fit in the *torn-sheet breakup* regime produced more violent film flapping, opposite to the higher velocity operating conditions (corresponding to higher M values)

which fit in the *membrane-sheet breakup* regime. This is in line with the results found in the literature and the conclusions of the previous Chapter (Section 3.3).

Quantitative analysis, including ligaments and droplet properties, highlighted that atomization moved from a finer to a more inhibited state depending on M, Re, We and Oh. The pattern infered from the qualitative analysis is maintained for L_{bu} and L_{90} values, and is the opposite for the f_{main} ones. The results of the u_{lig} parameter are pretty close between operating conditions, and the same occurs with u_{def} for the *membrane-sheet breakup* regime cases. In the *torn-sheet breakup* regime cases, that value is slightly altered by the violent film flapping. As a result, f_{bu} is not consistent with the f_{main} trend. Ligament parameters and droplet characteristics demonstrated the impact of liquid properties, gas velocity and their interaction on the atomization process. Notably, gas velocity played a crucial role in reducing the dispersion of droplet velocities.

Further analysis of droplet properties revealed differences in droplet distributions in the wall-normal, streamwise and spanwise directions. Liquid properties significantly affect wall-normal velocity distributions, particularly at low gas velocities (lower Re_g) and low M values (torn-sheet breakup regime), causing asymmetry in the distributions due to the film flapping phenomenon. In contrast, normalized spanwise velocity distributions showed limited variations among liquids, with increased gas velocity reducing the dispersion around null values of wall-normal droplet velocity.

These findings provide valuable insight into the behaviour of prefilming airblast atomizers under different conditions, which are crucial for understanding and optimizing atomization processes in various applications. This analysis also lays the foundation for the development of a comprehensive atomization model discussed in Chapter 5, with potential applicability to both detailed simulations and 0D studies of engine performance.

Chapter 5

Proposal for the integration of the work developed in Lagrangian LES simulations

Simulation of primary breakup through VOF-DNS in prefilming airblast atomizers allowed identifying the features of this process specific to this kind of atomizers. The model proposed in the present Chapter links the gathered DNS data from the previous study to spray boundary conditions in reactive flow LES of spray flames, acting as a *spray generator*. Even though Lagrangian simulations are the main application of the model, it is worth noting that the model can also prove valuable in 0D studies and similar investigations. To increase the physical significance and accuracy of such simulations, the spray breakup model must consider this phenomenology, accounting for the following features:

- Variable liquid mass flow rate. The discontinuous nature of the planar prefilming airblast atomization for certain breakup mechanisms has been observed in many studies of the literature, as well as in Section 4.1 of the present thesis.
- Droplet size conditioned by droplet location, as a certain correlation could be found among these variables.

- Droplet velocity (in all components) conditioned by droplet size, as momentum exchange between gas and liquid is enhanced (i.e. droplets are more accelerated) the lower the droplet size. In prefilming airblast atomizers, the liquid is deposited on the prefilmer at a low speed, the gas being responsible for carrying it along together with its subsequent droplets. Momentum exchange takes place whenever a liquid structure is detached from the liquid film. In general, these structures are more affected by the gas bulk velocity the lower the droplet size.

- Droplet wall-normal velocity conditioned by droplet location, as the pdf of this magnitude for droplets generated above the prefilmer surface is biased towards positive values, the opposite being true for droplets falling below the prefilmer. This is due to the film flapping phenomenon as a single atomization event was analyzed (further explanation was given in Section 3.2).

In order to avoid extra degrees of freedom, it was decided for the model to only generate droplets at a certain axial location X. This way individual droplets do not need to be identified and tracked, avoiding numerical issues when introducing the liquid mass flow rate and simplifying the process. A detailed explanation about this matter will be given later in Section 5.2.2.

The algorithm to be used in the proposed spray generator according to the primary breakup model is introduced in Section 5.1. Details on how the primary breakup data obtained in Chapter 4 are treated to feed the algorithm are given in Section 5.2, where the model coefficients are introduced. Next, Section 5.3 shows the influence of the different operating conditions of Chapter 4 on the model coefficients. These coefficients are then in turn mathematically parameterized as a function of the relevant dimensionless groups associated to each operating condition. Finally, the main findings of this Chapter are summarized in Section 5.4.

5.1 Particle injection proposal overview

Although the proposed spray breakup model has various potential applications, the use of the model as an injection module for spray flame LES lagrangian simulations will be discussed hereinafter for illustrative purposes. Figure 5.1 sketches the algorithm of the primary breakup model followed to generate a droplet cloud.

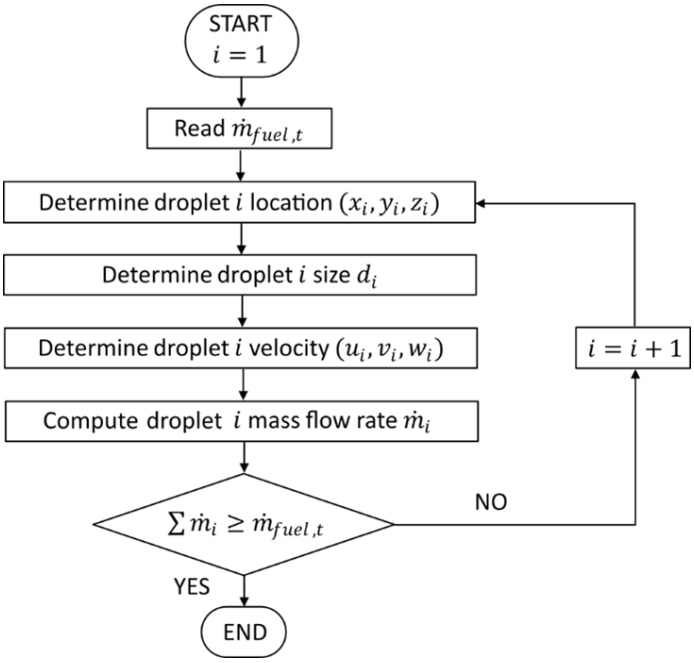

Figure 5.1: Overview of the algorithm followed by the proposed injection model at each time step t of a lagrangian simulation.

For each time step t of a lagrangian simulation, a droplet count i would be initialized. Then, the proposed steps of the injection module loop (each of them will be detailed in Section 5.2 for the reference condition) are as follows:

- **Step 0.** The liquid mass flow rate to be injected at the time step $\dot{m}_{fuel,t}$ will be read from the proposed model.
- **Step 1.** Next, the three coordinates of the i droplet location will be determined according to the breakup model. The axial location x_i is set to a fixed location, the wall-normal location y_i is computed from the breakup model parametrized pdf and the spanwise location z_i is assigned randomly.
- **Step 2.** Once the i droplet location is generated, its diameter d_i will be computed according to the breakup model parametrized pdf, which will condition droplet size with a certain dependence on the wall-normal position of the droplet y_i.

- **Step 3.** Then, the three components of its velocity will be computed as established by the primary breakup model. In this case, the breakup model conditions the streamwise velocity u_i by the droplet diameter d_i and the wall-normal velocity v_i by the droplet location y_i in order to account for breakup phenomenology.

- **Step 4.** The injected mass flow rate from all droplets $\dot{m}_i$ will be calculated from liquid density, droplet size and velocity. If the addition of the injected mass flow rate from all initialized droplets is lower than desired $\dot{m}_{fuel,t}$, another droplet is generated increasing by one the droplet count i and repeating this process from Step 1.

5.2 Data for breakup model derivation

For several magnitudes, generically denoted by X, the model will determine their value for an individual droplet according to probability density functions (pdf) of statistically processed data. Let us remind that the probability P that the magnitude value lies among two limits a and b is given by the pdf integration (also known as cumulative distribution function, cdf), according to Equation 5.1:

$$P(a < X_i \leq b) = cdf(b) - cdf(a) = \int_a^b pdf(X)dX \tag{5.1}$$

with the convenient property that the integration among $-\infty$ and ∞ is equal to 1. Hence, for all these X magnitudes, the model assigns the droplet property value as follows: whenever a property value must be determined according to a pdf, a random number between 0 and 1 is generated. The property value whose cdf matches the generated random number is then assigned to the droplet. This way, the generated values reflect the gathered DNS statistics. Since this is performed for all generated droplets, breakup phenomenology is recovered in a lagrangian simulation.

5.2.1 Step 0: Generation of the liquid mass flow rate temporal evolution

VOF-DNS predictions of the primary breakup in prefilming atomizers show, in agreement with the experimental data, that distinct atomization events take place. As a consequence, the introduction of atomized liquid into the combustion chamber does not take place at a continuous rate. Figure 5.2

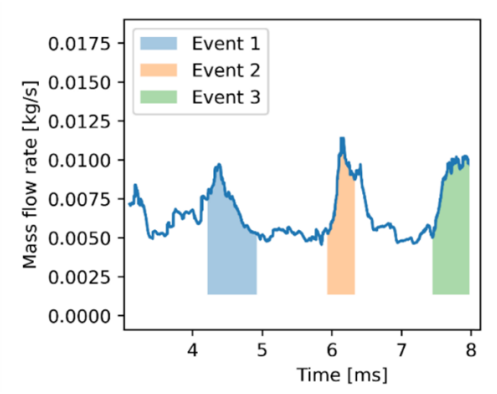

Figure 5.2: Temporal evolution of the atomized liquid mass flow rate post-processed in OP#1, including the depiction of distinct atomization events.

shows the temporal evolution of the atomized liquid mass flow rate for the OP#1, illustrating this fact.

As stated before, it is then essential for the phenomenological model to provide a variable mass flow rate signal rather than letting the proposed spray generator provide a constant mass flow rate at all times. Generally, lagrangian simulations will require a greater amount of simulated time to perform reacting flow predictions. Hence, one should be able to extend the VOF-DNS signal in the time domain.

To this end, the Fast Fourier Transform (FFT) of the DNS signal was performed, accepting that the normalized liquid mass flow rate can be expressed according to Equation 5.2:

$$\dot{m}_{norm}(t) = \frac{\dot{m}_{fuel}(t)}{\bar{\dot{m}}_{fuel}} = \sum_{n=1}^{N} A_n \cdot cos(2\pi \cdot f_n \cdot t + \theta_n) \tag{5.2}$$

where A_n and θ_n are the amplitude and phase of the f_n frequencies, respectively; whereas N is the number of terms considered in the series.

The FFT of $\dot{m}_{norm}(t)$ was truncated at 15 terms, whose most relevant frequencies, amplitudes and phases are shown in Table 5.1. These terms were enough to capture the relevant features of the signal, as it will be shown later. It may be seen that most relevant frequencies for the reference condition are harmonics of the first non-zero frequency $f_2 \approxeq 210\,\text{Hz}$, which corresponds to a period $T_2 \approxeq 4.762\,\text{ms}$ among two main atomizing events. The most relevant frequency is $f_4 \approxeq 630\,\text{Hz}$, which coincides with f_{main} in the reference operating condition (Table 4.3).

Table 5.1: Fourier Transform features of the 15 most relevant terms of the OP#1 normalized atomized mass flow rate signal.

n	f_n [Hz]	A_n [-]	θ_n [rad]
1	0	1.0000	0
2	209.996	0.1030	0.0891
3	419.992	0.1199	−1.4460
4	629.987	0.3165	1.1144
5	839.983	0.1820	1.7173
6	1049.979	0.0862	−0.0552
7	1259.975	0.1564	2.0909
8	1469.971	0.0607	2.7187
9	1679.966	0.0838	0.9921
10	1889.962	0.0305	1.8044
11	2099.958	0.0334	−0.9638
12	2729.945	0.0508	1.2770
13	3149.937	0.0394	0.5680
14	3359.933	0.0517	2.2500
15	4409.912	0.0340	1.2738

In order to extend the signal to any desired period of time without introducing undesired periodic features, a randomizing feature has been implemented. The strategy consists in letting the values of the main frequencies (and their corresponding amplitudes) evolve in time as per Equation 5.3:

$$\dot{m}_{norm}(t) = \frac{\dot{m}_{fuel}(t)}{\bar{\dot{m}}_{fuel}} = \sum_{n=1}^{N} A_n(t) \cdot cos[2\pi \cdot f_n(t) \cdot t + \theta_n] \tag{5.3}$$

where the variable $A_n(t)$ and $f_n(t)$ amplitudes and frequencies are obtained according to normal distributions using the frequencies (and amplitudes) shown in Table 5.1 as mean values and assigning them a certain standard deviation as a percentage of the mean values given by the k_A and k_f parameters:

$$\mu_{n,A} = A_n \qquad \text{and} \qquad \sigma_{n,A} = k_A \cdot \mu_{n,A} \tag{5.4}$$

$$\mu_{n,f} = f_n \qquad \text{and} \qquad \sigma_{n,f} = k_f \cdot \mu_{n,f} \tag{5.5}$$

Values of $A_n(t)$ and $f_n(t)$ are obtained for different time instants separated by a period 1.2 times higher than the period among atomizing events. This choice has proven effective in capturing and extending over time a trend similar

to that observed in the DNS processing, as demonstrated below. Their values at intermediate instants are then obtained by cubic interpolation among calculated instants. Values of $k_A = 0.01$ and $k_f = 0.025$ were found to generate reasonable time evolutions for $\dot{m}_{norm}(t)$, respecting airblast atomizer breakup phenomenology. An example of this generation for an extended time interval is shown in Figure 5.3. It may be seen that the strategy to generate extended signals with a randomized component still respects the average period among main atomizing events.

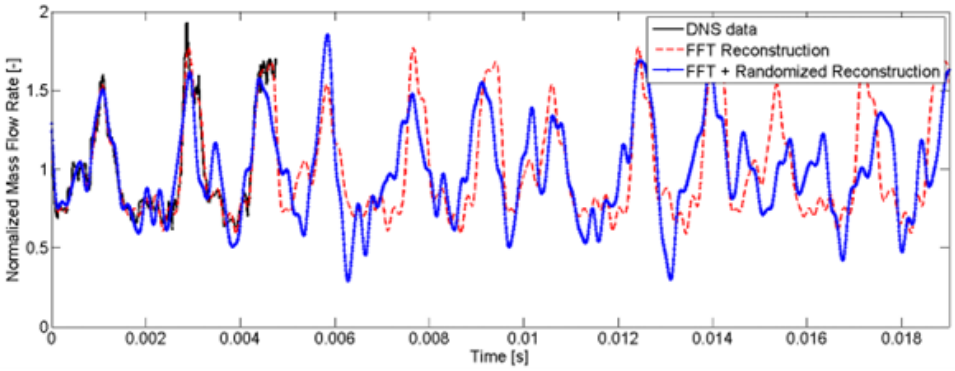

Figure 5.3: Temporal evolution of the normalized mass flow rate signal according to OP#1 data (black), FFT reconstruction of this signal extended for a larger time period (red) and randomized signal respecting the FFT main features (blue).

To sum up, the liquid mass flow rate to be injected by the spray generator at a given time instant is then given by Equation 5.6:

$$\dot{m}_{fuel,t} = \dot{m}_{norm,t} \cdot \bar{\dot{m}}_{fuel} \tag{5.6}$$

where $\dot{m}_{norm,t}$ is obtained from Equation 5.3 with the mean features synthesized in Table 5.1, and $\bar{\dot{m}}_{fuel}$ is the mean fuel mass flow rate prescribed.

This process has been illustrated with OP#1 (i.e. reference condition) DNS data as many atomizing events were simulated. However, due to the limited computational resources, only a single atomizing event (other than the transient) could be simulated for the remaining operating conditions (OP#2 to OP#4). For this reason, a main frequency among atomizing events is used instead. This frequency f_{main} was gathered from the period of time among the transient and the processed events. It was reported in Table 4.2, but it is displayed again in Table 5.2 for illustrating purposes.

Table 5.2: General primary breakup magnitudes obtained.

Parameter	OP#1	OP#2	OP#3	OP#4	Units
f_{main}	630.0	724.6	414.1	632.9	Hz

5.2.2 Step 1: Droplet location determination

At this step of the injection module algorithm, the three coordinates corresponding to the position of each individual droplet (x_i, y_i, z_i) must be determined respecting the primary breakup phenomenology observed in the VOF-DNS.

The DNS droplet post-processing strategy identifies individual droplets at each time step, but it does not track them along time steps. This is one major reason to focus on the droplets trespassing a given YZ plane: if several planes (or a whole volume) were considered, information about which droplets are carried among planes and which ones are newly generated is lost, potentially conditioning sizes and velocities erroneously. Therefore, it was decided to inject droplets at a given YZ plane (i.e. at a single axial location X from the prefilmer edge). In the frame of the ESTiMatE project (mentioned in Section 1.1), this premise was backed by the partners responsible of carrying out reactive lagrangian simulations using the proposed spray generator. Droplets were assumed to be spherical as they are meant to be injected in a Lagrangian framework.

A sensitivity study was carried out processing the OP#1 DNS data (location, size and velocity components) of droplets crossing YZ planes at the $L_{90} = 3.25\,\text{mm}$ distance from the prefilmer edge (recall Section 4.2.1) and further locations separated 0.5 mm among each other. This distance was chosen as most of the ligaments have disintegrated, so the remaining liquid structures are mainly spherical. Results of this analysis (Figure 5.4) show that droplet size (top-left), wall-normal velocities (bottom-left) and spanwise velocities (bottom-right) were not importantly modified among processing planes. Only the streamwise velocity pdfs (top-right) were significantly shifted towards greater values as the processing plane moved away from the prefilmer edge. This is reasonable due to the individually formed droplets exchanging momentum with the surrounding faster gas. In the context of a CFD simulation, the injected droplets would evolve in such a way, exchanging momentum with the gas as they move through the combustion chamber. With all, it was concluded that L_{90} can be considered representative of the primary breakup process and all droplets can be produced by the injection module at $x_i = L_{90}$. It should be noted that, as a result from this analysis, VOF-DNS droplet data

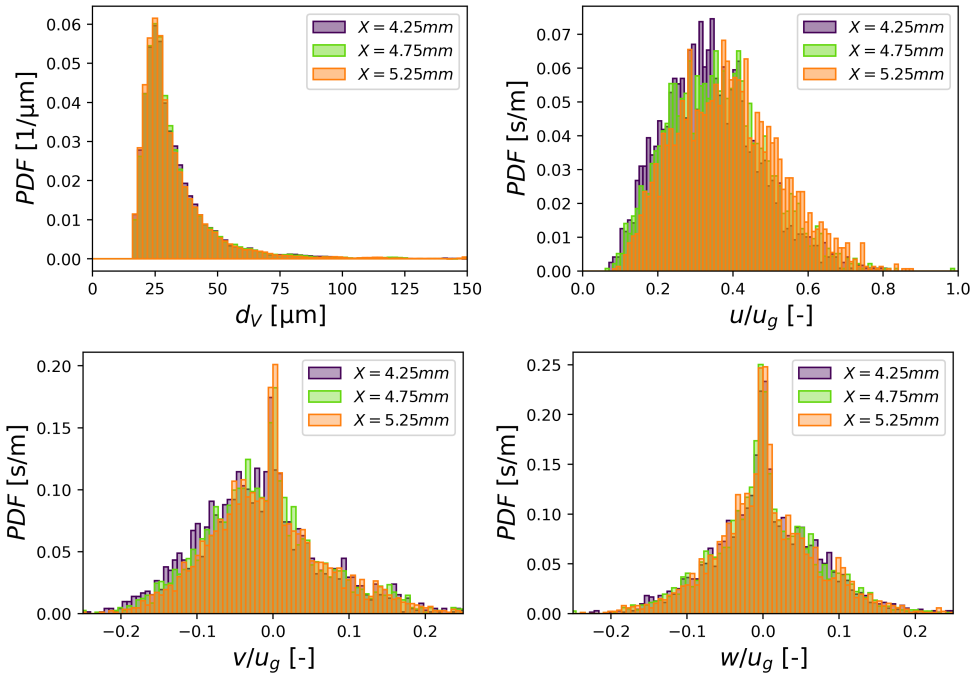

Figure 5.4: Sensitivity study of droplets crossing YZ planes at different distances from the prefilmer edge for the reference condition (OP#1). Pdfs show droplet size (top-left), streamwise velocities (top-right), wall-normal velocities (bottom-left) and spanwise velocities (bottom-right) respectively.

used to generate the primary breakup model was then exclusively sampled at the YZ plane corresponding location, not the whole domain as in previous Chapters 3 and 4.

As far as the wall-normal location y_i is concerned, droplet data were fitted to a Weibull distribution pdf as given by Equation 5.7, where α, β and γ are the shape, scale and threshold parameters of the Weibull distribution, respectively, whereas the subindex y refers to the y_i location pdf (please note that values of y are expressed in mm, $y = 0$ referring to the prefilmer center). A p-value greater than 0.05 ensured data could be significantly explained by this distribution with a 95% confidence interval. Upon droplet generation, the spray generator assigns the droplet wall-normal location y_i according to this pdf and the involved cdfs. The OP#1 processed droplet data for the chosen axial location and the resulting pdf are depicted in Figure 5.5. As stated in Section 4.2.2, a bias towards the negative side (bottom part of the domain

respect to the prefilmer) can be observed, although this does not always occur for the rest of the operating conditions. The choice of the Weibull distribution is convenient as it can represent both symmetrical and asymmetrical distributions depending on the fitting of its parameters.

$$pdf(y) = \frac{\alpha_y}{\beta_y^{\alpha_y}}(y-\gamma_y)^{\alpha_y-1} \cdot e^{-(\frac{y-\gamma_y}{\beta_y^{\alpha_y}})^{\alpha_y}} \tag{5.7}$$

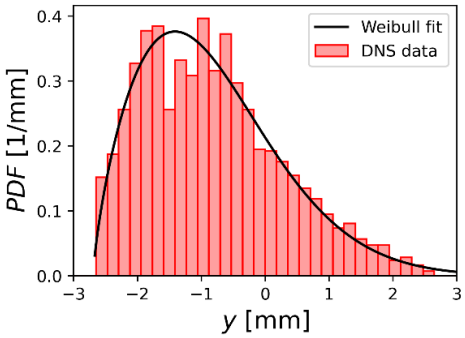

Figure 5.5: Droplet location pdf and Weibull fit for the reference condition (OP#1).

Last, it was checked from VOF-DNS data that droplets were randomly scattered spanwise. Hence, the spanwise location z_i is randomly assigned to each droplet.

In summary, values of the droplet location parameters and coefficients are compiled in Table 5.3 for all the operating conditions tested.

Table 5.3: Summary of the breakup model droplet location coefficients (Step 1) for each operating condition.

Parameter	Coefficient	OP#1	OP#2	OP#3	OP#4
x_i	L_{90}	0.003 25	0.002 76	0.0055	0.003 72
y_i	α_y	1.7364	2.6800	1.4695	3.6664
	β_y	2.0998	2.1742	2.4697	3.6541
	γ_y	−2.6930	−1.9161	−2.7068	−3.3954
z_i	-	-	-	-	-

5.2.3 Step 2: Droplet size determination

Droplet size is prescribed according to a size pdf gathered at the previously fixed axial location. Since information about the droplet wall-normal location y_i is already available from the previous Step (Section 5.2.2), the droplet diameter d_i pdf will be conditioned by this location. To do so, the droplet size pdf must be expressed as a function of two variables (d_i and y_i) rather than a single variable (d_i). To this end, specific droplet size pdfs were obtained for different y intervals. In order to avoid biasing data for drop size determination towards the y locations were more droplets were found in Step 1, these y intervals were not uniformly scattered among the DNS domain range (-3 to 3 mm). Intervals were rather chosen so that each of them represents the same cumulative number of droplets (i.e. cumulative density function, cdf, integration of the corresponding pdf). For each y interval, data were fitted to a lognormal distribution pdf of two parameters (μ and σ, with the subindex d referring to the d_i droplet size). A statistical fit was applied to the values of the μ_d and σ_d parameters of these *y-specific pdfs* in order to express both of them as a function of y, taking the central point of each interval as the representative point for the fitting and resulting in Equations 5.8 to 5.12:

$$pdf(d,y) = \frac{1}{d\ \sigma_{logscale}(y)\ \sqrt{2\pi}} \cdot e^{-\frac{[\ln d - \mu_{logscale}(y)]^2}{2\ [\sigma_{logscale}(y)]^2}} \tag{5.8}$$

where:

$$\mu_{logscale}(y) = \ln\left(\frac{[\mu_d(y)]^2}{\sqrt{[\mu_d(y)]^2 + [\sigma_d(y)]^2}}\right) \tag{5.9}$$

$$\sigma_{logscale}(y) = \sqrt{\ln\left(1 + \frac{[\sigma_d(y)]^2}{[\mu_d(y)]^2}\right)} \tag{5.10}$$

$$\mu_d(y) = \mu_{d2} \cdot y^2 + \mu_{d1} \cdot y + \mu_{d0} \tag{5.11}$$

$$\sigma_d(y) = \sigma_{d1} \cdot y + \sigma_{d0} \tag{5.12}$$

Values of the fitted lognormal distribution parameters are compiled for all tested operating conditions in Table 5.4 (please note that values of d are expressed in µm; values of y are expressed in mm, $y = 0$ referring to the prefilmer center). The resulting 2-variable *size-location pdf* obtained for the reference condition is depicted in Figure 5.6 for illustrating purposes.

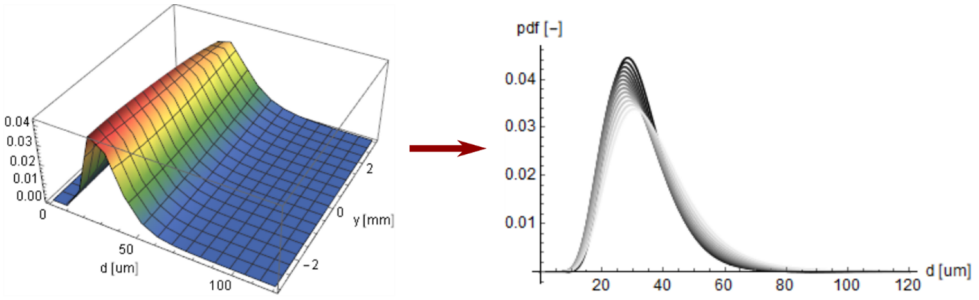

Figure 5.6: 2-variable droplet size-location pdf (left) and slices for several sample y locations (right) increasing y from dark ($y = -3\,\mathrm{mm}$) to bright ($y = 3\,\mathrm{mm}$) for OP#1.

Table 5.4: Summary of the breakup model droplet size coefficients (Step 2) for each operating condition.

Parameter	Coefficient	OP#1	OP#2	OP#3	OP#4
d_i	μ_{d0}	32.583	29.951	40.191	36.163
	μ_{d1}	0.7713	−0.1779	−0.9279	−0.0645
	μ_{d2}	0.2485	−0.2497	−0.8084	−0.1363
	σ_{d0}	11.968	8.990	15.886	14.703
	σ_{d1}	0.6356	−0.2451	−0.3412	0.1847

5.2.4 Step 3: Droplet velocity determination

Droplet velocity (u_i,v_i,w_i) is prescribed according to the pdf for each velocity component gathered at the previously fixed axial location. Since information about the droplet size is already available from the previous Step (Section 5.2.3) and the size and velocities have shown to be strongly correlated, the pdf for each velocity component will be conditioned by droplet diameter. Analogously to what was explained in Step 2, the pdf for each velocity component was then expressed as a function of two variables (the velocity component and droplet size). To this end, specific velocity component pdfs were obtained for different d_v intervals. The parameters of each pdf could then be expressed as a function of d_v. It is important to note again that, in order to avoid biasing data for drop velocity determination in Step 3 towards the sizes were more droplets were found in Step 2, these d_v intervals were not uniformly scattered among the droplet size range. Intervals were rather chosen so that each of them represents the same cumulative number of droplets.

All velocity components were normalized by the mean gas velocity according to Equation 5.13.

$$u_{norm} = u/\overline{u_g} \qquad v_{norm} = v/\overline{v_g} \qquad w_{norm} = w/\overline{w_g} \tag{5.13}$$

Starting with the normalized streamwise droplet velocity component u_{norm}, DNS data were found to properly fit to a Weibull distribution according to Equation 5.14:

$$pdf(u_{norm}, d) = \frac{\alpha_u(d)}{\beta_u(d)^{\alpha_u(d)}} \cdot (u_{norm} - \gamma_u)^{\alpha_u(d)-1} \cdot e^{-(\frac{u_{norm}-\gamma_u}{\beta_u(d)^{\alpha_u(d)}})^{\alpha_u(d)}} \tag{5.14}$$

where:

$$\alpha_u(d) = \alpha_{u0} \cdot d^{\alpha_{uexp}} \qquad \text{and} \qquad \beta_u(d) = \beta_{u0} \cdot d^{\beta_{uexp}} \tag{5.15}$$

Values of the fitted Weibull distribution parameters are compiled for all tested operating conditions in Table 5.5. The resulting 2-variable *velocity-size pdf* obtained for the reference condition is depicted in Figure 5.7 (left) for illustrating purposes. This *velocity-size pdf* then represents a succession of velocity pdfs for all d_i sizes, and allows conditioning the droplet streamwise velocity u_i of a specific droplet by its diameter d_i obtained in Step 2. To exemplify this, Figure 5.7 (right) shows the pdfs extracted in OP#1 for different values of d_i.

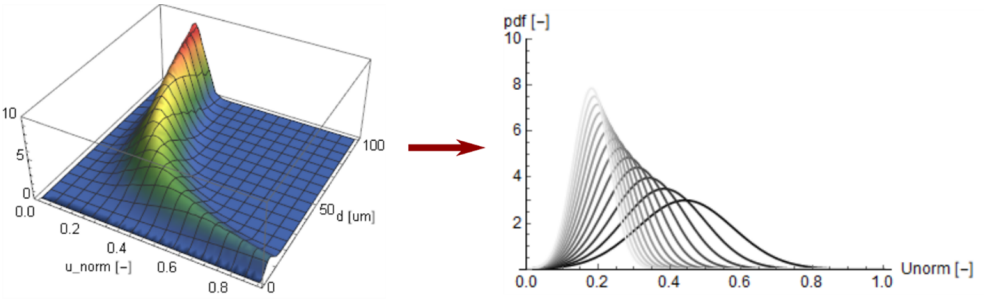

Figure 5.7: 2-variable droplet normalized streamwise velocity-size pdf (left) and slices for several sample d diameters (right) increasing d from dark ($d = 20\,\mu$m) to bright ($d = 80\,\mu$m) for OP#1.

As far as the normalized wall-normal droplet velocity component v_{norm} is concerned, DNS data were fitted to a logistic distribution according to Equation 5.16, with $q = \sqrt{3}/\pi$. It must be noted that the parameters of the

logistic distribution are different depending on whether the injected droplet has fallen above or below the prefilmer. This feature also conditions the droplet wall-normal velocity v_i by droplet location y_i in order to account for airblast atomization phenomenology as seen previously in Figure 4.10.

$$pdf(v_{norm}, d) = \frac{1}{q\ \sigma_v(d)} \cdot \frac{e^{-\left[\frac{v_{norm}-\mu_v(d)}{q\ \sigma_v(d)}\right]}}{\left\{1 + e^{-\left[\frac{v_{norm}-\mu_v(d)}{q\ \sigma_v(d)}\right]}\right\}^2} \tag{5.16}$$

where:

$$\mu_v(d) = \begin{cases} \mu_{v0bot} \\ \mu_{v0top} \end{cases} \quad \text{and} \quad \sigma_v(d) = \begin{cases} \sigma_{v0bot} \cdot e^{\sigma_{vexpbot} \cdot d} & \text{if } y_i \leq 0 \\ \sigma_{v0top} \cdot e^{\sigma_{vexptop} \cdot d} & \text{if } y_i > 0 \end{cases} \tag{5.17}$$

Values of the fitted logistic distribution parameters are compiled in Table 5.5. The resulting 2-variable *velocity-size pdfs* above and below the prefilmer

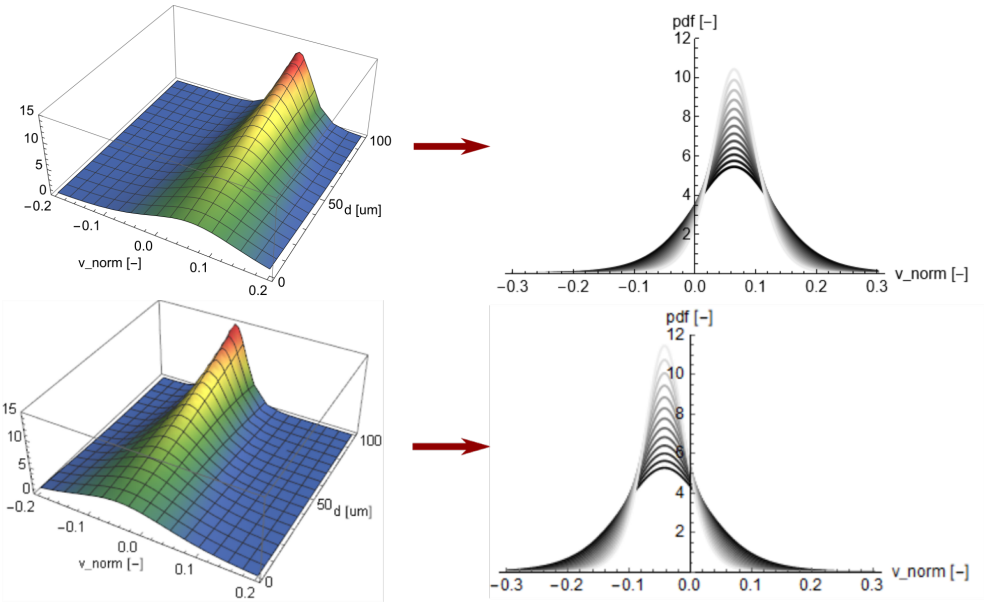

Figure 5.8: 2-variable droplet normalized wall-normal velocity-size pdfs (left) and slices for several sample d diameters (right) increasing d from dark ($d = 20\,\mu$m) to bright ($d = 80\,\mu$m) for OP#1. The top and bottom images represent both parts of the domain (above $y > 0$ and below $y \leq 0$ the prefilmer) respectively.

respectively are depicted in Figure 5.8 (left). These *velocity-size pdfs* then represent a succession of velocity pdfs for all d_i sizes, and allows conditioning the wall-normal velocity v_i of a specific droplet by its diameter d_i obtained in Step 2 and its wall-normal location y_i obtained in Step 1. Figure 5.8 (right) shows the extracted pdfs for different values of d_i.

Last, in the case of the normalized spanwise droplet velocity component w_{norm}, DNS data were fitted to a Laplace distribution according to Equation 5.18. The value of μ_w was so small that, given the simmetry of the problem and the inherent randomness along the Z-axis, a pragmatic choice was made to set $\mu_w = 0$. The parameter $\lambda_w(d)$ is given by Equation 5.19.

$$pdf(w_{norm}, d) = \frac{\lambda_w(d)}{2} \cdot e^{-\lambda_w(d)|w_{norm} - \mu_w|} \tag{5.18}$$

$$\lambda_w(d) = \lambda_{w0} \cdot d^{\lambda_{wexp}} \tag{5.19}$$

Values of the fitted Laplace distribution parameters are compiled for all tested operating conditions in Table 5.5. The resulting 2-variable *velocity-size pdf* obtained for the reference condition is depicted in Figure 5.9 (left) for illustrating purposes. This *velocity-size pdf* then represents a succession of velocity pdfs for all d_i sizes, and allows conditioning the droplet spanwise velocity w_i of a specific droplet by its diameter d_i obtained in Step 2. Figure 5.9 (right) shows the extracted pdfs for different values of d_i. As it can be seen, the effect of the droplet size on spanwise velocity component is almost negligible. Hence, in a simplified version of the model a single-variable pdf could be used.

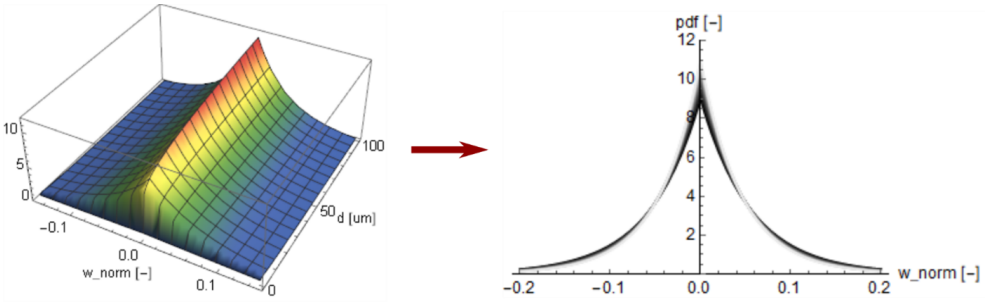

Figure 5.9: 2-variable droplet normalized spanwise velocity-size pdf (left) and slices for several sample d diameters (right) increasing d from dark ($d = 20\,\mu$m) to bright ($d = 80\,\mu$m) for OP#1.

Table 5.5: Summary of the breakup model droplet velocity coefficients (Step 3) for each operating condition.

Parameter	Coefficient	OP#1	OP#2	OP#3	OP#4
$u_{norm,i}$	α_{u0}	3.4575	6.6530	6.8717	4.0444
	α_{uexp}	−0.004 58	−0.239	−0.268	−0.0968
	β_{u0}	5.7078	3.2199	4.4667	4.1347
	β_{uexp}	−0.858	−0.750	−0.846	−0.815
	γ_u	0.0620	0.0528	0.0887	0.0493
$v_{norm,i}$	μ_{v0bot}	−0.042 26	−0.031 04	−0.027 72	−0.039 42
	σ_{v0bot}	0.1109	0.0632	0.1714	0.0798
	$\sigma_{vexpbot}$	−0.0129	−0.0070	−0.0113	−0.0110
	μ_{v0top}	0.064 57	0.026 76	0.079 15	0.017 47
	σ_{v0top}	0.1033	0.0692	0.0892	0.0496
	$\sigma_{vexptop}$	−0.0108	−0.008 37	−0.008 33	−0.006 10
$w_{norm,i}$	λ_{w0}	11.666	8.8526	5.3925	4.7227
	λ_{wexp}	0.1448	0.3401	0.3780	0.5408

5.3 Spray breakup model parametrization

The variations among operating conditions in the *conditioned pdfs* coefficients shown in Table 5.5 were tried to be related to the variations in the functioning parameters of each operating condition, gathered in Table 5.6. The dimensionless groups known to be relevant in primary atomization were selected, prioritizing those that yielded a larger R^2 coefficient in the correlations. This coefficient is also reported for each fitting so that its quality can be assessed.

The value of h_l obtained for each operating condition was modelled in turn through these functional parameters, as it is also a parameter that may explain the variability between OPs in some results. On the other hand, main frequency f_{main} depends directly on M and the square root of We_l.

Regarding droplet position, the streamwise coordinate parameter L_{90} was correlated with the momentum flux ratio M and with the tradidional Weber number We_l, while the spanwise coordinate parameter was randomized because of the symmetry in the domain. The wall-normal coordinate parameters α_y and β_y (shape and scale of the Weibull distribution) could be linked to gas velocity through and breakup regime (through Re_g and M), but the γ_y location threshold provided better a fitting with Weber numbers We_h and We_l.

Table 5.6: Summary of the expressions used to correlate the model coefficients obtained for each operating condition with their functional parameters.

	Parameter	Coefficient	Expression	R^2
General	h_l	-	$0.0001274 + 3.253 \cdot 10^{-9} Re_g - 1.0229 \cdot 10^{-5} We_l$	1
	f_{main}	-	$-1685.87 - 34.407M + 973.191\sqrt{We_l}$	0.9982
Step 1	x_i	L_{90}	$0.01301 + 0.0005275M - 0.002090We_l$	0.9801
	y_i	α_y	$-4.1269 + 0.0005204Re_g - 0.09278M$	0.9212
		β_y	$-2.8278 + 0.0005664Re_g - 0.1821M$	0.9622
		γ_y	$0.5826 + 0.1825We_h - 0.9072We_l$	0.9929
Step 2	d_i	μ_{d0}	$23.972 + 0.02120\rho_l - 0.8452We_l$	0.9856
		μ_{d1}	$4.4831 - 0.004760\rho_l - 1.012 \cdot 10^{-5} We_\delta^2$	0.5622
		μ_{d2}	$1.2647 - 0.001982\rho_l + 1.613 \cdot 10^{-5} Re_g$	0.4019
		σ_{d0}	$5.3771 + 0.01248\rho_l - 0.02074We_\delta$	0.9957
		σ_{d1}	$2.8831 - 0.002835\rho_l - 3.865 \cdot 10^{-8} We_\delta^3$	0.6011
Step 3	$u_{norm,i}$	α_{u0}	$-18.078 + 227459h_l + 0.004483We_h^2$	0.9783
		α_{uexp}	$3.1376 - 27141.9h_l - 0.006161We_\delta$	0.9878
		β_{u0}	$23.4149 - 148888h_l - 0.2292We_h$	0.9438
		β_{uexp}	$-1.3568 + 3788.87h_l + 0.007685We_h$	9926
		γ_u	$-0.04426 + 1132.74h_l + 0.008853Re_l$	0.7951
	$v_{norm,i}$	μ_{v0bot}	$-0.2128 + 1479.03h_l + 3.269 \cdot 10^-4We_\delta$	0.9414
		μ_{v0top}	$0.01555 + 637.297h_l - 1.206 \cdot 10^-4We_\delta$	0.5184
		σ_{v0bot}	$-0.02509 + 3204.21h_l - 1.477 \cdot 10^{-4}\rho_l$	0.9483
		σ_{v0top}	$0.1474 + 1677.91h_l - 2.331 \cdot 10^{-4}\rho_l$	0.9993
		$\sigma_{vexpbot}$	$-0.02342 + 7.782 \cdot 10^{-6}\rho_l + 3.450 \cdot 10^{-5} We_\delta$	0.8013
		$\sigma_{vexptop}$	$-0.02793 + 1.786 \cdot 10^{-5}\rho_l + 2.113 \cdot 10^{-5} We_\delta$	0.9788
	$w_{norm,i}$	λ_{w0}	$35.6238 - 0.02818\rho_l - 0.09799We_h$	0.9884
		λ_{wexp}	$-1.0081 + 0.001220\rho_l + 0.01338M$	0.9993

Concerning droplet size, all parameters scaled with ρ_l, which is not a dimensionless parameter per se. This implies that, irrespective of the dimensionless groups, the liquid density plays a significant role in the droplet size distribution. For the calculation of the mean droplet size, We_l and We_d were required, but for the standard deviation only We_δ was found to be necessary. The non-linearity of the mean with the conditions could be related to Re_g.

In relation to normalized droplet velocities, every component is analyzed individually. The mean liquid film height h_l was found to influence all parameters for the streamwise velocity distribution. The shape and scale parameters of the Weibull distribution selected could be related to Weber numbers We_h and We_δ, showing that the atomizing edge thickness affected both of them linearly, but the scale one is affected exponentially. The exponential part of the shape parameter depends on the boundary layer thickness. The remaining location parameter was also modelled with Re_l. Each of the Logistic distributions used for the wall-normal velocity has two parameters each, namely mean and scale (proportional to the standard deviation), both of them found to be linearly correlated with h_l. The dimensionless number We_δ also had an influence on them, linear for the mean parameter but exponential for the standard deviation. Moreover, liquid density ρ_l was found not only to be key for the standard deviation parameter of this distribution (in both linear and exponential manners), but also for the scale parameter of the spanwise velocity distribution. This one could also be linearly related to the atomizing edge thickness (through We_h) and exponentially related to the breakup regime (through M).

It is also important to acknowledge some limitations of the proposed model. The main drawback is that only 4 conditions could be used to derive the model, not constituting a large database to completely cover the two different atomization regimes identified in the performed simulations. The validity of the proposed model is thus not known beyond its range of determination. Furthermore, while most correlations present values of R^2 close to 1, a few values are below 0.8. Most pdf coefficients with lower R^2 values involved a non-linear function in order to achieve pdf conditioning, so even if the value of the correlation was perfect, the model still would not describe relevant non-linear or crossed effects.

5.4 Conclusions

The workflow to develop an injection model has been proposed, considering the complexities of airblast atomization. This methodology incorporates a

variable mass flow rate, conditions the size distribution of injected droplets on their wall-normal location, and determines the velocity distribution of droplets based on that size. The injection has been chosen to occur at a single axial location, although this condition could be relieved at the expense of increasing the complexity of the model. However, this change in the model could induce numerical instabilities when using it as a boundary condition for CFD simulations.

The spray generator links the features of the atomized droplet cloud, such as drop size and velocity to the functional parameters related to different operating conditions, including gas and liquid properties. This link was established by correlating the expressions of the droplet pdfs to relevant dimensionless groups known to influence primary atomization (namely Re_g, Re_l, We_l, We_h, We_δ, M) or to the liquid film thickness (h_l) and liquid density. If the tested OPs had included pressurized conditions, this would have been replaced by the liquid-gas density ratio.

The proposed model is characterized by its ease of implementation and has been tested by other partners within the ESTiMatE project. The behaviour of the spray generator when used to inject lagrangian particles in reacting LES of spray flames for the reference condition has been assessed by García et al. [119], ensuring the proper reproduction of the droplet cloud determined in the specific primary breakup high-fidelity simulations.

The limitations of the model were also analysed, having into account that only 4 operating conditions were used to derive the proposed model so the validity is uncertain outside its range of determination. However the presented workflow demonstrates that it is possible to derive a complete primary breakup model from specific high-fidelity simulations following the proposed methodology. Hence, the application of the procedure developed to further operating conditions should allow a larger dataset to derive a universal primary breakup model or, at least, to identify different submodels for each atomization regime relevant to prefilming airblast atomizers.

Chapter 6

Conclusions and future works

This chapter summarizes the main findings of the dissertation, emphasizing their potential to inspire additional analysis and future research.

6.1 Conclusions

This work contributes to the understanding of primary atomization in air-blast atomizers through a comprehensive investigation encompassing methodology, boundary conditions, parametric analysis and the development of a phenomenological model. The findings are expected to provide valuable insight for optimizing atomizer design and enhancing atomization efficiency across a range of engineering applications, specially in the context of aero engines. Moreover, the development of the *spray generator* tool serves as a bridge between the obtained results of the primary atomization framework and subsequent physiochemical processes in the engine, facilitating a more comprehensive understanding of these interconnected phenomena.

A numerical investigation has been performed through VOF-DNS simulations of the atomizing edge to obtain useful data using the embedded DNS (eDNS) methodology. This methodology consists on computing single-phase LES precursor simulations to gather turbulent data for the inflow conditions of the main simulation, assuming the flow between both computational domains is one-way coupled. These precursor simulations were succesfully validated against consolidated experimental and DNS computational data in the literature, comparing mean streamwise velocity profiles (law of the wall) and root

mean square (RMS) velocity components. Additional two-phase LES precursor simulations have been proposed in this thesis to extend the eDNS concept, getting the liquid film to develop along the prefilmer. Depending on the inflow conditions, the methodolody is splitted into two new variations:

- The first method considered both constant liquid film thickness and velocity at the domain inlet, but a variable gas inlet velocity to account for the turbulence of the gaseous phase. The only difference with the actual eDNS method by Sauer et al. [45] is the film thickness is obtained by processing the results of the extra two-phase LES precursor simulations instead of being a theoretical or experimental value.
- The second method considered all gas and liquid features (velocities and thickness) as variable, both timewise and spanwise, to also account for the spatio-temporal evolution of the liquid film thickness upstream of the prefilmer edge. Snapshots of a plane perpendicular to the flow direction are obtained from the two-phase LES precursor simulations, mapping these values as an input boundary condition of the VOF-DNS main simulation.

To achieve a comprehensive evaluation of the DNS simulation results, some post-processing tools have been implemented and applied. Additionally, a methodology to post-process ligament data not only in a 2D projection but in a 3D domain was also proposed. A threshold α value has been chosen based in the ones found in the literature to identify individual liquid structures all over the domain. The main and larger structure, encompassing both the film and any ligament directly connected to it, is recognized as the intact core, distinguished from the droplet cloud and any ligaments that have become detached. This enabled independent processing of both kinds of liquid structures.

- Regarding the intact core and ligaments analysis, two different approaches have been adressed:
  - As the experimental data found in the literature consists of 2D shadowgraphy images, the liquid data obtained from the DNS has been projected onto the prefilmer plane and binarized for a succesful qualitative comparison with validation purposes.

    To extract the ligaments from the liquid core, a method has been proposed to process the resulting 2D images of each timestep. A

cutting and smoothing algorithm was created to isolate them, and a connectivity filter was used to identify them.

A novel method based on the Fast Marching Method has been proposed in this thesis to obtain a better approximation of the ligament length. It gives the distance of the continuous shortest path between the prefilmer edge and each ligament tip, obtaining higher ligament lengths as one-dimensional limitations of the older method are no longer present.

The method for determining other relevant parameters related to ligaments in the literature, such as film deformation velocity, is strongly dependent on spatiotemporal resolution. Instead, it has been proposed to calculate these velocities by projecting them into the prefilmer plane, summing their values weighted by α. Validation of this method has been successful and appears to be more robust.

– A 3D approach to post-process liquid structures in sprays has been proposed and implemented as one of the main contributions in this thesis to avoid the information loss during the projection procedure. This approach preserves the three-dimensional representation of the ligament structures, obtaining more accurate ligament lengths (the Fast Marching Method also applies in 3D) and velocities.

  An additional ligament equivalent diameter has been defined from length and volume to correlate with the size of generated droplets during atomization process.

Some additional parameters were used to describe the breakup process regardless of whether the ligaments were treated in a two-dimensional or three-dimensional manner, averaging magnitudes across all time steps: breakup length, mean ligament tip velocity, mean film deformation speed. From those values, a mean breakup frequency was estimated.

- The droplet cloud has been analyzed using the method found in the literature for a round spray. Assuming spherical droplets, volumetric diameters and droplet velocities were computed, as well as other relevant properties (Reynolds, Weber and Ohnesorge dimensionless numbers).

Both proposed variations of the eDNS method have been performed for a widely studied operating condition in order to compare the accuracy of the results and discuss the computational costs of the simulations. In both cases,

the predicted breakup mechanism sequence obtained was in accordance to the momentum flux ratio: liquid accumulation, bag formation, bag breakup, ligament formation and ligament breakup. These liquid structures were analyzed using the postprocessing tools explained previously.

Qualitative comparisons between both simulation strategies for the reference condition revealed important differences in terms of ligament distribution and droplet cloud, although having the same momentum flux ratio. The variable case, which considers the liquid film evolution upstream of the prefilmer edge, resulted in a less uniformly distributed spanwise liquid reservoir behind the edge, as film crests and valleys are less synchronized along the prefilmer span. This results in a less violent bag breakup event and a more continuous atomization process in time than the constant liquid film thickness case, inhibiting atomization to a certain extent but producing breakup more continuously in time. Both approaches yielded a higher number of droplets generated through bag breakup compared to ligament breakup, but the latter mechanism became more significant for the variable film thickness strategy. Furthermore, the ligaments predicted using this strategy exhibited a larger equivalent diameter than the ones in the constant case, enabling the prediction of a multimodal drop size distribution as the one reported from experimental results in the literature.

Quantitative validation against experimental data in the literature showed reasonable agreement for both simulations, with better predictions obtained when accounting for the liquid film evolution along the prefilmer surface despite not accounting for the absolute nature of the interfacial instability produced at this location. The multi-modal droplet size distribution seen in experiments could only be reproduced using the novel proposed methodology. Differences of the spray spreading in the wall-normal direction between methods caused variations in velocities distributions, splitted among velocity components: accounting for liquid film evolution lead to a narrower droplet cone than the one obtained in the opposite case. In the latter, film flapping was strongly present as the behaviour of the film was very uniform across spanwise locations, meaning all the shaped bags get punctured and break up at the same stage and droplets are generated mostly at the same side of the prefilmer. The averaged and aggregated quantities considered in this case might be biased by the lack of variability as only a few breakup events were simulated, but this limitation is attenuated if the novel proposed methodology is used.

The choice between constant and variable liquid film thickness methodologies hinges on the specific aspects of the atomization process that one aims

to capture. The constant thickness approach offers simplicity and computational efficiency, obtaining isolated violent breakup events and allowing for a broad overview of the breakup process. Nevertheless, the variable thickness methodology provides a more detailed and accurate representation of the liquid film evolution, breakup is more continuous in time and less uniform spanwise. Droplet size, positions and velocities distributions are closer to the experimental results, especially in scenarios where film thickness variations significantly influence the atomization dynamics. However, unless a more aggressive cell refinement (unfeasible in the scope of the present thesis) is achieved, it might struggle to represent particularly thin films and is subject to phenomena like non-physical dewetting.

The limitations of the comparative study between both methodologies within the framework of the thesis will be discussed hereunder. This comparison was limited to a specific operating condition where liquid accumulation behind the prefilmer edge is key, and the breakup frequency is partially decoupled from the film wave frequency. It is acknowledged that conditions with higher gas-to-liquid momentum flux ratios, as found in aero engines, may lead to different breakup regimes where breakup frequency is expected to be more closely coupled to the film wave frequency, but the proposed methodology could also yield more accurate predictions for them.

It must be noted that both approaches assume that perturbations exclusively propagate downstream from the instability source, which is true when the interfacial instability generated in the planar airblast atomizer is convective. This is not true for the operating conditions analyzed in this study, requiring a computation of the complete atomizer geometry for a detailed analysis on the absolute interfacial instability. Instead, the DNS domain included part of the prefilmer surface upstream of its edge to keep the influence of the interfacial stability in that region. Even so, the methodology has been validated from a practical standpoint compared against experimental data.

Some other limitations of the methodology must be emphasized, mainly caused by the need for a significant amount of computational resources. On the one hand, this implied a small computational domain, which yielded smaller ligaments than the ones reported in the experiments. However, this fact is indeed acknowledged in numerous literature studies with similar resolution. It also implied a small number of breakup events simulated, reducing variability in breakup events and lacking a deeper statistical analysis, so the results might be biased. On the other hand, adopting smaller cell sizes would have enhanced the depiction of the liquid-gas interface given the considerable number of droplets with the smallest reliable diameters (twice the cellsize), but still an

accurate turbulence representation was ensured through comparison with the Kolmogorov length scale. Furthermore, some mesh resolution issues affected the interface description when trying larger cell sizes for a mesh sensitivity study, as there were not enough cells to represent the liquid film. In order to assess the limitations concerning mesh cell size, a mesh sensitivity study has been proposed in the Basilisk code, similar to PARIS but with the inclusion of the Adaptive Mesh Refinement (AMR) feature. This study revealed no mesh independence in the droplet size and velocity distributions. Nevertheless, using a finer mesh without including the variable film thickness at the domain inlet did not allow retrieving the multimodal drop size distribution observed in the experiments, predicting that the vast majority of generated droplets are produced through the bag breakup mechanism. The fact that the simulation with variable film thickness in PARIS was indeed able to predict a multimodal size distribution correctly balancing bag breakup and ligament breakup means that the novel methodology proposed and developed in the thesis allows a better physical description of the problem than mesh refinement itself. This finding supports the effort carried out in implementing the technique.

The upcoming conclusions will refer to the parametric study, another key aspect of the thesis. The former proposed variation of the eDNS method has been chosen to explore how the formation of liquid structures is influenced by mean gas velocity and fluid properties. VOF-DNS simulations were conducted for four different operating conditions, involving two gas velocities and two liquids tested.

On the one hand, variations in the mean gas velocity have an impact on several key parameters within the atomization process. Higher gas velocities increase Re_g, all definitions of Weber numbers (We_l, We_h and We_δ) and momentum flux ratio M, but also decrease film thickness. These changes in the value of M are strong enough to induce differences in the breakup mechanism detected, in line with the findings in the literature. On the other hand, variations in the fluid properties (30% higher density, 4 times more dynamic viscosity and 70% more surface tension for H_2O-Propanediol than for Shellsol D70) result in lower Re_l and Weber numbers, but higher film thickness and Ohnesorge values. The momentum flux ratio is also reduced, but the breakup mechanism is not changed substantially. In summary, atomization ranges from finer in cases with high gas velocity and low density/viscosity to most inhibited in cases with low gas velocity and high density/viscosity.

The atomization process investigated had a consistent pattern in all cases, forming bags, rims and ligaments. Two different breakup mechanisms from

the literature have been identified among the four operating conditions tested: the *torn-sheet breakup* regime (cases with lower Re_g and M values) where liquid accumulation in the prefilmer edge is key and triggers film flapping, and the *membrane-sheet breakup* regime (cases with higher Re_g and M values). The analysis of ligaments properties among all cases highlighted that characteristic lengths correlated with the same trend infered from qualitative results (finer to more inhibited atomization state), characteristic frequencies followed the opposite trend, and characteristic velocities were nearly identical. However, the violent film flapping in the torn-sheet breakup regime cases slightly altered deformation velocities u_{def} and, therefore, breakup frequencies f_{bu} trends. In terms of droplet properties, Re_g played a crucial role in reducing the dispersion of droplet location and their wall-normal velocity distributions. Liquid characteristics also influenced wall-normal velocity distributions, specially for the torn-sheet breakup operating conditions with high asymmetry, but normalized spanwise velocity distributions showed limited variations.

Building upon the knowledge gained about primary atomization in airblast atomizers during this thesis, a *spray generator* has been developed. The algorithm accounts for a variable liquid mass flow rate (accounting for airblast atomization phenomenology), generating droplets in a loop until the target mass flow rate is reached. In the proposal, droplet position is computed from the DNS data (in a determined axial location), droplet size is conditioned by wall-normal location, and droplet velocities are influenced by droplet size. This model has been developed through the observation and analysis of the quantitative results obtained from the simulations conducted for the parametric study. Specifically, the appearance of the pdfs has been correlated with matematical functions, statistically adjusting the parameters that emerged in a reasonable manner. The spray generator has been evaluated by another partner of the ESTiMatE project for the reference operating condition, injecting lagrangian particles in a reacting LES of spray flames. Results showed an accurate replication of the droplet cloud from the DNS simulation.

Subsequently, the algorithm was extended to all operating conditions tested in the parametric study. To link the functional parameters (like droplet size and velocity) to the results obtained in those simulations, some statistical correlations were established between the mathematical expressions infered for the droplet pdfs and pertinent dimensionless factors acknowledged for their influence on primary atomization: main frequency f_{main} and droplet axial position are mainly influenced by the breakup regime (through Re_g and M) and the traditional Weber number We_l, but the wall-normal location is also linked to the atomizing edge height through We_h; droplet size is essentially governed by ρ_l and the boundary layer based Weber number We_δ; and droplet velocities

are mainly determined by h_l for the streamwise and wall-normal components, while ρ_l shapes the spanwise component.

Nevertheless, this process has some limitations. Merely four conditions were available for developing the proposed model, not being an extensive enough database to cover both atomization regimes identified in the parametric study. The applicability of the suggested model remains uncertain beyond its determined range, but the showcased procedure illustrated the possibility of generating a more extensive dataset.

All in all, creating a complete primary breakup model from particular high-fidelity simulations or, at least, identifying distinct submodels suitable for each atomization regime relevant to prefilming airblast atomizers would be feasible if enough computational resources were available.

6.2 Future works

Some aspects remain unaddressed or require further examination to warrant a deeper comprehension and modelling of primary atomization phenomena in airblast atomizers. To this end, the subsequent tasks may contribute significantly to this subject:

- One of the main drawbacks of limited computational resources was the inability to simulate a large amount of atomization events for every operating condition. This would provide valuable information for a deeper statistical analysis, improving the quality of the resulting pdfs and the validity of the model.

- The parametric study was performed with the constant film thickness approach as the variable film thickness approach involved some problems with mesh cell size. For some operating conditions, there appeared some non-physical dewetting in the film (not present in literature experiments) due to an insufficient number of cells to properly reproduce the film thickness itself and the gas-liquid interface. Refining the mesh in future simulations could allow variable film thickness DNS simulations to succeed regardless of the simulated operating condition, feeding the phenomenological model with improved results.

- Related to the previous point, refining the domain of the DNS simulations using PARIS Simulator would increase the number of cells exponentially. As a solution, the use of Adaptive Mesh Refinement (AMR)

could increase the number of cells in certain locations instead of the whole domain, improving the gas-liquid interface representation. PARIS Simulator does not have this feature, but another CFD code by the same authors Basilisk has. In Appendix A Basilisk has been succesfully used to perform a mesh study in the reference operating condition, so a complete parametric study with additional operating conditions could be performed to improve precision using a reasonable amount computational resources, as long as the variable film thickness approach is implemented in the code.

- It would be valuable to consider simulations involving the entire geometry of the atomizer, encompassing a more extensive region upstream of the prefilmer. Such simulations, although not necessarily at the DNS level, would provide an opportunity to assess the potential differences that may arise due to the absolute instability, and the influence of implementing two-way coupling on the simulations outcomes. This could offer deeper insight into the overall atomization process and contribute to a more comprehensive understanding of the system's behaviour.

- The intention of the ESTiMatE project was to integrate the phenomenological model with the ITD leader code PRECISE-UNS and the BSC code Alya, enabling the injection of droplets within Lagrangian simulations. This integration aims to faithfully replicate the characteristics of the primary atomization process during spray formation. By the time this document is being written, other partners of the project are working on this direction.

  A preliminary implementation has been carried out by BSC in Python for model verification, comparing the droplet cloud generated by the injection module in a lagrangian LES against the VOF-DNS obtained for the reference operating condition. It would be convenient to perform some additional tests for the rest of operating conditions.

- Another interesting investigation would be exploring the differences between using a predefined Rosin-Rammler droplet size distribution versus the proposed model. This would assess the impact of the computational representation on the spray in a reactive Lagrangian simulation of a spray flame.

- Employing the process described in the methodology for additional operating conditions could potentially generate a more extensive dataset

for devising a universal primary breakup model or, at least, for identifying distinct submodels suitable for each atomization regime relevant to prefilming airblast atomizers.

Appendices

Appendix A

Exploring mesh refinement through adaptive tools

In this Chapter, a comprehensive exploration of mesh refinement is performed for the reference operating condition by utilizing a different CFD code, Basilisk [108], which has adaptive meshing features.

Adaptive Mesh Refinement (AMR) is a numerical technique used in CFD and other computational sciences to dynamically adjust the grid resolution during the simulation. Berger and Colella pioneered an algorithm known as *local adaptive mesh refinement* [120] which has been broadly used in turbulence problems. The goal of this technique is to focus the mesh resolution efforts in regions of interest, allowing for a more efficient and accurate representation of the physical phenomena under investigation. It involves dividing the computational domain into a hierarchy of grids with varying resolutions. High-resolution grids are allocated in areas with complex flow features or steep gradients, while coarser grids are used in less critical regions. This adaptability allows for improved accuracy where it is needed most, optimizing computational efficiency.

Basilisk is a free software program designed for solving partial differential equations on adaptive Cartesian meshes. It has been developed by the same authors as its predecessor Gerris and PARIS Simulator. Basilisk programs are written in *Basilisk C*, a variant of the C language.

It is important to emphasize that, unlike the detailed studies presented in previous Chapters, the main objective of this Appendix is to verify the

new CFD code's capability to reproduce primary atomization features in two-phase flow DNS simulations using less computational resources than PARIS Simulator. If affirmative, a deeper mesh study would be feasible, and the injection model proposed in Chapter 5 could be easily extended.

A.1 Proposed methodology for the case of study

Many elements are shared between PARIS (explained in Section 2.2.3) and Basilisk codes. Therefore, this Section only provides details of the elements that differ between them.

A.1.1 Governing equations and related submodels

The incompressible, variable-density, Navier-Stokes equation with surface tension (Equation A.1) is solved using the finite volume approach with mass and momentum conservation, and including also the Continuous Surface Force (CSF) method to compute surface tension forces. The deformation tensor is $\mathbf{D} = [\nabla\mathbf{u} + (\nabla\mathbf{u})^T]/2$.

$$\rho\left[\frac{\partial\mathbf{u}}{\partial t} + \mathbf{u}\cdot\nabla\mathbf{u}\right] = -\nabla p + \nabla\cdot(2\mu\mathbf{D}) + \sigma\kappa\delta_S\mathbf{n} \tag{A.1}$$

$$\frac{\partial\alpha}{\partial t} + \mathbf{u}\cdot\nabla\alpha = 0 \tag{A.2}$$

The VOF method (remember Section 2.1.3) is also applied to capture the interface of the two-phase flow following Equation A.2, however the the Weymouth and Yue (WY) approach [121] is used to split-direction advection. For interface reconstruction, the normal vector $\mathbf{n}$ is computed from the volume fraction field using the Mixed-Youngs-Centered (MYC) approximation and basic geometric functions. On the other hand, the curvature κ is estimated through the Height Functions (HF) approach [85] as well.

A.1.2 Computational domain and mesh

In this study, the aim is to reproduce the reference simulation using the embed DNS approach showed in Figure 2.5 left, with variable air velocity, constant liquid velocity and film thickness (namely $h_l \neq f(t,z)$ case in Chapter 3 and OP#1 in Chapter 4). Reminding the geometry of the atomizing edge DNS domain (Figure 2.13) the new dimensions are compiled in Table A.1. Length and height have slightly lower values than the PARIS reference case but the

span is higher, as the domain needs to be squared and divisible by powers of 2. The prefilmer edge thickness h_p was shown in Table 1.1 and the film thickness is considered constant as well.

Table A.1: Main dimensions of the atomizing edge DNS computational domain.

Description	Parameter	Value [mm]
Domain length	L_x	5.12
Domain height	L_y	5.12
Domain span	L_z	5.12
Prefilming length	L_p	1.00

The spatial discretization of the 3D domain involves cubic finite volumes organized hierarchically as an octree [122]. Each finite volume is called a cell, and may act as the parent of up to eight children (four in 2D). A cell with no parents is called a *root cell*, which is the base of the tree, and a cell with no children is called a *leaf cell*. The refinement level of cells starts at zero for the root cell, and increases by one for every group of descendant children added. Each cell has a direct neighbour at the same level in each direction, these cells being connected by cell faces (edges in 2D). Figure A.1 provides an example of spatial discretization (left) and the corresponding tree representation (right) of a quadtree (two-dimensional equivalent of an octree) for illustrative purposes. In this grid, the flow pressure and velocity components are located at the cell centers, opposite to the staggered grid used in PARIS, as momentum conservation is simpler when dealing with mesh adaptation. For more details on the implementation the reader is referred to [123].

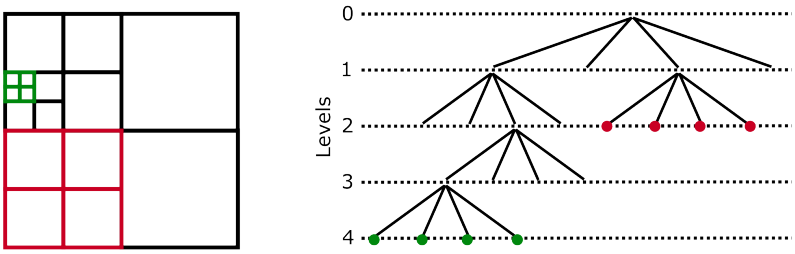

Figure A.1: Example of quadtree discretisation (left) and corresponding tree (right) adapted from [123].

The mesh is automatically refined where velocity or VOF gradients are greater than a threshold. Depending on the maximum and minimum refinement levels enabled, different ranges of cell sizes and number of cells are obtained. Two simulations have been performed to assess the influence of the minimum cell size on the results and to validate the mesh employed in the thesis, despite the slight differences between the codes. The main mesh properties of these simulations are gathered in Table A.2. For the reference case, the minimum refinement level imposed is 6 and the maximum is 9, resulting in a grid ranging from 0.26 to 134.22 million cells with sizes between 10 and 80 µm. This implies that, in this scenario, the finest resolution aligns with the resolution of the PARIS reference case. However, for the refined case, one more refinement level is enabled (10), allowing up to a maximum of 1073.74 million cells with a minimum size of 5 µm. The level of refinement near the inlet for both simulations is forced to 9 so the turbulent velocities can be properly mapped from the precursor LES simulation. The study thus intends to assess the sensitivity of the results to the minimum cell size.

Table A.2: Cases of study of the influence of mesh refinement.

Case	Description	Refinement levels	Number of cells [M]	Sizes [µm]
BSK ref	Reference	6 - 9	0.26 - 134.22	10 - 80
BSK fine	Refined	6 - 10	0.26 - 1073.74	5 - 80

A.1.3 Boundary conditions and discretization schemes

The α field is set to mantain a constant film thickness at the inlet (X- boundary) similar to $h_l \neq f(t, z)$ case in Chapter 3, as there is no implementation for a variable film thickness in Basilisk. In terms of velocities, the liquid velocity is also constant, but a Dirichlet boundary condition is implemented for the gaseous phase, incorporating time-varying velocity data obtained from the precursor LES simulation. This data is mapped onto the computational domain with linear interpolations between temporally sampled planes, ensuring a dynamic representation of the inlet conditions. On the other hand, a Neumann boundary condition is applied at the outlet (X+ boundary) and for the bottom and top bounds (Y- and Y+ boundaries) to maintain the numerical stability of the simulation, in order to avoid artificial reflections or disturbances. A symmetric condition is used spanwise (Z- and Z+ boundaries), ensuring that the normal component of the velocity is zero after projection through the balance of acceleration and pressure gradient. Solid immersed

boundaries (prefilmer solid wall) are treated forcing high inertia and turning velocity to 0 before advection. More details can be found in the Basilisk documentation [108].

For temporal discretization, a combination of a time-splitting projection-correction method (remember Equations 2.29 to 2.32) and a 2$^{\text{nd}}$ order staggered-in-time discretization is employed [124].

The projection step is presented in Equation A.3 with some simplification for readability, where A is the advection term, D is the diffusion term and F is the forces term.

$$\frac{(\mathbf{u}^* - \mathbf{u}^n)}{\Delta t} = -A^{n+\frac{1}{2}} + \frac{D^n + F^{n+\frac{1}{2}}}{\rho^{n+\frac{1}{2}}} \tag{A.3}$$

Then, the auxiliary velocity field $\mathbf{u}^*$ is corrected with the pressure gradient as shown in Equation A.4 so it turns out to be divergence-free. This results in the Poisson Equation A.5 expressed with no dependance of $\mathbf{u}^{n+1}$.

$$\frac{(\mathbf{u}^{n+1} - \mathbf{u}^*)}{\Delta t} = \frac{-\nabla p^{n+\frac{1}{2}}}{\rho^{n+\frac{1}{2}}} \tag{A.4}$$

$$\nabla \cdot \left(\frac{\nabla p^{n+\frac{1}{2}}}{\rho^{n+\frac{1}{2}}} \right) = \frac{\nabla \mathbf{u}^*}{\Delta t} \tag{A.5}$$

For the spatial discretization, an exact projection for face-centered velocities $\mathbf{u}^{*f}$ and an approximate projection for the cell-centered velocities $\mathbf{u}^{*c}$ are used. First, $\mathbf{u}^{*c}$ is computed from the projection step (Equation A.3). Then, the auxiliary face-centered velocity field $\mathbf{u}^{*f}$ is needed to obtain the divergence as shown in Equation A.6, where Δ is the length scale of the cell and $\mathbf{n}^f$ is the unit normal vector of the face. This term is computed averaging the cell-centered values, guaranteing consistency of the corresponding volume fluxes.

$$\nabla \cdot \mathbf{u}^* = \frac{1}{\Delta} \sum_f \mathbf{u}^{*f} \cdot \mathbf{n}^f \tag{A.6}$$

After solving this Equation, the face-centered pressure gradient is applied for the correction step (Equation A.4), obtaining the face-centered velocity field $\mathbf{u}^{n+1,f}$. Finally, said correction term is averaged over all the faces delimiting the control volume, so it can be used to obtain the cell-centered velocity field $\mathbf{u}^{n+1,c}$. The former field is divergence-free by definition, but the latter is approximately non-divergent.

A variable timestep is employed ensuring the maximum CFL number never surpasses 0.4, so each millisecond of simulated physical time required 45.3k core-hours for the *BSK ref* case and 106.3k core-hours for the *BSK fine* case.

A more detailed description of time and spatial discretization schemes is given in [85, 123].

A.1.4 Post-processing methods

This Section overviews the post-processing tools used for analyzing the atomization edge DNS data obtained through Basilisk CFD code.

Recalling the first step in Section 2.2.3.4, individual continuous liquid structures are identified using the same threshold value $\alpha = 0.5$. This allows to separate the intact core and ligaments from the droplet cloud. Due to the new mesh typology employed, the assessment of the core and ligaments is unfeasible without substantial modifications to the already developed post-processing scripts. Consequently, the focus is shifted exclusively to the analysis of the droplet cloud, where minor adjustments to the post-processing scripts permitted exploring and comparing the results.

A.1.4.1 Droplet cloud analysis

Assuming spherical droplets one more time, each individual droplet i is attributed a volumetric diameter based on Equation 2.35. The droplet i liquid volume ($V_{drop,i}$) is calculated as the sum of the liquid volume for every cell j belonging to the droplet, as in the first part of Equation 2.36 (reported again in Equation A.7 for illustrative purposes). However, AMR generates cells with different sizes, causing $V_{cell,j}$ to not be constant in this case and avoiding simplification.

$$V_{drop,i} = \sum_{j=1}^{Ncells} \alpha_j V_{cell,j} \tag{A.7}$$

Droplet velocities are computed as weighted averages of the velocity from each cell j composing the droplet. This was shown in the first part of Equation 2.37 (reported again in Equation A.8 for illustrative purposes), but now the weighting factor (total liquid volume) cannot be simplified with $V_{cell,j}$.

$$\mathbf{u_{drop,i}} = \frac{\sum_{j=1}^{Ncells} \alpha_j \cdot V_{cell,j} \cdot \mathbf{u_j}}{\sum_{j=1}^{Ncells} \alpha_j \cdot V_{cell,j}} \tag{A.8}$$

A.2 Results

In this Section, the results are presented by comparing the PARIS $h_l \neq f(t, z)$ case with both Basilisk simulations, as there is no implementation for variable film thickness and velocity in the latter code. By doing so, the effect of the minimum cell size is isolated while keeping the rest of the setup as similar as possible between them.

Concerning droplet sizes, Figure A.2 displays the PDFs of drop diameters for the three simulated cases. Please remind that droplets with a diameter less than twice the minimum cell size are not reliable and have been excluded from the analysis ($d_V \leq 20\,\mu m$ for PARIS and BSK ref, $d_V \leq 10\,\mu m$ for BSK fine). The comparison reveals a significant agreement between PARIS and BSK ref. Both cases seem to have a single breakup mode and maintain the same peak diameter, but there is a slight increase in larger droplets and a decrease in smaller droplets for the latter. However, the peak diameter for the BSK fine case has shifted to smaller values, as the finer mesh can capture smaller droplets. Therefore, the droplet size results are quite sensitive to the mesh resolution. Despite the extra level of refinement, the droplet diameter distribution obtained still appears to have a single mode, not resembling the multimodal distribution observed in the experiments and obtained for the $h_l = f(t, z)$ case in PARIS. This implies that, despite the lower cell size, most of the represented droplets are shaped from the bag breakup mechanism, without significant contribution from ligament breakup.

Regarding droplet velocities, Figure A.3 illustrates the PDFs obtained for each of the droplet velocity components. The velocity distributions exhibit a considerable similarity among PARIS and BSK ref scenarios, the differences being justified recalling the analysis from Chapter 3. On the other hand, distributions of the BSK fine simulation differ to a larger extent.

For the streamwise component, the distribution shape and dispersion about the average is almost identical between the first two cases, having the peak around a similar value. Nevertheless, some differences are present in the extremes, as the BSK ref case has a higher number of droplets with near null streamwise velocity, and there are no droplets that achieve a value greater than 70% u_g. Alternatively, the BSK fine case distribution is noticeably shifted to higher streamwise velocity values, closer to the mean gas velocity, with the peak around 50% u_g and deviation achieving 100%. This can be attributed to the presence of significantly smaller droplets, which exchange more momentum with the gas, thus accelerating.

In terms of wall-normal velocities, the PDFs are centered around 0 and

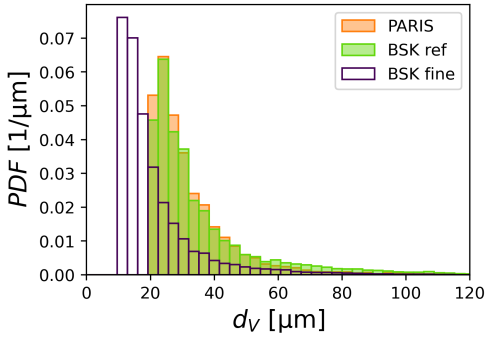

Figure A.2: Droplet size PDF for the three simulations.

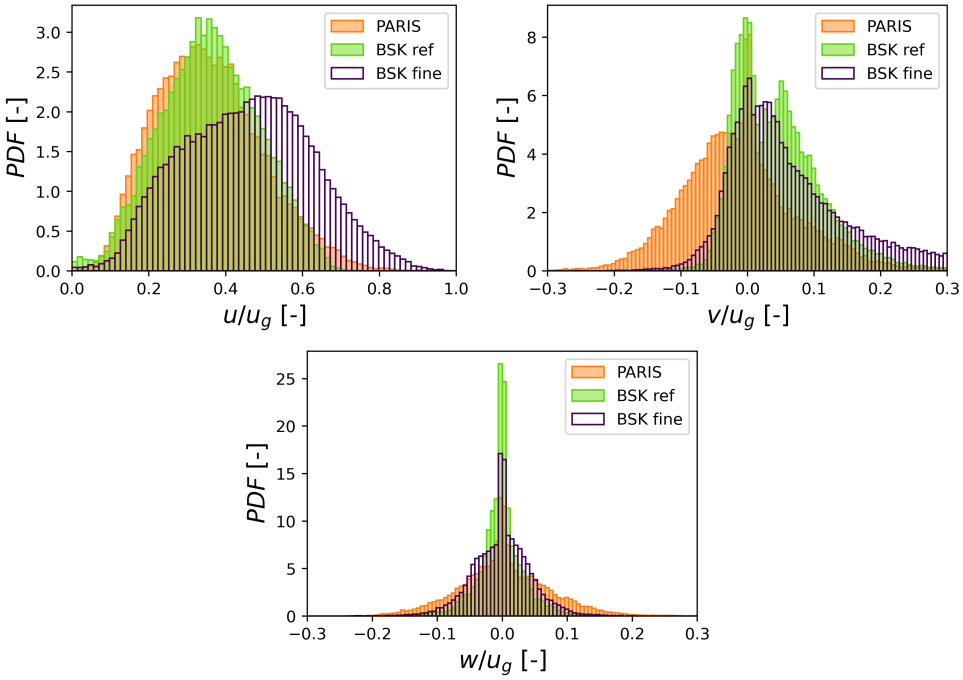

Figure A.3: PDFs for the droplet velocity components for the three simulated test cases: streamwise velocity (top left), wall-normal velocity (top right), spanwise velocity (bottom). All values are normalized with the gas bulk velocity.

have a high dispersion towards one side in all cases: negative values for PARIS and positive ones for both BSK simulations. This may be explained considering that the liquid film flaps violently, and the generated bags got punctured towards opposite sides of the prefilmer in the breakup events analyzed through each simulation (i.e. code), yielding a high amount of droplets below the prefilmer for the former case and above the prefilmer for the Basilisk cases. These locations strongly influence the wall-normal velocity component as droplets generated through this mechanism tend to travel further away from the prefilmer. Again, the BSK fine case predicts droplets with higher velocity values than the BSK ref case, as the extra amount of small droplets detected tends to reach velocities closer to that of the gas.

Finally, the spanwise component distributions are similarly centered around $w/u_g = 0$, but the Basilisk cases have a significantly higher peak and lower deviation from this value.

The following paragraphs will revisit the previous comparison with a significant change: filtering droplets with $d_V \leq 20\,\mu\text{m}$ for the BSK fine results. Filtering droplets with small sizes in this case might seem senseless, as one of the main advantages of simulating with a finer mesh is capturing smaller droplets. However, aligning the filtering criteria of all three simulations, both among them and with the resolution of the experiments (remember Chapter 2), may enable a fairer comparison and a better evaluation of the distributions characteristics. Specifically, it may provide information about whether the relative importance of the experimentally observed atomization mechanisms (bag breakup and ligament breakup) significantly changes with the cell size.

Observing the new drop diameters comparison in Figure A.4, the three distributions are almost identical now. This confirms the fact that the extra level of refinement in the last simulation has not managed to improve the description of the atomization mechanism, obtaining the same single mode shape contrary to the multimodal one observed in the experimental results and achieved in Chapter 3 by modifying the inlet boundary condition.

The velocity distributions of the BSK fine case are also modified after removing the smaller droplets, as illustrated in Figure A.5. In this occasion, the new streamwise velocities distribution is much more similar in shape and dispersion to the other cases, not exceeding the same 70% u_g limit obtained with a coarser mesh. It is also worth mentioning that the peak is slightly shifted towards a lower value. For the wall-normal component, both Basilisk distributions are much closer, again centered around 0 and with a high dispersion in one side. The finer mesh case still shows slightly more droplets with

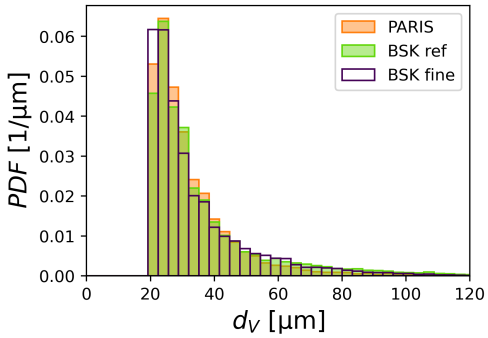

Figure A.4: Droplet size PDF for the three simulations, filtering droplets whose $d_V \leq 20\,\mu$m for BSK fine.

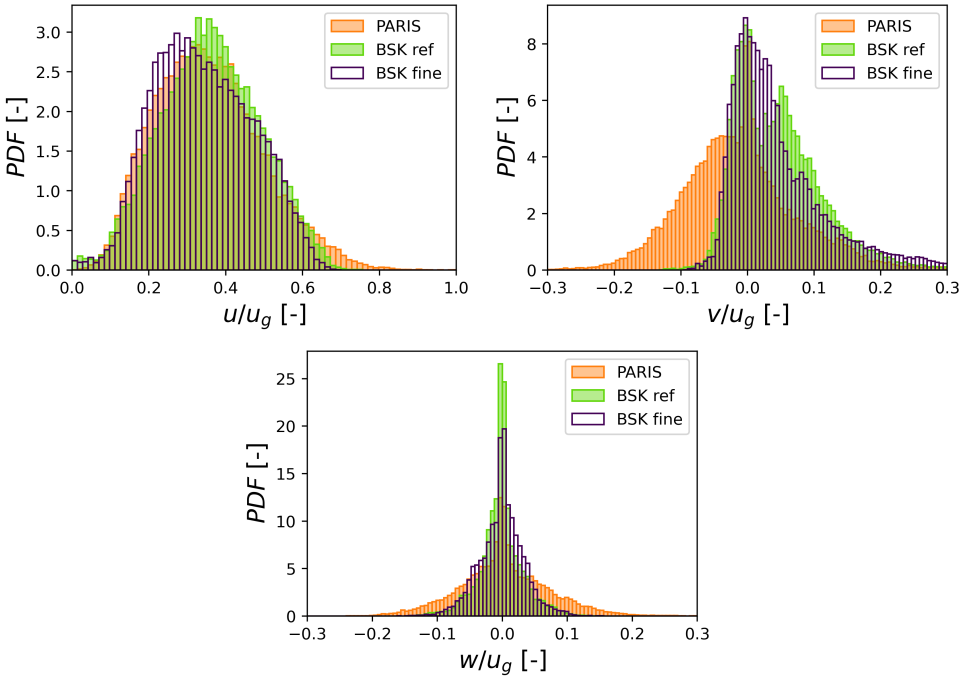

Figure A.5: PDFs for the droplet velocity components for the three simulated test cases, filtering droplets whose $d_V \leq 20\,\mu$m for BSK fine: streamwise velocity (top left), wall-normal velocity (top right), spanwise velocity (bottom). All values are normalized with the gas bulk velocity.

higher wall-normal velocities, but the secondary peak is obscured. Finally, the spanwise component distribution has not changed noticeably. Most droplets filtered had some velocity, so the population of the peak around null spanwise velocity is marginally greater. Both Basilisk distributions are almost identical.

A.3 Conclusions

A mesh study has been accomplished in this Appendix using the Basilisk CFD code to simulate the reference operating condition described in Chapter 3. The main advantage of this code over PARIS is its Adaptive Mesh Refinement tool, capable of dynamically adjusting the spatial resolution during the simulation based on the evolving flow features. Two different simulations have been performed in this analysis: the first one matching its maximum refinement level with the spatial discretization used throughout the thesis for the reference case (smallest cell size 10 µm), and the second one with an extra level of refinement available (until 5 µm).

A few minor changes have been applied to the postprocessing tools in order to get quantitative results (i.e. distributions of diameters and velocity components) of the droplets generated with Basilisk simulations. Despite the small differences between PARIS and Basilisk codes, fairly similar results have been obtained, confirming the latter can reproduce the atomization mechanism in two-phase flow DNS simulations with less computational resources. Once this methodology has been validated, a deeper mesh study would be feasible changing minimum and maximum levels of refinement in further simulations in order to improve accuracy and computational effort.

The finer case showed many differences in the distributions compared to the coarser one, indicating that the results do depend on the mesh and its ability to capture progressively smaller droplets, usually with higher velocities. However, when matching the droplet resolution of this simulation with the rest of simulations and with the resolution of the experiments available in the literature for validation (i.e. ignoring droplets with $d_V \leq 20\,\mu m$) differences practically dissappear. The fact that both fine and coarse cases are so similar supports the statement that the description reached with PARIS in Chapter 3 is reasonable for the reference operating condition.

Nevertheless, both Basilisk cases predict a single mode distribution for the droplet sizes. The distribution observed in the literature experiments is multimodal, in agreement with both bag breakup and ligament breakup processes being relevant atomization mechanisms. Hence, the extra level of mesh refinement was not able to improve the description of the breakup mechanism in the

reference operating conditions. The fact that the simulation with variable film thickness in PARIS ($h_l = f(t, z)$ case in Chapter 3) was indeed able to predict a multimodal distribution means that the novel methodology proposed and developed in the thesis to study breakup atomization allows a better physical description of the problem than mesh refinement itself. This finding supports the effort carried out in implementing this technique.

On the other hand, a combination of both refinement and improvement of the inlet boundary conditions (accounting for film history) could be tested with Basilisk for the operating conditions with lower film thicknesses, as those cases resulted in non-physical dewetting due to the PARIS limitations. In order to do this, it would be necessary to implement an inlet boundary condition with variable film thickness and velocities, as it has been done for PARIS. This way, in case of success, the injection model proposed in Chapter 5 could be easily improved and extended.

Bibliography

[1] Søvde, Ole Amund et al. "Aircraft emission mitigation by changing route altitude: A multi-model estimate of aircraft NOx emission impact on O3 photochemistry". In: *Atmospheric Environment* 95 (2014), pp. 468–479. DOI: 10.1016/j.atmosenv.2014.06.049 (cited on page 1).

[2] Valdés, Rosa Maria Arnaldo et al. "Flight Path 2050 and ACARE Goals for Maintaining and Extending Industrial Leadership in Aviation: A Map of the Aviation Technology Space." In: *Sustainability* 11 (7 2019), p. 2065. DOI: 10.3390/su11072065 (cited on page 1).

[3] Dareck, M, Edelstenn, C, and Ender, T. *Flightpath 2050 Europe's Vision for Aviation.* 2011 (cited on page 1).

[4] Liu, Yize et al. "Review of modern low emissions combustion technologies for aero gas turbine engines". In: *Progress in Aerospace Sciences* 94 (July 2017), pp. 12–45. DOI: 10.1016/j.paerosci.2017.08.001 (cited on page 2).

[5] *ESTiMatE - Emissions SooT ModEl 2020.* URL: https://estimate-project.eu/ (cited on page 2).

[6] Anand, M. S., Eggels, R., Staufer, M., Zedda, M., and Zhu, J. "An Advanced Unstructured-Grid Finite-Volume Design System for Gas Turbine Combustion Analysis". In: *ASME 2013 Gas Turbine India Conference.* American Society of Mechanical Engineers, 2013. ISBN: 978-0-7918-5616-1. DOI: 10.1115/GTINDIA2013-3537 (cited on page 2).

[7] Vázquez, Mariano et al. "Alya: Multiphysics engineering simulation toward exascale". In: *Journal of Computational Science* 14 (2016), pp. 15–27. DOI: 10.1016/j.jocs.2015.12.007 (cited on page 2).

[8] Lefebvre, Arthur H and McDonell, Vincent G. *Atomization and Sprays*. 2nd Ed. CRC Press, 2017. ISBN: 978-1-4987-3625-1 (cited on pages 3, 4).

[9] Peng, C.-A., Jurman, L.A., and McCready, M.J. "Formation of solitary waves on gas-sheared liquid layers". In: *International Journal of Multiphase Flow* 17 (6 1991), pp. 767–782. DOI: 10.1016/0301-9322(91)90055-8 (cited on page 4).

[10] Vlachos, N.A., Paras, S.V., and Karabelas, A.J. "Liquid-to-wall shear stress distribution in stratified/atomization flow". In: *International Journal of Multiphase Flow* 23 (5 1997), pp. 845–863. DOI: 10.1016/S0301-9322(97)00007-4 (cited on page 4).

[11] Shedd, Timothy A. and Newell, Ty A. "Characteristics of the Liquid Film and Pressure Drop in Horizontal, Annular, Two-phase Flow Through Round, Square and Triangular Tubes". In: *Journal of Fluids Engineering* 126 (5 2004), pp. 807–817. DOI: 10.1115/1.1792261 (cited on page 4).

[12] Fu, Qing-fei, Yang, Li-jun, and Qu, Yuan-yuan. "Measurement of annular liquid film thickness in an open-end swirl injector". In: *Aerospace Science and Technology* 15 (2 2011), pp. 117–124. DOI: 10.1016/j.ast.2010.06.006 (cited on page 4).

[13] Gepperth, Sebastian, Guildenbecher, Daniel, Koch, Rainer, and Bauer, Hans-Jörg. "Pre-filming primary atomization: Experiments and modeling". In: *ILASS-Europe 2010, 23rd Annual Conference on Liquid Atomization and Spray Systems*. 2010 (cited on pages 4, 8, 9, 14, 40, 41).

[14] Gepperth, Sebastian, Müller, Armin, Koch, Rainer, and Bauer, Hans-Jörg. "Ligament and Droplet Characteristics in Prefilming Airblast Atomization". In: *ICLASS 2012, 12th Triennial International Conference on Liquid Atomization and Spray Systems*. 2012 (cited on pages 4, 9, 10, 14, 47, 54, 61).

[15] Chaussonnet, Geoffroy. "Modeling of liquid film and breakup phenomena in Large-Eddy Simulations of aeroengines fueled by airblast atomizers". PhD thesis. Institut National Polytechnique de Toulouse - INPT, 2014. URL: https://theses.hal.science/tel-01006179 (cited on pages 5–7, 73).

[16] Rayana, Fares Ben, Cartellier, Alain H., and Hopfinger, Emil J. "Assisted Atomization of a Liquid Layer: Investigation of the parameters affecting the mean drop size prediction". In: *ICLASS 2006*. 2006. URL: https://hal.science/hal-00224338 (cited on page 5).

[17] Hong, Moongeun, Cartellier, Alain H., and Hopfinger, Emil J. "Atomisation and mixing in coaxial injection". In: *4th International Conference on Launcher Technology Space Launcher Liquid Propulsion*. 2002. URL: https://hal.science/hal-00202242 (cited on page 5).

[18] Marmottant, Philippe and Villermaux, Emmanuel. "Atomisation primaire dans les jets coaxiaux". In: *Combustion* 2 (1 2002), pp. 89–125 (cited on page 5).

[19] Raynal, Ludovic. "Instabilité et entrainement à l'interface d'une couche de mélange liquide-gaz". Thèse de doctorat dirigée par Hopfinger, Emil Mécanique Grenoble 1 1997. PhD thesis. 1997. URL: http://www.theses.fr/1997GRE10222%22 (cited on page 5).

[20] Varga, C. M., Lasheras, J. C., and Hopfinger, E. J. "Initial breakup of a small-diameter liquid jet by a high-speed gas stream". In: *Journal of Fluid Mechanics* 497 (497 2003), pp. 405–434. DOI: 10.1017/S0022112003006724 (cited on page 5).

[21] Gepperth, Sebastian, Koch, Rainer, and Bauer, Hans-Jörg. "Analysis and comparison of primary droplet characteristics in the near field of a prefilming airblast atomizer". In: *Proceedings of ASME Turbo Expo 2013: Turbine Technical Conference and Exposition*. 2013 (cited on page 6).

[22] Jurman, L. A., Bruno, K., and McCready, M. J. "Periodic and solitary waves on thin, horizontal, gas-sheared liquid films". In: *International Journal of Multiphase Flow* 15 (3 1989). DOI: 10.1016/0301-9322(89)90007-4 (cited on page 6).

[23] Mansour, Adel and Chigier, Norman. "Dynamic behavior of liquid sheets". In: *Physics of Fluids A* 3 (12 1991), pp. 2971–2980. DOI: 10.1063/1.857839 (cited on page 6).

[24] Stapper, B.E. and Samuelsen, G.S. "An experimental study of the breakup of a two-dimensional liquid sheet in the presence of co-flow air shear". In: *28th Aerospace Sciences Meeting*. American Institute of Aeronautics and Astronautics, 1990. DOI: 10.2514/6.1990-461. URL: http://arc.aiaa.org/doi/10.2514/6.1990-461 (cited on page 6).

[25] Lozano, Antonio, Call, Charles J., Dopazo, César, and García-Olivares, Antonio. "Experimental and numerical study of the atomization of a planar liquid sheet". In: *Atomization and Sprays* 6 (1 1996), pp. 77–94. DOI: 10.1615/AtomizSpr.v6.i1.40 (cited on page 6).

[26] Fernandez, V. G., Berthoumie, P., and Lavergne, G. “Liquid sheet disintegration at high pressure: An experimental approach”. In: *Comptes Rendus - Mecanique* 337 (6-7 2009), pp. 481–491. DOI: 10.1016/j.crme.2009.06.026 (cited on pages 6, 7, 63).

[27] Jasuja, Arvind K. “Behaviour of aero-engine airblast sprays in practical environments”. In: *ICLASS 2016, 10th International Conference on Liquid Atomization and Spray Systems*. 2006 (cited on pages 7, 13).

[28] Matsuura, Kazuaki, Suzuki, Kazuhiro, and Kurosawa, Yoji. “Effects of Ambient Pressure on Spray Characteristics of a High-Shear-Type Aero-Engine Airblast Fuel Injector”. In: *ILASS 2008*. 2008 (cited on pages 7, 13).

[29] Gepperth, S, Bärow, E, Koch, R, and Bauer, H J. “Primary atomization of prefilming airblast nozzles: Experimental studies using advanced image processing techniques”. In: *26th Annual Conference on Liquid Atomization and Spray Systems (ILASS Europe)*. 2014 (cited on pages 7, 10, 13).

[30] Holz, Simon, Braun, Samuel, Chaussonnet, Geoffroy, Koch, Rainer, and Bauer, Hans Jörg. “Close nozzle spray characteristics of a prefilming airblast atomizer”. In: *Energies* 12 (14 2019), pp. 1–22. DOI: 10.3390/en12142835 (cited on page 8).

[31] Berthoumieu, Pierre and Lavergne, Gérard. “Video techniques applied to the characterization of liquid sheet breakup”. In: *Journal of Visualization* 4 (3 2001), pp. 267–275. DOI: 10.1007/BF03182587 (cited on pages 8, 13).

[32] Holz, Simon, Chaussonnet, Geoffory, Gepperth, Sebastian, Koch, Rainer, and Bauer, Hans-Joerg. “Comparison of the Primary Atomization Model PAMELA with Drop Size Distributions of an Industrial Prefilming Airblast Nozzle”. In: *ILASS - Europe 2016, 27th Annual Conference on Liquid Atomization and Spray Systems*. 2016. URL: https://www.researchgate.net/publication/307931957 (cited on pages 8, 13).

[33] Inamura, T. et al. “Spray characteristics of prefilming type of airblast atomizer”. In: *ICLASS 2012 - 12th International Conference on Liquid Atomization and Spray Systems*. 2012 (cited on pages 8, 14).

[34] Inamura, T., Katagata, N., Nishikawa, H., Okabe, T., and Fumoto, K. "Effects of prefilmer edge thickness on spray characteristics in prefilming airblast atomization". In: *International Journal of Multiphase Flow* 121 (2019), p. 103117. DOI: 10.1016/j.ijmultiphaseflow.2019.103117 (cited on pages 8, 14, 63).

[35] Matas, Jean Philippe. "Inviscid versus viscous instability mechanism of an air-water mixing layer". In: *Journal of Fluid Mechanics* 768 (2015). DOI: 10.1017/jfm.2015.106 (cited on pages 8, 14).

[36] Chaussonnet, Geoffroy, Müller, A, Holz, Simon, Koch, Rainer, and Bauer, H. J. "Time-Response of Recent Prefilming Airblast Atomization Models in an Oscillating Air Flow Field". In: *Journal of Engineering for Gas Turbines and Power* 139 (12 2017). DOI: 10.1115/1.4037325 (cited on pages 9, 14).

[37] Chaussonnet, Geoffroy et al. "Investigation of the liquid accumulation characteristics in planar prefilming airblast atomization". In: *ICLASS 2018 - 14th International Conference on Liquid Atomization and Spray Systems*. 2018 (cited on pages 9, 14).

[38] Chaussonnet, G., Gepperth, S., Holz, S., Koch, R., and Bauer, H. J. "Influence of the ambient pressure on the liquid accumulation and on the primary spray in prefilming airblast atomization". In: *International Journal of Multiphase Flow* 125 (2020), p. 103229. DOI: 10.1016/j.ijmultiphaseflow.2020.103229 (cited on pages 10, 14, 47, 54).

[39] Payri, Raul, Gimeno, Jaime, Martí-Aldaraví, Pedro, and Carvallo, César. "Parametrical study of the dispersion of an alternative fire suppression agent through a real-size extinguisher system nozzle under realistic aircraft cargo cabin conditions". In: *Process Safety and Environmental Protection* 141 (2020). DOI: 10.1016/j.psep.2020.04.022 (cited on page 10).

[40] Chaussonnet, G., Vermorel, O., Riber, E., and Cuenot, B. "A new phenomenological model to predict drop size distribution in Large-Eddy Simulations of airblast atomizers". In: *International Journal of Multiphase Flow* 80 (2016), pp. 29–42. DOI: 10.1016/j.ijmultiphaseflow.2015.10.014 (cited on pages 10, 14, 15, 29, 54).

[41] Palanti, L. et al. "An attempt to predict spray characteristics at early stage of the atomization process by using surface density and curvature distribution". In: *International Journal of Multiphase Flow* 147 (2021), p. 103879. DOI: 10.1016/j.ijmultiphaseflow.2021.103879 (cited on pages 10, 16).

[42] Weller, H. G., Tabor, G., Jasak, H., and Fureby, C. "A tensorial approach to computational continuum mechanics using object-oriented techniques". In: *Computers in Physics* 12 (6 1998), p. 620. DOI: 10.1063/1.168744 (cited on pages 10, 31).

[43] Mukundan, Anirudh Asuri, Ménard, Thibaut, Berlemont, A, Motta, Jorge César Brändle de, and Eggels, Ruud. "Validation and Analysis of 3D DNS of planar pre-filming airblast atomization simulations". In: *ILASS Americas, 30th Annual Conference on Liquid Atomization and Spray Systems*. 2019 (cited on pages 11, 16, 24, 43).

[44] Braun, Samuel et al. "Numerical prediction of air-assisted primary atomization using Smoothed Particle Hydrodynamics". In: *International Journal of Multiphase Flow* 114 (2019), pp. 303–315. DOI: 10.1016/j.ijmultiphaseflow.2019.03.008 (cited on pages 11, 12, 16, 45).

[45] Sauer, Benjamin, Sadiki, Amsini, and Janicka, Johannes. "Numerical Analysis of the Primary Breakup Applying the Embedded DNS Approach to a Generic Prefilming Airblast Atomizer". In: *The Journal of Computational Multiphase Flows* 6 (3 2014), pp. 179–192. DOI: 10.1260/1757-482X.6.3.179 (cited on pages 11, 15, 27, 43, 108).

[46] Sauer, B., Sadiki, A., and Janicka, J. "Embedded DNS concept for simulating the primary breakup of an airblast atomizer". In: *Atomization and Sprays* 26 (3 2016), pp. 187–217. DOI: 10.1615/AtomizSpr.2014011019 (cited on pages 11, 15, 31, 44, 54).

[47] Warncke, K. et al. "Experimental and numerical investigation of the primary breakup of an airblasted liquid sheet". In: *International Journal of Multiphase Flow* 91 (2017), pp. 208–224. DOI: 10.1016/j.ijmultiphaseflow.2016.12.010 (cited on pages 11, 16, 43, 44, 47, 49–52, 54, 56, 60–65, 76).

[48] Warncke, K, Sadiki, A, and Janicka, J. "New insights in the role of turbulence for simulating primary breakup of prefilming airblast atomization". In: *ILASS - Europe 2019, 29th European Conference on Liquid Atomization and Spray Systems*. 2019 (cited on pages 11, 16).

[49] Jiang, Delin and Ling, Yue. "Destabilization of a planar liquid stream by a co-flowing turbulent gas stream". In: *International Journal of Multiphase Flow* 122 (2020). DOI: 10.1016/j.ijmultiphaseflow.2019.103121 (cited on pages 11, 16).

[50] Jiang, D. and Ling, Y. "Impact of inlet gas turbulence on the formation, development and breakup of interfacial waves in a two-phase mixing layer". In: *Journal of Fluid Mechanics* 921 (2021). DOI: 10.1017/jfm.2021.481 (cited on pages 11, 16).

[51] Torregrosa, Antonio J., Payri, Raúl, Salvador, F. Javier, and Crialesi-Esposito, Marco. "Study of turbulence in atomizing liquid jets". In: *International Journal of Multiphase Flow* 129 (2020). DOI: 10.1016/j.ijmultiphaseflow.2020.103328 (cited on pages 11, 24).

[52] Payri, Raúl, Gimeno, Jaime, Martí-Aldaraví, Pedro, and Martínez, María. "Transient nozzle flow analysis and near field characterization of gasoline direct fuel injector using Large Eddy Simulation". In: *International Journal of Multiphase Flow* 148 (2022). DOI: 10.1016/j.ijmultiphaseflow.2021.103920 (cited on pages 11, 24).

[53] Carmona, J. et al. "A comparative study of direct numerical simulation and experimental results on a prefilming airblast atomization configuration". In: *Atomization and Sprays* 31 (8 2021), pp. 9–32. DOI: 10.1615/ATOMIZSPR.2021037399 (cited on pages 11, 16).

[54] Desjardins, Olivier, Blanquart, Guillaume, Balarac, Guillaume, and Pitsch, Heinz. "High order conservative finite difference scheme for variable density low Mach number turbulent flows". In: *Journal of Computational Physics* 227 (15 2008). DOI: 10.1016/j.jcp.2008.03.027 (cited on page 11).

[55] Zandian, A., Sirignano, W. A., and Hussain, F. "Planar liquid jet: Early deformation and atomization cascades". In: *Physics of Fluids* 29 (6 2017), p. 062109. DOI: 10.1063/1.4986790 (cited on pages 11, 15, 24).

[56] Zandian, A., Sirignano, W. A., and Hussain, F. "Understanding liquid-jet atomization cascades via vortex dynamics". In: *Journal of Fluid Mechanics* 843 (2018), pp. 293–354. DOI: 10.1017/jfm.2018.113 (cited on pages 11, 15).

[57] Zandian, Arash, Sirignano, William A., and Hussain, Fazle. "Length-scale cascade and spread rate of atomizing planar liquid jets". In: *International Journal of Multiphase Flow* 113 (2019), pp. 117–141. DOI: 10.1016/j.ijmultiphaseflow.2019.01.004 (cited on pages 11, 15).

[58] Agbaglah, G., Chiodi, R., and Desjardins, Olivier. "Numerical simulation of the initial destabilization of an air-blasted liquid layer". In: *Journal of Fluid Mechanics* 812 (2017), pp. 1024–1038. DOI: 10.1017/jfm.2016.835 (cited on pages 11, 15, 24).

[59] Mukundan, Anirudh Asuri, Ménard, Thibaut, Motta, Jorge César Brändle de, and Berlemont, Alain. "Detailed numerical simulations of primary atomization of airblasted liquid sheet". In: *International Journal of Multiphase Flow* 147 (2022). DOI: 10.1016/j.ijmultiphaseflow.2021.103848 (cited on pages 11, 16, 24, 43, 60, 62).

[60] Mukundan, Anirudh Asuri, Ménard, Thibaut, Berlemont, Alain, and Motta, Jorge César Brändle de. "A comparative study of DNS of airblast atomization using CLSMOF and CLSVOF methods". In: *ILASS - Europe 2019, 29th European Conference on Liquid Atomization and Spray Systems*. 2019 (cited on pages 11, 16, 24, 43).

[61] Koch, Rainer et al. "Prediction of primary atomization using Smoothed Particle Hydrodynamics". In: *European Journal of Mechanics - B/Fluids* 61 (2017), pp. 271–278. DOI: 10.1016/j.euromechflu.2016.10.007 (cited on pages 11, 15).

[62] Holz, Simon et al. "New Insights in the Primary Breakup Process of Prefilming Airblast Atomizers by SPH Predictions". In: *ICLASS 2018, 14th Triennial International Conference on Liquid Atomization and Spray Systems*. 2018 (cited on pages 11, 15, 40, 63).

[63] Richardson, Lewis F. "Weather prediction by numerical process, second edition". In: *Weather Prediction by Numerical Process, Second Edition* (1922), pp. 1–236. DOI: 10.1017/CBO9780511618291 (cited on page 19).

[64] Kolmogorov, A. "On the log-normal distribution of particles sizes during breakup process". In: *Dokl. Akad. Nauk.* XXXI (4 1941), pp. 99–101 (cited on page 19).

[65] Grete, Philipp, O'Shea, Brian W., and Beckwith, Kris. "As a Matter of Dynamical Range – Scale Dependent Energy Dynamics in MHD Turbulence". In: *The Astrophysical Journal Letters* 942 (2 2023), p. L34. DOI: 10.3847/2041-8213/acaea7 (cited on page 20).

[66] Mirjalili, S., Jain, Suhas S., and Dodd, M. S. "Interface-capturing methods for two-phase flows: An overview and recent developments". In: *Center for Turbulence Research Annual Research Briefs*. 2017, pp. 117–135 (cited on page 22).

[67] Luo, Kun, Shao, Changxiao, Chai, Min, and Fan, Jianren. "Level set method for atomization and evaporation simulations". In: *Progress in Energy and Combustion Science* 73 (2019), pp. 65–94. DOI: 10.1016/j.pecs.2019.03.001 (cited on page 23).

[68] Glimm, J, Isaacson, E, Marchesin, D, and McBryan, O. "Front tracking for hyperbolic systems". In: *Advances in Applied Mathematics* 2 (1 1981), pp. 91–119. DOI: 10.1016/0196-8858(81)90040-3 (cited on page 22).

[69] Unverdi, S O and Tryggvason, G. "A front-tracking method for viscous, incompressible, multi-fluid flows". In: *J. Comput. Phys.* 100 (1992), pp. 25–37 (cited on pages 22, 23).

[70] Tryggvason, G. et al. "A Front-Tracking Method for the Computations of Multiphase Flow". In: *Journal of Computational Physics* 169 (2 2001), pp. 708–759. DOI: 10.1006/jcph.2001.6726 (cited on page 22).

[71] Hirt, C.W W and Nichols, B.D D. "Volume of fluid (VOF) method for the dynamics of free boundaries". In: *Journal of Computational Physics* 39 (1 1981), pp. 201–225. DOI: 10.1016/0021-9991(81)90145-5 (cited on pages 24, 25).

[72] Noh, W. F. and Woodward, Paul. "SLIC (Simple Line Interface Calculation)". In: 1976. DOI: 10.1007/3-540-08004-x_336 (cited on page 25).

[73] DeBar, Roger B. "Fundamentals of the KRAKEN code". In: *Technical Report* (March 1974) (cited on page 25).

[74] Youngs, David L. "Time-dependent multi-material flow with large fluid distortion". In: *Numerical Methods for Fluid Dynamics* (1982) (cited on page 25).

[75] Youngs, David L. "An interface tracking method for a 3D Eulerian hydrodynamics code". In: *Atomic Weapons Research Establishment (AWRE) Technical Report 44/92/35* (1984), p. 35 (cited on page 25).

[76] Li, J. "Calcul d'Interface Affine par Morceaux (Piecewise linear interface calculation)". In: *C. R. Acad. Sci. Paris, II* 320 (1995), pp. 391–396 (cited on pages 25, 42).

[77] Tryggvason, Grétar, Scardovelli, Ruben, and Zaleski, Stéphane. *Direct Numerical Simulations of Gas–Liquid Multiphase Flows*. 1st. Cambridge University Press, 2011. ISBN: 9780521787505 (cited on pages 25, 26, 43, 46).

[78] Pilliod, James Edward and Puckett, Elbridge Gerry. "Second-order accurate volume-of-fluid algorithms for tracking material interfaces". In: *Journal of Computational Physics* 199 (2 2004), pp. 465–502. DOI: 10.1016/j.jcp.2003.12.023 (cited on page 25).

[79] Scardovelli, R and Zaleski, S. “Interface Reconstruction with Least-Square Fit and Split Lagrangian-Eulerian Advection”. In: *Int J. Numer. Meth. Fluids* 41 (2003), pp. 251–274 (cited on page 25).

[80] Brackbill, J.U U, Kothe, D.B B, and Zemach, C. “A continuum method for modeling surface tension”. In: *Journal of Computational Physics* 100 (2 1992), pp. 335–354. DOI: 10.1016/0021-9991(92)90240-Y (cited on page 26).

[81] Renardy, Yuriko and Renardy, Michael. “PROST a parabolic reconstruction of surface tension for the volume-of-fluid method”. In: *Journal of computational physics* 183 (2 2002), pp. 400–421 (cited on page 26).

[82] Torrey, Martin D, Cloutman, Lawrence D, Mjolsness, Raymond C, and Hirt, C W. “NASA-VOF2D: a computer program for incompressible flows with free surfaces”. In: *NASA STI/Recon Technical Report N* 86 (1985), p. 30116 (cited on page 27).

[83] Sussman, Mark. “A second order coupled level set and volume-of-fluid method for computing growth and collapse of vapor bubbles”. In: *Journal of Computational Physics* 187 (1 2003), pp. 110–136 (cited on page 27).

[84] Cummins, Sharen J., Francois, Marianne M., and Kothe, Douglas B. “Estimating curvature from volume fractions”. In: *Computers & Structures* 83 (6-7 2005), pp. 425–434. DOI: 10.1016/j.compstruc.2004.08.017 (cited on page 27).

[85] Popinet, Stéphane. “An accurate adaptive solver for surface-tension-driven interfacial flows”. In: *Journal of Computational Physics* 228 (16 2009). DOI: 10.1016/j.jcp.2009.04.042 (cited on pages 27, 43, 120, 124).

[86] White, Frank M. *Viscous fluid flow*. 3rd. McGraw-Hill, 2006. ISBN: 007-124493-X (cited on page 30).

[87] Fuster, D. et al. “Instability regimes in the primary breakup region of planar coflowing sheets”. In: *Journal of Fluid Mechanics* 736 (2013), pp. 150–176. DOI: 10.1017/jfm.2013.536 (cited on page 30).

[88] Issa, R.I. “Solution of the implicitly discretised fluid flow equations by operator-splitting”. In: *Journal of Computational Physics* 62 (1 1986), pp. 40–65. DOI: 10.1016/0021-9991(86)90099-9 (cited on page 31).

[89] Nicoud, F. and Ducros, F. “Subgrid-Scale Stress Modelling Based on the Square of the Velocity Gradient Tensor”. In: *Flow, Turbulence and Combustion* 62 (3 1999), pp. 183–200. DOI: 10.1023/A:1009995426001 (cited on page 31).

[90] Moser, Robert D, Kim, John, and Mansour, Nagi N. "Direct numerical simulation of turbulent channel flow up to Reτ=590". In: *Physics of Fluids* 11 (4 1999), pp. 943–945. DOI: 10.1063/1.869966 (cited on page 31).

[91] *OpenFOAM - blockMesh*. URL: https://www.openfoam.com/documentation/guides/latest/man/blockMesh.html (cited on page 31).

[92] *OpenFOAM - boxTurb*. URL: https://www.openfoam.com/documentation/guides/latest/man/boxTurb.html (cited on page 32).

[93] Lee, Sang Bong. "A study on temporal accuracy of OpenFOAM". In: *International Journal of Naval Architecture and Ocean Engineering* 9 (4 2017), pp. 429–438. DOI: 10.1016/j.ijnaoe.2016.11.007 (cited on page 32).

[94] Greenshields, Christopher and Weller, Henry. *Notes on Computational Fluid Dynamics: General Principles*. CFD Direct Ltd, 2022. ISBN: 978-1-3999-2078-0 (cited on page 33).

[95] Iwamoto, Kaoru, Suzuki, Yuji, and Kasagi, Nobuhide. "Reynolds number effect on wall turbulence: Toward effective feedback control". In: *International Journal of Heat and Fluid Flow* 23 (5 2002). DOI: 10.1016/S0142-727X(02)00164-9 (cited on page 34).

[96] Wardle, Kent E. and Weller, Henry G. "Hybrid multiphase CFD solver for coupled dispersed/segregated flows in liquid-liquid extraction". In: *International Journal of Chemical Engineering* (2013). DOI: 10.1155/2013/128936 (cited on pages 35, 38).

[97] Aniszewski, W., Bogusławski, A., Marek, M., and Tyliszczak, A. "A new approach to sub-grid surface tension for LES of two-phase flows". In: *Journal of Computational Physics* 231 (21 2012), pp. 7368–7397. DOI: 10.1016/j.jcp.2012.07.016 (cited on page 36).

[98] Herrmann, Marcus. "A Sub-Grid Surface Dynamics Model for Sub-Filter Surface Tension Induced Phase Interface Dynamics". In: *8th International Conference on Multiphase Flow (ICMF 2013)* 1 (480 2013), pp. 1–7 (cited on page 36).

[99] Jofre, Lluís, Dodd, Michael S., Grau, Joan, and Torres, Ricardo. "Near-interface flow modeling in large-eddy simulation of two-phase turbulence". In: *International Journal of Multiphase Flow* 132 (2020), p. 103406. DOI: 10.1016/j.ijmultiphaseflow.2020.103406 (cited on page 36).

[100] Zalesak, Steven T. “Fully multidimensional flux-corrected transport algorithms for fluids”. In: *Journal of Computational Physics* 31 (3 1979), pp. 335–362. DOI: 10.1016/0021-9991(79)90051-2 (cited on page 38).

[101] Crank, J. and Nicolson, P. “A practical method for numerical evaluation of solutions of partial differential equations of the heat-conduction type”. In: *Mathematical Proceedings of the Cambridge Philosophical Society* 43 (1 1947), pp. 50–67. DOI: 10.1017/S0305004100023197 (cited on page 38).

[102] Leer, Bram van. “Towards the ultimate conservative difference scheme. II. Monotonicity and conservation combined in a second-order scheme”. In: *Journal of Computational Physics* 14 (4 1974), pp. 361–370. DOI: 10.1016/0021-9991(74)90019-9 (cited on page 38).

[103] *Numerical study on the temporal discretization schemes in two-phase wave simulation*. Vol. Volume 2: CFD and FSI. 38th International Conference on Offshore Mechanics and Arctic Engineering - OMAE. 2019, V002T08A016. ISBN: 9780791858776. DOI: 10.1115/OMAE2019-96278 (cited on page 38).

[104] Deshpande, Suraj S., Anumolu, Lakshman, and Trujillo, Mario F. “Evaluating the performance of the two-phase flow solver interFoam”. In: *Computational Science and Discovery* 5 (2012), p. 014016. DOI: 10.1088/1749-4699/5/1/014016 (cited on page 38).

[105] Aniszewski, W. et al. “PArallel, Robust, Interface Simulator (PARIS)”. In: *Computer Physics Communications* 263 (2021), p. 107849. DOI: 10.1016/j.cpc.2021.107849 (cited on pages 42, 43, 46).

[106] Scardovelli, Ruben and Zaleski, Stephane. “Interface reconstruction with least-square fit and split Eulerian-Lagrangian advection”. In: *International Journal for Numerical Methods in Fluids* 41 (3 2003), pp. 251–274. DOI: 10.1002/fld.431 (cited on page 42).

[107] Pope, Stephen B. *Turbulent Flows*. Cambridge University Press, 2000. ISBN: 9780521591256 (cited on page 44).

[108] Popinet, S. *Basilisk flow solver*. 2023. URL: http://basilisk.fr/ (cited on pages 44, 119, 123).

[109] Kajishima, Takeo and Taira, Kunihiko. *Computational Fluid Dynamics*. 1st. Springer International Publishing, 2017. ISBN: 978-3-319-45302-6 (cited on page 45).

[110] Lacis, Ugis et al. “Nanoscale sheared droplet: volume-of-fluid, phase-field and no-slip molecular dynamics”. In: *Journal of Fluid Mechanics* 940 (2022), pp. 1–45. DOI: 10.1017/jfm.2022.219 (cited on page 45).

[111] Legendre, D. and Maglio, M. "Comparison between numerical models for the simulation of moving contact lines". In: *Computers and Fluids* 113 (2015), pp. 2–13. DOI: 10.1016/j.compfluid.2014.09.018 (cited on page 45).

[112] Leonard, B.P. Brian P. "A stable and accurate convective modelling procedure based on quadratic upstream interpolation". In: *Computer methods in applied mechanics and engineering* 19 (1 1979), pp. 59–98. DOI: 10.1016/0045-7825(79)90034-3 (cited on page 46).

[113] Chorin, Alexandre Joel. "Numerical solution of the Navier-Stokes equations". In: *Mathematics of Computation* 22 (1968), pp. 745–762. DOI: 10.2307/2004575 (cited on page 46).

[114] Crialesi-Esposito, Marco, Gonzalez-Montero, L. A., and Salvador, F. J. "Effects of isotropic and anisotropic turbulent structures over spray atomization in the near field". In: *International Journal of Multiphase Flow* 150 (December 2020 2022). DOI: 10.1016/j.ijmultiphaseflow.2021.103891 (cited on pages 47, 51).

[115] Schroeder, Will, Martin, Ken, and Lorensen, Bill. *The Visualization Toolkit (VTK)*. 2018. URL: https://vtk.org/ (cited on page 47).

[116] Bradski, G. "The OpenCV Library (2000)". In: *Dr. Dobb's Journal of Software Tools* (2000) (cited on page 49).

[117] Sethian, J. A. "A fast marching level set method for monotonically advancing fronts." In: *Proceedings of the National Academy of Sciences* 93 (4 1996), pp. 1591–1595. DOI: 10.1073/pnas.93.4.1591 (cited on page 49).

[118] Payri, R., Salvador, F. J., Carreres, M., and Moreno-Montagud, C. "A computational methodology to account for the liquid film thickness evolution in Direct Numerical Simulation of prefilming airblast atomization". In: *International Journal of Multiphase Flow* 161 (2023). DOI: 10.1016/j.ijmultiphaseflow.2023.104403 (cited on page 75).

[119] Guillamón, Carlos, Carreres, Marcos, Moreno-Montagud, Carlos, Eggels, Ruud, and Mira, Daniel. "Assessment and validation of a phenomenological atomization model for airblast spray injection". In: *ILASS Europe 2023, 31st European Conference on Liquid Atomization & Spray Systems*. 2023, pp. 4–7 (cited on page 105).

[120] Berger, M. J. and Colella, P. "Local adaptive mesh refinement for shock hydrodynamics". In: *Journal of Computational Physics* 82 (1 1989). DOI: 10.1016/0021-9991(89)90035-1 (cited on page 119).

[121] Weymouth, G. D. and Yue, Dick K.P. "Conservative Volume-of-Fluid method for free-surface simulations on Cartesian-grids". In: *Journal of Computational Physics* 229 (8 2010). DOI: 10.1016/j.jcp.2009.12.018 (cited on page 120).

[122] Samet, Hanan. *Applications of spatial data structures: Computer graphics, image processing, and GIS*. USA: Addison-Wesley Longman Publishing Co., Inc., 1990. ISBN: 020150300X (cited on page 121).

[123] Popinet, Stéphane. "Gerris: A tree-based adaptive solver for the incompressible Euler equations in complex geometries". In: *Journal of Computational Physics* 190 (2 2003). DOI: 10.1016/S0021-9991(03)00298-5 (cited on pages 121, 124).

[124] Chorin, Alexandre Joel. "On the convergence of discrete approximations to the Navier-Stokes equations". In: *Mathematics of Computation* 23 (106 1969). DOI: 10.1090/s0025-5718-1969-0242393-5 (cited on page 123).